The Dissertation Committee for Zhitao Li Certifies that this is the approved version of the following dissertation:

Modeling and Simulation of Polymer Flooding Including the Effects of Fracturing

Committee:

Mojdeh Delshad, Supervisor

Mary F. Wheeler

Gary A. Pope

Kamy Sepehrnoori

Chun Huh

Modeling and Simulation of Polymer Flooding Including the Effects of Fracturing

by

Zhitao Li, B.S.; M.S.E.

Dissertation

Presented to the Faculty of the Graduate School of

The University of Texas at Austin

in Partial Fulfillment

of the Requirements

for the Degree of

Doctor of Philosophy

The University of Texas at Austin

December, 2015

Dedication

To my grandparents.

Acknowledgements

I would like to thank my supervisor, Dr. Mojdeh Delshad, for her invaluable help and guidance during the last five years. I would like to thank my committee members, Dr. Gary A. Pope, Dr. Kamy Sepehrnoori, Dr. Chun Huh, and Dr. Mary F. Wheeler, for their suggestions and help. Especially I would like to express my gratitude to Dr. Mojdeh Delshad and Dr. Kamy Sepehrnoori for giving me the opportunity to study in this graduate program!

I would also like to thank Dr. Harry L. Chang and Dr. Jieyuan Zhang for the help they provided during my internships with Chemor Tech International LLC, where I gained practical experience on chemical EOR projects. I would also like to thank Dr. Yahan Yang and Dr. Xiaochen Wang for their guidance during my internship with Exxon Mobil Upstream Research Company. I am thankful to Dr. Li Ji and Dr. Bo Gao for helping me build up my connections.

I am indebted to my current and former officemates, Hariharan Ramachandran, Dr. Haishan Luo, Dr. Xianhui Kong, Dr. Haomin Xu, Peter Wang, Dr. Mohammad Lotfollahi, Venkateswaran Pudugramam, Neil Rodrigues, Luis Lamas, Sophie Dufour *et al*. They have been always ready to help me whenever I have a question. I am also grateful for many others who helped me during my studies!

I am thankful for the funding from the Chemical EOR JIP sponsors and the Chevron-UT Enhanced Oil Recovery Alliance, and also the support from Joannna L. Castillo and the Sciencesoft Ltd.

Finally, I would like to thank my family for their love and support!

Modeling and Simulation of Polymer Flooding Including the Effects of Fracturing

Zhitao Li, Ph.D.

The University of Texas at Austin, 2015

Supervisor: Mojdeh Delshad

Chemical enhanced oil recovery (EOR) technology has attracted increasing interest in recent years with declining oil production from conventional oil reserves. Water flooding of heterogeneous reservoirs with viscous oil leaves considerable amount of remaining oil even at high producing water cuts. Polymer flooding is a mature EOR technology for augmenting recovery of moderately viscous oil. Water soluble polymers are used to reduce water mobility and improve sweep efficiency. For very viscous oil, polymer flooding is a potential non-thermal approach for minimizing viscous fingering and improving both displacement sweep efficiency and volumetric sweep efficiency. Polymer manufacturing techniques has been significantly advanced since 1980's, which provides improved polymer quality and keeps polymer price relatively low. Compared with unconventional oil recovery techniques such as hydraulic fracturing, well planned and optimized polymer flooding can be profitable even at pessimistic oil price. It is thus crucial to have a reservoir simulator that is able to accurately model polymer properties and simulate polymer flooding in complex reservoir systems.

Polymer rheological behavior is dependent on polymer molecular structure, concentration, Darcy velocity, brine salinity, hardness, permeability, porosity, etc. We improved polymer rheology modeling for heterogeneous reservoirs where permeability varies for orders of magnitude. For an injection well, a large portion of pressure drop is

lost near wellbore where apparent polymer viscosity as a function of Darcy velocity varies drastically. Conventional analytical well models fail to capture the non-Newtonian effect of apparent polymer viscosity and make injectivity predictions widely deviated from true solutions especially for coarse-grid simulations. We developed a semi-analytical polymer injectivity model and implemented it into UTCHEM. This model is able to handle both shear-thinning and shear-thickening polymer rheology. It successfully avoids the grid effect and matches fine-grid simulation results and analytical solutions. Another challenge is to model polymer injectivity under fracturing conditions. To maintain an economic polymer injection rate, wellbore pressure may exceed the fracture initiation pressure. We developed a framework to couple a fracture model with UTCHEM. This coupled simulator is able to model fracture propagation during polymer injection. Finally several simulation studies were conducted to show the impacts of polymer rheological behavior, loss of polymer into aquifer, near wellbore effect and fracture propagation.

Table of Contents

List of Tables

List of Figures

Chapter 1: Introduction

This chapter presents research motivation, literature review, and dissertation outline.

1.1 MOTIVATION

Chemical enhanced oil recovery (CEOR) is defined as an EOR process using the injection of a combination of chemicals such as alkaline, polymer, surfactant, and cosolvent. The main mechanisms include mobility control and interfacial tension reduction, which contribute to both volumetric sweep efficiency and displacement sweep efficiency (Lake, 1989; Green and Willhite, 1998).

Polymer is a viscosifier used as a mobility control agent for CEOR processes such as polymer flooding (P), surfactant/polymer flooding (SP), alkaline/surfactant/polymer flooding (ASP). The apparent viscosity of a polymer solution in porous media depends on its concentration, polymer size/structure, brine salinity, velocity, pore size/structure, and temperature (Sorbie, 1991). Hydrolyzed polyacrylamide (HPAM), a synthetic polymer, is currently the only widely used polymer in commercial-scale chemical flood applications, and has achieved considerable successes. Synthetic polymers have flexible structures. They are sensitive to brine salinity and hardness, and are also susceptible to mechanical and thermal degradation, which refer to the instability of polymer molecules due to high flow rate and high temperature respectively (Sorbie, 1991; Audibert and Argillier, 1995). Biopolymers, e.g. Xanthan gum, have a more rigid structure and are less susceptible to brine salinity/hardness, thermal or mechanical degradation. Recently, biopolymers have re-gained attention for offshore applications or in harsh environments of high salinity, high hardness and/or high temperature (Kulawardana *et al*., 2012).

For the injection of polymer solutions into porous media during chemical flooding processes, an important concern is the capability of maintaining economic polymer injection rates, in which polymer rheology plays an essential role. Polymer solutions have complex rheological behaviors in porous media. Laboratory coreflood studies show that HPAM solution behaves Newtonian/shear-thinning at low flow velocities and shear-thickening after flow velocity reaches a critical onset value referred to viscoelastic rheology. For field applications, at designed injection rate for viscous HPAM solutions, flow velocity can easily exceed the critical onset velocity in the near-wellbore region, which means a drastic increase in the apparent viscosity of polymer solutions (Li & Delshad, 2014). The onset of shear-thickening behavior may lead to excessive wellbore pressure and limit polymer injectivity. It could also cause severe mechanical degradation of polymer molecular. To the contrary of HPAM, biopolymers such as xanthan gum solution only show shear-thinning behavior in porous media. The apparent viscosity of shear-thinning fluids has a high Newtonian plateau at low flow velocities and a low Newtonian plateau at high flow velocities. Between these two plateaus, the viscosity decreases following a power law as flow velocity increases (Balhoff, 2005). For practical field injection rates, flow velocity in the vicinity of wellbore is relatively high and the apparent viscosity of a biopolymer solution falls into the low Newtonian plateau or the power law regime. So the shear-thinning behavior reduces polymer viscosity near wellbore and is beneficial to polymer injectivity.

There are some ongoing polymer field tests where the field injectivities differ significant from simulation forecasts and analytical calculations. Unexpected high injectivities of HPAM solutions have been observed in some fields at acceptable levels of polymer mechanical degradation (Kumar *et al*., 2012; Manichand *et al*., 2013), which contradicts the predictions from chemical flooding simulation results based on laboratory

measurements. One possible explanation is that when HPAM solution is injected into porous media in the field, wellbore pressure may increase above the rock parting pressure at which fracture initiates from the wellbore. The creation of a fracture at the injection well causes the contact area, where polymer solutions enter the formation from the wellbore, to increase by several folds. This would greatly decrease the flow velocity near wellbore and also shift the rheological regime from thickening to shear-thinning/Newtonian for HPAM solutions. During polymer injection process, dynamic fracture growth helps to maintain the injectivity as the front of polymer solutions propagates in the reservoir (Suri *et al*., 2009; Seright *et al*., 2009; Khodaverdian *et al*., 2010; Lee *et al*., 2011; Suri *et al.*, 2011; Zechner *et al*., 2014).

Although polymer flooding is a mature chemical EOR processes that has been studied and practiced for many years (Chang, 1978), modeling polymer injectivity is a long-standing problem and still challenging in several aspects. Firstly, in conventional reservoir simulation, analytical well models, e.g. Peaceman's well model (Peaceman, 1983), relate wellblock pressure, wellbore pressure, and geometric factors such as wellbore radius and grid size. A basic assumption for these models is that fluid viscosity is Newtonian (i.e. viscosity is constant as the flow rate changes).

However, that apparent viscosity of polymer solutions is a function of flow velocity and flow velocity decreases drastically as the distance away from the injection well increases. In numerical simulations, as the size of a wellblock increases, the average velocity of the wellblock smears, and thus the apparent viscosity of the wellblock is erroneously calculated. Therefore reservoir simulators using well models based on Newtonian fluid assumption often predict unrealistic well injectivity. Another issue with modeling polymer injectivity is how to include the effect of dynamic fracture growth during polymer injection. This requires coupling of an existing chemical flooding

simulator with dynamic fracture models. Very few reservoir simulators can model both dynamic fracture growth and chemical flooding processes. Other issues affecting polymer injectivity include polymer degradation, polymer adsorption, etc. They bring additional uncertainties and complexities to constructing a precise model for polymer injectivity predictions.

In recent years, polymer flooding has also attracted interest for improving oil recovery of heavy oil reservoirs, which requires polymer solutions of high concentrations and high molecular weights. These polymers may show strong viscoelastic effect and reduce residual oil saturation after waterflooding (Koh, 2015; Lee, 2015; Qi *et al.*, 2016). In addition, possible presence of active aquifer in offshore heavy oil reservoirs may cause polymer loss which decreases the economic attractiveness of polymer flooding. Applying polymer flooding in heavy oil reservoirs with active aquifer influxes requires careful simulation studies to optimize field development strategy. So it is crucial to model the polymer viscoelastic effect and impact of active aquifer influxes, which present new challenges to polymer flooding simulations.

UTCHEM is a 3D, multicomponent, multiphase, compositional reservoir simulator which was developed in The University of Texas at Austin (Delshad *et al*., 2000). It is capable of modeling chemical flood processes involving polymer rheology, complex phase behaviors of surfactant-brine-oil system, reaction of acidic oil with alkaline, and geochemical reactions. For simulating polymer flooding using UTCHEM, it was observed that calculated polymer injectivity is sensitive to grid size of the wellblock (Sharma, 2011). The solution in UTCHEM to correct the "grid effect" was to use an effective radius to modify the flow velocity in the wellblock. However, this approach is empirical and impractical for large-scale field simulations with several hundred wells. Another issue with UTCHEM is that though fracture growth plays an indispensable role

in polymer injectivity modeling, there is no dynamic fracture model in UTCHEM. In addition, modeling polymer flooding in a heavy oil reservoir with an active aquifer requires an accurate description of aquifer strength and polymer viscosity. The focus of this research is on modeling of polymer flooding in order to improve polymer injectivity predictions, which are long-existing simulation problems, and also accommodate the recently emerged need of simulating polymer flooding in a heavy oil reservoir with an active aquifer.

1.2 LITERATURE REVIEW

1.2.1 Modeling and Simulation of Polymer Flooding

Zeto (1968) developed a 3D numerical simulator to model polymer flooding in both homogeneous and heterogeneous reservoirs. Polymer was treated to be miscible with water. Simulation studies showed that compared to water flooding, polymer flooding improved vertical sweep efficiency for layered reservoirs with high permeability contrast even at a watered-out stage. Slater and Farouq-Ali (1970) included the effect of polymer on reducing mobility of water in their simulator and showed both numerically and experimentally that polymer improved area sweep efficiency especially for highly unfavorable pattern floods.

Bondor *et al*. (1972) modeled polymer rheological behavior in complex reservoirs using a modified Blake-Kozeny model for power flaw fluids. They also emphasized the importance of near wellbore polymer rheology and its effect on polymer injectivity. They modified their well model using an apparent skin factor determined by an integral of the non-Newtonian viscosity profile for radial flow around the wellbore. However, their well model was based on the assumption that the wellblock pressure should be equal to the areal average pressure (van Poolen *et al*., 1969), which was later proved to be incorrect

by Peaceman (1978). Thus the predicted skin factor based on this well model was questionable. Other polymer properties modeled in the simulator by Bondor *et al.* (1972) included non-ideal mixing of polymer and water, polymer adsorption, and permeability reduction due to polymer adsorption on rock materials.

Goudarzi *et al*. (2013) summarized basic components for polymer modules in several simulators including UTCHEM, CMG-STARS (Computer Modeling Group Ltd, 2013), ECLIPSE (Schlumberger, 2010). Basic functions in a polymer module include models for: polymer viscosity as a function of concentration and shear rate, adsorption, permeability reduction, inaccessible pore volume, salinity and hardness effect on viscosity, etc.

Verma *et al*. (2009) modeled polymer flood in an Exxon's in-house unstructured grid simulator, EM^{power}. Yuan (2010) added the polymer module into the Integrated Parallel Accurate Reservoir Simulator (IPARS) (Wheeler, 2002), to utilize its capability for large-scale parallel simulations. Clemens *et al.* (2011) modeled polymer flooding using streamline simulation technique and achieved significant improvement in computational efficiency. Other noticeable work includes modeling 1D polymer flooding process using generalized fractional flow theory based on extensions of the Buckley-Leverett theory for waterflooding (Pope, 1980), and the chemical flooding EOR forecasting model for predicting chemical flood performance by Mollaei *et al*. (2013).

Accurately modelling of in-situ polymer rheology is important for predicting polymer flood performance. In-situ polymer shear-thinning behavior is commonly modeled with shear-thinning models (e.g., power law model) using an equivalent shear rate derived from capillary bundle model (Lake 1989; Sorbie 1991). There are also several shear-thickening rheological models for synthetic polymer solutions at high shear rates (Hirasaki and Pope, 1974; Haas and Durst, 1981; Heemskerk *et al*., 1984; Masuda *et*

al., 1992; Ranjbar *et al*., 1992; Han *et al*., 1995; Stavland *et al*., 2010). The unified viscosity model developed by Delshad *et al.* (2008) was validated systematically against several other models and also successfully matched the apparent viscosity over a wide range of shear rate for several polymers of interest.

Comprehensive chemical flood simulators such as UTCHEM, CMG-STARS, etc. can be used to simulate complex chemical flood processes (Saad, 1989) including surfactant-polymer, alkaline-polymer, and alkaline-surfactant-polymer flooding. Kong *et al.* (2015) conducted a pilot case simulation study to show the benefits of adding polymer to Water Alternating Gas (WAG) process. Luo *et al*. (2015) improved the geochemical module in UTCHEM to more accurately simulate processes such as alkaline-surfactant-polymer, low-salinity, and low salinity polymer flooding (Skauge and Shiran, 2013) in which geochemical reactions play a critical role.

1.2.2 Modeling Dynamic Fracture

Clifton (1989) summarized three key governing equations for a comprehensive solution to a fracture propagation problem as follows: (1) an elasticity equation that determines the fracture shape with the fluid pressure on the fracture face and rock properties; (2) a fluid-flow equation that determines the fluid pressure distribution from the wellbore to the fracture tip; and (3) a propagation criterion that determines the fracture extension/shrinkage.

Two-dimensional fracture models assume a fracture of a specified height but variable lengths and widths. Perkins and Kern (1961) introduced a two-dimensional fracture model which was further developed by Nordgren (1972). This model is now known as the PKN model, and it assumes plain strain in vertical directions. Another popular two-dimensional model is the GdK model originated from the work by

Khristianovich and Zheltov (1955) and the improvement by Geertsma and de Klerk (1959). This model assumes plain strain in horizontal directions. The PKN model is a good approximation when the fracture length to height is large while the GdK model works better when the ratio is small.

A real 3D fracture model imposes no assumption on the orientation of fracture growth and is computational prohibitive in applicable reservoir simulations (Economides, 2000). A pseudo-3D fracture model assumes fracture height small enough compared with the fracture length so that calculations of the deformations of cross-sections perpendicular to the fracture orientation can be treated independently from the fracture length (Clifton, 1989).

Gadde and Sharma (2001) coupled a single well model (UTWID) with UTCHEM. A vertical PKN-type fracture is attached to the well. Uniform one-dimensional fluid leak-off along and perpendicular to the two fracture faces is assumed. Fracture geometry is assumed to be pseudo-static for any given times during a reservoir simulation. Fracture half-length is the key unknown variable constraint by an interval between the wellbore radius and the maximum fracture half-length. By checking if pressure at fracture tip satisfies the fracture propagation criterion, the interval is halved every iteration until an acceptable accuracy is reached. Thermoelastic effect on stress calculations has been taken into account using Perkins and Gonzalez model (Perkins and Gonzalez, 1985). Pore plugging due to fines in the injected water has been modeled.

Ji *et al*. (2004) proposed a dynamic transmissibility modification method which uses one common grid system to model fracture growth in a reservoir simulator. This model avoids the possible singularity problem in conventional fracture models using a mass balance constraint for fluids in fractures, since fractures with high fluid leak-off rates may be much smaller than the injected fluid volume. Ji *et al*. (2009) developed a

novel model with iteratively coupled reservoir simulation, geomechanics, and fracture propagation. Fracture initiation has been considered. When fracture propagates, related simulation nodes are released in the finite-element geomechanical simulation model. Fracture geometry is used as an input for transmissibility modifications in the reservoir simulation part. Fluid pressures from reservoir simulation are output into the geomechanical simulation part to solve strain and stress fields. The simulation process is iterated until the fracture propagation criterion is satisfied. The main capability of this coupled model is hydraulic fracture modeling involving strong coupling of the effects of geomechanics, fracture propagation and reservoir fluid flow.

Singh (2014) coupled a geomechanical model and fracture propagation with IPARS. In his dissertation, he systematically compared several schemes to couple fracture and reservoir flow including the average permeability method to represent fracture by increasing the average permeability of reservoir block, the meshed-in scheme to represent fracture using very-fine grids, and the interface scheme to represent fracture as a flow boundary. This coupled simulator was used to study fracture propagation "during slickwater injection for single and multistage fracturing scenarios" (Wick et al., 2015).

Lee *et al.* (2011) and Lee (2012) coupled a fracture growth model with CMG-STARS to model fracture growth due to particle plugging, polymer injection and thermal stresses. They emphasized the effects of polymer rheology on injectivity and fracture growth. Ma (2015) modified CFRAC developed by Dr. Mark McClure and Dr. Roland Horne at Stanford University for modeling fracture growth and discrete fracture network to include the capability of modeling polymer injection, and observed earlier fracture initiation for shear-thickening polymer than shear-thinning polymer.

1.3 DISSERTATION OUTLINE

In the first chapter, we discuss the challenges in modeling and simulation of polymer flooding including near wellbore effect of polymer rheology, fracture propagation, and impact of aquifer influx. We also briefly review some previous work by other researchers.

In the second chapter, basic UTCHEM formulations including governing equations, well models, numerical treatment of boundary conditions, and existing polymer module are presented.

In the third chapter, several numerical enhancements to existing UTCHEM models are introduced for improving the accuracy, robustness and computational efficiency of the program.

In the fourth chapter, we describe an analytical injectivity model for polymer solutions to eliminate the grid effect on fluid velocity and the apparent viscosity calculation. This model is able to handle both shear-thinning and shear-thickening polymer rheology. An apparent skin factor model is also discussed for correcting polymer injectivity estimation without modifying simulation codes.

In the firth chapter, we present a methodology to couple a fracture propagation model with an existing reservoir simulator to investigate polymer injectivity under fracturing conditions.

In the sixth chapter, we conduct simulation studies using the enhanced UTCHEM simulator and discuss the effect of polymer rheology, aquifer influx, fracture propagation, etc.

In the seventh chapter, we summarize the findings and accomplishments of this research and provide suggestions for future work.

Chapter 2: UTCHEM Formulation

UTCHEM is a three-dimensional, IMPEC-type (Implicit Pressure and Explicit Concentration), block-centered finite difference, compositional simulator. The governing equations of this model consist of a system of hyperbolic conservation equations for mass/concentration and one parabolic pressure equation. A hyperbolic conservation equation for energy is also included for non-isothermal applications, which will not be our focus in this study.

Modeling chemical EOR processes often require high order differencing in space to capture flood fronts for injected chemicals such as polymer, surfactant, alkaline, ions, etc. In UTCHEM, both second-order and third-order differencing schemes are implemented. Besides, a Total Variation Diminishing (TVD) method combined with a flux limiter is used to control numerical oscillations (Liu et al., 1994).

As one of the most comprehensive chemical flooding simulator, UTCHEM is able to model heterogeneous permeabilities, three-phase relative permeabilities, dispersion, capillary desaturation, phase behavior of surfactant-brine-oil mixtures, surfactant/polymer adsorption, polymer/microemulsion rheology, permeability reduction, and geochemical reactions.

In this chapter, we briefly review basic mathematical formulations in UTCHEM covering governing equations, well models, numerical treatment of boundary conditions, and existing polymer flooding module.

2.1 GOVERNING EQUATIONS

2.1.1 Mass Conservation Equations

The mass conservation equation for each component is given as

$$\frac{\partial}{\partial t}\left(\phi\tilde{C}_\kappa\rho_\kappa\right)+\nabla\cdot\left[\sum_{l=1}^{n_p}\rho_\kappa\left(C_{\kappa l}\vec{u}_l-\vec{\tilde{D}}_{\kappa l}\right)\right]=R_\kappa \qquad [2.1]$$

where ϕ is the porosity, $\tilde{C}_\kappa$ is the overall volume fraction of the κ-th component per unit pore volume, ρ_κ is the component density, $C_{\kappa l}$ is the volume fraction of the κ-th component in the l-th phase, $\vec{u}_l$ is the Darcy flux or the superficial velocity, $\vec{\tilde{D}}_{\kappa l}$ is the dispersive flux, R_κ is the source terms from the injection/production term, Q_{Tk} and the chemical reaction term, r_k. The injection/production term, Q_{Tk} includes contributions from both wells, Q_k, and reservoir boundary, Q_{Bk}.

In UTCHEM, a naming convention similar to the one proposed by Lake (1989) is adopted. The subscript l is used to denote the phase: when l = 1, it refers to the aqueous phase; l = 2 refers to the oleic phase, l = 3 refers to the microemulsion phase, and l = 4 refers to the gaseous phase. The subscript κ refers to the component. κ = 1, 2, 3, 4, 5, or 6 refers to water (in volume fraction), oil (in volume fraction), surfactant (in volume fraction), polymer (in wt%), anion (in meq/ml), or divalent cations (in meq/ml) respectively. More components are modeled for simulations of complex processes such as geochemical reactions, and biological processes. In this dissertation, we also follow this naming convention.

2.1.2 Pressure Equation

For UTCHEM which is a slightly compressible multiphase flow model, the component density is expressed as

$$\rho_\kappa=\rho^o_{\kappa R}\left[1+c^o_k\left(P_R-P^o_R\right)\right] \qquad [2.2]$$

where $\rho^o_{\kappa R}$ is the constant reference component density at the constant reference pressure P^o_R, c^o_k is the component compressibility, and P_R is the pressure of the reference phase (namely, the aqueous phase in UTCHEM). Besides, the porosity ϕ can be expressed as

$$\phi = \phi^o_R \left[1 + c^o_r \left(P_R - P^o_R \right) \right] \qquad [2.3]$$

where ϕ^o_R is the constant reference porosity at the constant reference pressure P^o_R, and c^o_r is the rock compressibility.

The Darcy flux $\vec{u}_l$ can be calculated from Darcy's law for multiphase flow:

$$\vec{u}_l = -\frac{k_{rl}}{\mu_l} \vec{\vec{k}} \cdot \left(\nabla P_l - \gamma_l \nabla h \right) \qquad [2.4]$$

where k_{rl} is the relative permeability of the *l*-th phase, μ_l is the viscosity, $\vec{\vec{k}}$ is the permeability tensor, P_l is the pressure of the *l*-th phase, γ_l is the specific weight, and h is the depth. The pressure of the *l*-th phase, P_l, can be expressed as the summation of the reference phase pressure, P_R and the capillary pressure, P_{cl}:

$$P_l = P_R + P_{cl} \qquad [2.5]$$

Substituting Eqs. [2.2]~[2.5] into Eq. [2.1] and summing the subsequent equation over all volume-occupying components gives the pressure equation:

$$\phi c_t \frac{\partial P_R}{\partial t} + \nabla \cdot \left(\vec{\vec{k}} \cdot \lambda_{rTc} \nabla P_R \right) = \sum_{\kappa=1}^{n_{cv}} Q_{T\kappa} - \nabla \cdot \sum_{l=1}^{n_p} \left(\vec{\vec{k}} \cdot \lambda_{rlc} \gamma_l \nabla h \right) + \nabla \cdot \sum_{l=1}^{n_p} \left(\vec{\vec{k}} \cdot \lambda_{rlc} \nabla P_{cl} \right) \qquad [2.6]$$

where

$$\lambda_{rlc} = \frac{k_{rl}}{\mu_l} \sum_{\kappa=1}^{n_{cv}} \rho_\kappa C_{\kappa l} \qquad [2.7]$$

and

$$\lambda_{rTc} = \sum_{l=1}^{n_p} \lambda_{rlc} \qquad [2.8]$$

and

$$c_t = c_r^o + \sum_{\kappa=1}^{n_{cv}} c_\kappa^o \tilde{C}_\kappa \qquad [2.9]$$

and n_{cv} is the total number of volume-occupying components. Note that the dispersive flux $\vec{\vec{D}}_{\kappa l}$ and the chemical reaction term r_k have no contribution to the pressure equation.

2.2 WELL MODELS

Wells are treated as source terms or boundaries in reservoir simulation models. For a cylindrical coordinate, a 1D simulation, or a cross-sectional simulation, a well can be treated as an internal boundary in the model. No specific well models are required to capture any sub-cell physics. However in most of the cases, due to the size contrast between a wellbore and its wellblock in a 2D/3D Cartesian/curvilinear coordinate system, a well model is required to relate the difference between wellblock pressure and wellbore pressure to well rate. Roughly speaking, two types of well models are generally used for reservoir simulations. For the first type, analytical formulations are developed to account

for the effects of reservoir rock properties (e.g., permeability contrast in different directions), geometric factors from gridding (e.g., wellbore radius, grid size, grid thickness, well location, well deviation, and partial penetration), and fluid mobility. Analytical well models include work by Peaceman (1983), Babu *et al.* (1989), and Ding (1996). For the second type, the effects of reservoir rock properties and geometric factors are not differentiated but accounted as a whole using an empirical well index for each wellblock. The well index is often treated as an input variable in a reservoir simulator and sometimes treated as a history matching parameter of field well performance.

In UTCHEM, existing well models include:

- The analytical model by Peaceman (1983)
- The analytical model by Babu *et al*. (1989)
- Empirical well index model

Wells can be vertical, horizontal or deviated. Deviated wells are treated as multi-segmented vertical wells. The number of injection wells and production wells are arbitrary for Cartesian grids. Completion intervals, well radius, well index modifiers, and skin factors can be specified as input parameters. Both injection wells and production wells can be rate constraint or pressure constraint. Wells can be shut in or reopen during simulation processes.

2.2.1 Well Index Calculations

The basic equation that relates the difference between wellbore pressure and well block pressure to well rate is derived from Darcy's law and shown below:

$$Q_{l,i_m j_m k_m} = PI_{l,m}\left(P_{wf} + \bar{\gamma}_m \Delta h_{i_m j_m k_m} - P_{l,i_m j_m k_m}\right) \qquad [2.10]$$

where the subscripts, i_m, j_m, and k_m, are the Cartesian coordinates for the m-th well block/segment in the reservoir; $Q_{l,i_m j_m k_m}$ is the well rate of the l-th phase at the m-th well block, and it is the well rate source term in the grid block (i_m, j_m, k_m); $PI_{l,m}$ is the productivity index; P_{wf} is the wellbore pressure at the first well block; $\overline{\gamma}_m$ is the average specific weight of fluid in the wellbore; $\Delta h_{i_m j_m k_m}$ is the relative depth of the m-th well block compared to the first well block calculated from the relative depth of the grid block (i_m, j_m, k_m) and the grid block (i_1, j_1, k_1); and $P_{l,i_m j_m k_m}$ is the m-th well block pressure of the l-th phase and also the l-th phase pressure at the grid block (i_m, j_m, k_m). The productivity index $PI_{l,m}$ is the product of the relative fluid mobility $\lambda_{rl,m}$ and the well index WI_m:

$$PI_{l,m} = \lambda_{rl,i_m j_m k_m} WI_m = \frac{k_{rl,i_m j_m k_m}}{\mu_{l,i_m j_m k_m}} WI_m \qquad [2.11]$$

In this section, we'll briefly show the formulations for well index calculations.

2.2.1.1 Well as Internal Boundary

For a 1D (x-direction) or cross-sectional (x-z) simulation (wells are located at the ends of the reservoir/core), the well index WI_m is calculated as

$$WI_m = \frac{k_{x,i_m j_m k_m} \Delta y_{i_m j_m k_m} \Delta z_{i_m j_m k_m}}{\frac{1}{2} \Delta x_{i_m j_m k_m}} \qquad [2.12]$$

where $\Delta x_{i_m j_m k_m}$ $\Delta y_{i_m j_m k_m}$ and $\Delta z_{i_m j_m k_m}$ are the grid dimensions in x, y, and z directions respectively.

For a cylindrical coordinate (r-z), the well index WI_m is calculated as

$$WI_m = \frac{k_{x,i_m k_m} \Delta z_{i_m k_m}}{\frac{1}{2} \Delta x_{i_m k_m}} \qquad [2.13]$$

Note: in UTCHEM, Eq. [2.13] is only used for explicit rate allocation which will be discussed later. And wellbore pressure in the cylindrical coordinate is set to be the pressure of the nearest reservoir grid block, which is a good assumption for very fine cylindrical grids.

2.2.1.2 Analytical Well Models

In a 2D or 3D simulation, for a well segment parallel to the z direction, the well index WI_m is calculated as

$$WI_m = \frac{2\pi \sqrt{k_{x,i_m j_m k_m} k_{y,i_m j_m k_m}} \Delta z_{i_m j_m k_m}}{\ln \frac{r_{o,m}}{r_{w,m}} + S_m} \qquad [2.14]$$

where $r_{o,m}$ is the equivalent wellblock radius at the m-th wellblock, and S_m is the skin factor.

For Peaceman's well model, the equivalent wellblock radius is given as

$$r_{o,m} = 0.28 \frac{\left[\left(\frac{k_x}{k_y} \right)^{\frac{1}{2}}_{i_m j_m k_m} \Delta y^2_{i_m j_m k_m} + \left(\frac{k_y}{k_x} \right)^{\frac{1}{2}}_{i_m j_m k_m} \Delta x^2_{i_m j_m k_m} \right]^{\frac{1}{2}}}{\left(\frac{k_x}{k_y} \right)^{\frac{1}{4}}_{i_m j_m k_m} + \left(\frac{k_y}{k_x} \right)^{\frac{1}{4}}_{i_m j_m k_m}} \qquad [2.15]$$

For the well model by Babu *et al*. (1989), the equivalent wellblock radius is computed in a more complex way. Details can be found in UTCHEM-9.0 Technical Documentation (Delshad *et al*., 2000).

Eqs. [2.12] ~ [2.15] are presented for a well segment parallel to the z direction. However, the directional variables x, y and z are interchangeable.

2.2.2 Well Constraints

2.2.2.1 Pressure Constraint

When a well is specified using pressure constraint, the bottomhole pressure of the first well block P_{wf} is set to be constant. The well rate term is equal to the summation of Eq. [2.10] over all phases and can be treated implicitly as

$$Q^{n+1}_{i_m j_m k_m} = \sum_{l=1}^{n_p} PI^n_{l,m} \left(P_{wf} + \overline{\gamma}^n_m \Delta h_{i_m j_m k_m} - P^n_{cl,i_m j_m k_m} - P^{n+1}_{R,i_m j_m k_m} \right) \qquad [2.16]$$

where the superscript n is the time level. n means explicit or value from the previous time step. n+1 means implicit or value to be calculated at current time step. The reference phase (aqueous phase) pressure P_R is then solved implicitly using the discretized form of the pressure equation, Eq. [2.6].

For a pressure-constraint production well, the well rate term for the l-th phase is then calculated as

$$Q^{n+1}_{l,i_m j_m k_m} = PI^n_{l,m} \left(P_{wf} + \overline{\gamma}^n_m \Delta h_{i_m j_m k_m} - P^n_{cl,i_m j_m k_m} - P^{n+1}_{R,i_m j_m k_m} \right) \qquad [2.17]$$

which is converted into the well rate term for each component, Q_κ, and used in the discretized form of the concentration equation, Eq. [2.1].

For a pressure-constraint injection well which has a fixed composition for the injection fluid, the well rate term for the *l*-th phase is forced to be:

$$Q_{l,i_m j_m k_m}^{n+1} = \frac{Q_l}{\sum_{l=1}^{n_p} Q_l} Q_{i_m j_m k_m}^{n+1} \qquad [2.18]$$

where $\frac{Q_l}{\sum_{l=1}^{n_p} Q_l}$ is the phase cut specified for the pressure constraint injection well.

2.2.2.2 Total Rate Constraint

When a well is specified using total rate constraint, the total injection/production rate of the well Q is set to be constant. Assuming that "the potential gradient between the wellbore and the grid block pressure is the same for all the layers of the reservoir" (Delshad *et al*., 2000), the well rate can be allocated explicitly into each well block.

For a total-rate-constraint injection well, the well rate term of the *l*-th phase is calculated as

$$Q_{l,i_m j_m k_m}^{n} = Q_l \frac{\sum_{l=1}^{n_p} PI_{l,m}^n}{\sum_{m=1}^{n_{wb}} \sum_{l=1}^{n_p} PI_{l,m}^n} PI_{l,m}^n \qquad [2.19]$$

where n_{wb} is the total number of wellblocks, and Q_l is the total injection rate of the *l*-th phase. The well rate term is equal to the summation of Eq. [2.19] over all phases:

$$Q^n_{i_m j_m k_m} = \sum_{l=1}^{n_p} Q^n_{l,i_m j_m k_m} \ . \qquad [2.20]$$

For a total-rate-constraint production well, the well rate term is calculated first:

$$Q^n_{i_m j_m k_m} = \sum_{l=1}^{n_p} Q_l \frac{\sum_{l=1}^{n_p} PI^n_{l,m}}{\sum_{m=1}^{n_{wb}} \sum_{l=1}^{n_p} PI^n_{l,m}} \qquad [2.21]$$

where $\sum_{l=1}^{n_p} Q_l$ is the specified total production rate. The well rate term for the *l*-th phase is then calculated as

$$Q^n_{l,i_m j_m k_m} = Q^n_{i_m j_m k_m} \frac{PI_{l,m}}{\sum_{l=1}^{n_p} PI_{l,m}} = Q^n_{i_m j_m k_m} \frac{\lambda^n_{rl,i_m j_m k_m}}{\sum_{l=1}^{n_p} \lambda^n_{rl,i_m j_m k_m}} \qquad [2.22]$$

where $\lambda^n_{rl,i_m j_m k_m}$ is the relative fluid mobility.

The explicit well rate allocation scheme explained above is called the "mobility method". This scheme is only as good as its assumption that "the potential gradient between the wellbore and the grid block pressure is the same for all the layers of the reservoir". For a heterogeneous reservoir that has layered pay zones of permeabilities varying for several orders of magnitude and meanwhile crossflow effect between layers is not strong enough, this assumption may lead to erroneous calculations, which will be

shown in the latter section that presents the implicit well rate allocation scheme or the potential method as an approach of numerical enhancement.

2.2.2.3 Total Oil Rate Constraint

When a production well is specified using total oil rate constraint, the total oleic phase production rate of the well, Q_2, is assumed constant. In this section, we use the mobility method to treat rate allocation explicitly.

For a total-oil-rate-constraint production well, the total well rate is first calculated as

$$Q^n = \frac{\sum_{m=1}^{n_{wb}} \sum_{l=1}^{n_p} PI_{l,m}^n}{\sum_{m=1}^{n_{wb}} PI_{2,m}^n} Q_2 \qquad [2.23]$$

Then the well rate term is calculated as

$$Q_{i_m j_m k_m}^n = Q^n \frac{\sum_{l=1}^{n_p} PI_{l,m}^n}{\sum_{m=1}^{n_{wb}} \sum_{l=1}^{n_p} PI_{l,m}^n} = Q_2 \frac{\sum_{l=1}^{n_p} PI_{l,m}^n}{\sum_{m=1}^{n_{wb}} PI_{2,m}^n}. \qquad [2.24]$$

The well rate term for the *l*-th phase is then calculated as

$$Q_{l,i_m j_m k_m}^n = Q_{i_m j_m k_m}^n \frac{PI_{l,m}}{\sum_{l=1}^{n_p} PI_{l,m}} = Q_2 \frac{PI_{l,m}}{\sum_{m=1}^{n_{wb}} PI_{2,m}^n} \qquad [2.25]$$

Note: Eq. [2.24] is used in the discretized form of the pressure equation and Eq. [2.25] is used in the discretized form of the mass conservation equation.

2.3 BOUNDARY CONDITIONS

When a cylindrical coordinate is adopted, the outer boundary is set to be constant pressure, which is numerically treated as a pressure-constraint production/injection well. There is no flux through the top or bottom boundary.

For models in Cartesian/curvilinear coordinates, the default boundary condition imposed on the mass conservation equations, the pressure equation, and the energy conservation equation are the no flow/no heat flux boundary condition.

When the option for modeling the saturated zone is activated, constant pressures can be specified at the lateral boundaries. Aqueous phase is allowed to enter the lateral boundaries. Concentrations of water, salinity, and divalent cation can be specified.

When the option for modeling vadose zone is activated, atmospheric pressure is set to the top boundary. For lateral boundaries, if saturated zone is not modeled, the entire lateral boundaries are set to be vadose zone and have constant atmospheric pressure. If saturated zone is modeled, then the depths to water table at both lateral boundaries need to be specified. Above the water table, the lateral boundaries are set to be at constant atmospheric pressure; below the water table, constant pressures can be specified.

For non-isothermal applications, fluxes from the lateral boundaries have an impact on the energy conservation equation. The temperature of the influxes is set to be the initial temperature.

Heat loss to the cap rock or the base rock in the reservoir is modeled using the semi-analytical model by Vinsome and Westerveld (1980).

The current model for modeling the saturated zone doesn't consider pressure change. When it is used to model aquifer influxes during reservoir depletion, the strength of the aquifer may appear too strong. Another problem is that the current model cannot be used to model the bottom aquifer. To improve the accuracy of modeling aquifer, a more sophisticated aquifer model needs to be developed and the bottom boundary needs to be considered.

2.4 POLYMER MODULE

When polymer solutions flow through porous media, polymer and rock properties are affected by the interaction between polymer molecule and rock, fluid flow, reservoir brine salinity and hardness, temperature, etc. In the polymer module of UTCHEM, the modeled properties are polymer adsorption, permeability reduction due to polymer adsorption, inaccessible pore volume for polymer traveling in porous media, apparent polymer viscosity and polymer rheology. Polymer degradation due to biological, chemical or physical factors is currently not modeled in UTCHEM.

2.4.1 Bulk Viscosity

Bulk viscosity of a polymer solution depends on polymer molecule size and is also a function of polymer concentration, brine salinity and hardness, and shear rate. Bulk viscosity can be measured with a viscometer. Bulk viscosity of a polymer solution at very low shear rate (zero shear rate viscosity) is modeled using the modified Flory-Huggins equation (Flory, 1953):

$$\mu_p^0 = \mu_w \left[1 + \left(A_{P1} C_{4l} + A_{P2} C_{4l}^2 + A_{P3} C_{4l}^3 \right) C_{SEP}^{S_P} \right] \qquad [2.26]$$

where μ_w (in cp or mPa·s) is the brine viscosity, A_{P1} (in wt%$^{-1}$), A_{P2} (in wt%$^{-2}$), and A_{P3} (in wt%$^{-3}$) are the fitting parameters obtained from matching lab data, and C_{4l} is the polymer concentration (the component number $\kappa = 4$ refers to polymer) in the *l*-th phase in the unit of wt%. $C_{SEP}^{S_P}$ (dimensionless) represents the effect of salinity and hardness on polymer viscosity. The effective salinity for polymer, C_{SEP} (in meq/ml), is defined as

$$C_{SEP} = \frac{C_{51} + (\beta_P - 1) C_{61}}{C_{11}} \qquad [2.27]$$

where C_{51} (in meq/ml) is total anion concentration ($\kappa = 5$) in the aqueous phase ($l = 1$), C_{61} (in meq/ml) is the total divalent cation concentration ($\kappa = 6$) in the aqueous phase, and C_{11} (in volume fraction) is the water concentration ($\kappa = 1$) in the aqueous phase. β_P is a fitting parameter that is usually greater than one because divalent cation has a more pronounced effect on polymer properties than monovalent cation whose concentration is defines as $C_{51} - C_{61}$. S_p is the slope of the reduced polymer viscosity $\frac{\mu_p^0 - \mu_w}{\mu_w}$ vs. C_{SEP} on a log-log plot.

The polymer solution is a shear-thinning fluid in a rheometer: it has a high Newtonian plateau when shear rate is low and a low Newtonian plateau when shear rate is very high. Between these two Newtonian plateaus, the bulk viscosity follows the power law:

$$\mu_p = K \dot{\gamma}^{n-1} \qquad [2.28]$$

where μ_p (in cp) is the bulk viscosity of polymer solution, the dimensionless power law exponent, *n,* is the slope of the linear portion of bulk viscosity vs. shear rate, $\dot{\gamma}$ (in sec^{-1}) plotted on a log-log scale, and the power law coefficient, *K* (in $cp \cdot sec^{n-1}$), can be obtained from the Y-intercept of the plot. The deficiency of the power law model is that it overestimates the viscosity at low shear rates and underestimates the viscosity at high shear rates.

Introducing additional model parameters helps with a better match of the polymer shear-thinning rheology. For example, one popular rheological model is the Carreau model (Carreau, 1968):

$$\mu_p - \mu_\infty = (\mu_P^0 - \mu_\infty)\left[1+(\lambda\dot{\gamma})^2\right]^{(n-1)/2} \qquad [2.29]$$

where μ_∞ (in cp) is the viscosity corresponding to infinite shear rate, μ_P^0 (in cp) is the zero shear rate viscosity which can be modeled using Eq. [2.23], λ (in sec) is a curve-fitting parameter related to the critical shear rate, $\dot{\gamma}_c$ (in sec), shown in Fig. 2.1 and characterizes the transition of rheological regime from the low shear rate Newtonian regime to the power law regime, and n is another curve-fitting parameter. Fig. 2.1 from Sorbie (1990) shows the viscosity comparison of the power law model with the Carreau model. When $\mu_p >> \mu_\infty$ and $\lambda\dot{\gamma} >> 1$, the Carreau model can be approximated using the power law model with $K = \mu_P^0 \lambda^{n-1}$ and the same n for the power law exponent.

In UTCHEM, the shear-thinning polymer rheological behavior is modeled using Meter's equation (Meter and Bird, 1964):

$$\mu_p - \mu_\infty = \frac{\mu_P^0 - \mu_\infty}{1 + \left(\frac{\dot{\gamma}}{\dot{\gamma}_{\frac{1}{2}}} \right)^{P_\alpha - 1}} \qquad [2.30]$$

where $\dot{\gamma}_{\frac{1}{2}}$ (in $\sec^{-1}$) is a fitting parameter and physically the shear rate at which the viscosity is half of the sum of μ_∞ and μ_P^0, and P_α is a dimensionless fitting parameter. When $\mu_p >> \mu_\infty$ and $\dot{\gamma} >> \dot{\gamma}_{\frac{1}{2}}$, the Meter's model can be approximated using the power law model with $K = \mu_P^0 \dot{\gamma}_{\frac{1}{2}}^{P_\alpha - 1}$ and $n = 2 - P_\alpha$.

2.4.2 Polymer Retention

Polymer retention decreases the front speed of polymer concentration as a polymer solution advances and affects the effectiveness of chemical flooding. It is a significant factor for economic analysis of a chemical EOR project. Polymer may adsorb to the surface of the rock. In addition, polymer molecule may also be trapped by porous media when the molecular size is comparable to the pore throat size, which is called "mechanical entrapment" (Sorbie, 1991). Polymer retention increases as rock permeability decreases; higher brine salinity or higher concentration also leads to more polymer adsorption. In UTCHEM, the adsorbed polymer concentration as a function of permeability, brine salinity and hardness, and polymer concentration is modeled using a Langmuir-type isotherm given as

$$\hat{C}_4 = \min\left(\tilde{C}_4, \frac{a_4\left(\tilde{C}_4 - \hat{C}_4\right)}{1 + b_4\left(\tilde{C}_4 - \hat{C}_4\right)} \right) \qquad [2.31]$$

where $\hat{C}_4$ (in wt%) is the adsorbed polymer concentration, which is not greater than total concentration of the dissolved polymer, $\tilde{C}_4$ (in wt%). b_4 (in wt%$^{-1}$) is an adsorption parameter and a_4 is a function of permeability and effective salinity for polymer, C_{SEP}, given as

$$a_4 = \frac{a_{41} + a_{42} C_{SEP}}{\sqrt{\frac{k}{k_{ref}}}} \qquad [2.32]$$

where a_{41} (dimensionless) and a_{42} (in ml/meq) are also adsorption parameters, and k_{ref} is the reference permeability in the unit of millidarcy or darcy at which the experimental data for adsorption are measured. a_{41}, a_{42}, and b_4 can be found by matching lab polymer adsorption data. a_4/b_4 represents the maximum level of adsorbed polymer, and b_4 controls the curvature of the Langmuir-type isotherm (Delshad *et al.*, 2000).

2.4.3 Permeability Reduction

Polymer retention in the rock causes permeability reduction. When adsorbed polymer molecules form a layer on the rock surface, the effective pore size decreases; in addition, polymer molecule may also be trapped in small pore throats which leads to "plugging". Both of adsorption and mechanical entrapment leads to the reduction of the aqueous phase permeability of the rock. In UTCHEM, permeability reduction by polymer retention is modeled using a permeability reduction factor, R_k:

$$R_k \equiv \frac{effective\ permeability\ of\ brine}{effective\ permeability\ of\ \ polymer\ solution} \qquad [2.33]$$

and it is extended to multiple phases and modeled as

$$R_{kl} = 1 + \frac{\left(R_{k\max} - 1\right) b_{rk} C_{4l}}{1 + b_{rk} C_{4l}} \qquad [2.34]$$

where b_{rk} (in wt%$^{-1}$) is a permeability reduction parameter, and the maximum permeability reduction factor R_{kmax} (dimensionless) is given as

$$R_{k\max} = \min\left\{ \left[1 - \frac{c_{rk}\left(A_{p1} C_{SEP}^{S_P}\right)^{\frac{1}{3}}}{\left(\frac{\sqrt{k_x k_y}}{\phi}\right)^{\frac{1}{2}}} \right]^{-4}, R_{kcut} \right\} \qquad [2.35]$$

where c_{rk} (in darcy$^{1/2}$/cp$^{1/3}$) is another permeability reduction parameter, and R_{kcut} is set to be 10 for normal polymer flood applications while it is adjustable for processes involved with gel or lower permeability rocks. Here, $A_{p1} C_{SEP}^{S_P}$ is related to the intrinsic polymer viscosity, $\left[\mu_p\right]$ (in wt%$^{-1}$), which is defined as

$$\left[\mu_p\right] \equiv \lim_{\substack{c_{4l} \to 0 \\ \dot{\gamma} \to 0}} \frac{\mu_p - \mu_w}{c_{4l} \mu_w} \qquad [2.36]$$

Substitution of Eq. [2.26] into Eq. [2.36] gives:

$$\left[\mu_p\right] = A_{p1} C_{SEP}^{S_P} \qquad [2.37]$$

Note: $\left[\mu_p\right]$ is a measure of polymer molecule size and $\left(\frac{\sqrt{k_x k_y}}{\phi}\right)^{\frac{1}{2}}$ is a measure of pore size. Therefore, R_{kmax} is estimated based on the ratio of polymer molecule size to pore size. Since most of polymer exists in the aqueous phase, Eq. [2.34] shows that permeability reduction mainly affects the effective permeability of aqueous phase rather than oleic phase.

For coreflood experiments, the mobility of a displacing phase can be calculated from pressure difference between two ends of the core, core cross-section area, and core length. The capability of reducing the mobility of a displacing phase by a polymer solution compared with a brine solution is the resistance factor, R_F, defined as

$$R_F \equiv \frac{\lambda_w}{\lambda_P} = R_k \frac{\mu_P}{\mu_w} \qquad [2.38]$$

The permeability reduction factor R_{k} can be inferred from the resistance factor, R_F. The effect of permeability reduction by a polymer solution is irreversible. The residual resistance factor, R_{RF}, is defined as the brine mobility ratio before and after polymer flooding. For a completely irreversible permeability reduction process, R_k is equal to R_{RF}.

2.4.4 Inaccessible Pore Volume

Small pores of sizes comparable to or smaller than polymer molecules are likely inaccessible to them. Besides, when polymer molecules flow through pores, there is the "wall exclusion effect" that forces polymer molecules to keep away from the rock surface. The concept of inaccessible pore volume based on these two effects has been used to explain that in some coreflood experiments, polymer molecules travels faster than

water, ion or ideal tracers, although the front of polymer concentration is retarded by polymer retention.

Inaccessible pore volume is modeled using a constant input parameter as an effective porosity to polymer, ϕ_e in the mass conservation equation for polymer species instead of actual porosity.

2.4.5 Apparent Polymer Viscosity

The apparent viscosity, μ_{app}, is a macroscopic concept defined using Darcy's law for single phase non-Newtonian fluids (Sorbie, 1991). By excluding the permeability reduction effect and considering μ_{app} as the pure viscous effect part of polymer solutions, μ_{app} is defined (in Darcy, CGS or SI units) as

$$\mu_{app} \equiv \frac{k}{R_k}\frac{\nabla P}{u} \qquad [2.39]$$

2.4.5.1 Polymer Rheology in Porous Media

For flow in porous media, polymer rheological behavior is complicated by the existence of tortuous structures of porous media. To represent the structures of porous media, the capillary bundle model (Lake, 1989; Sorbie, 1991) was proposed to approximate a porous medium using a bundle of capillary tubes.

The simplest capillary bundle model uses a bundle of uniform capillary tubes. Here we recap the methodology in CGS units detailed by Lake (1989):

For a tortuous capillary tube of length L_t and radius R, the Hargen-Poiseuille equation for a single-phase laminar Newtonian flow in a circular pipe gives:

$$q = \frac{\pi R^4}{8\mu}\frac{\Delta\Phi}{L_t} \qquad [2.40]$$

where q is the volumetric flow rate, μ is the Newtonian viscosity, and $\Delta\Phi$ is the potential difference between the ends of the tube. In CGS units, q is in cm^3/s, R in cm, $\Delta\Phi$ in barye or $g/(cm \cdot s^2)$, L_t in cm, and μ in poise or $g/(cm \cdot s)$. Then the average velocity (in cm/s) through the tube cross section is

$$\bar{v} = \frac{q}{\pi R^2} = \frac{R^2}{8\mu}\frac{\Delta\Phi}{L_t} \qquad [2.41]$$

For a one-dimensional core, Darcy's equation for single phase Newtonian flow (in cm/s) gives:

$$u = \frac{k}{\mu}\frac{\Delta\Phi}{L} \qquad [2.42]$$

where L (in cm) is the length of the core, and k is the permeability (in cm^2).

The travel time of a fluid element in a capillary tube is $L_t / \bar{v}$, and the travel time in a core is $L/(u/\phi)$. Assuming they are equal, we can get from Eq. [2.36] and Eq. [2.37]:

$$R = \sqrt{\frac{8k}{\phi}\left(\frac{L_t}{L}\right)^2} = \sqrt{\frac{8k}{\phi}\tau} \qquad [2.43]$$

where τ is defined as the tortuosity of the rock.

The approach by Lake (1989) explained above can be used to derive the analytical form of the apparent polymer viscosity. For a tortuous capillary tube of length L_t and

radius R, the Hargen-Poiseuille equation for single-phase laminar non-Newtonian flow of a power-law fluid in a circular pipe gives (Sorbie, 1991):

$$\bar{v} = \frac{n}{3n+1} R^{\frac{n+1}{n}} \left(\frac{\Delta\Phi}{2KL_t} \right)^{\frac{1}{n}} \qquad [2.44]$$

where K (in g/(cm·s)·s^{n-1}) and n are the power law parameters, and $\bar{v}$ (in cm/s) is the average velocity through the tube cross section. For a one-dimensional core, Darcy's equation for single phase non-Newtonian flow of a power-law fluid gives:

$$u = \frac{k}{\mu_{app}} \frac{\Delta\Phi}{L} \qquad [2.45]$$

Substitution of Eq. [2.45] and Eq. [2.43] into Eq. [2.44] and assuming $L_t / \bar{v} = L/(u/\phi)$ gives:

$$\mu_{app} = Hu^{n-1} \qquad [2.46]$$

where H (in g/(cm·s)·(cm·s)$^{n-1}$) is

$$H = \left[2\left(\frac{3n+1}{n} \right)^n \left(\frac{8k}{\phi} \right)^{-\left(\frac{n+1}{2}\right)} k\phi^{-n} \right] K \qquad [2.47]$$

If the apparent viscosity is calculated from the power-law form below:

$$\mu_{app} = K\dot{\gamma}_{eq,capil}^{n-1} \qquad [2.48]$$

Then the equivalent shear rate for the capillary bundle model is calculated as

$$\dot{\gamma}_{eq,capil} = \left(\frac{3n+1}{4n}\right)^{\frac{n}{n-1}} \frac{4|u|}{\sqrt{8k\phi}} \qquad [2.49]$$

where $\dot{\gamma}_{eq,capil}$ is in sec^{-1}, $|u|$ is in cm/s, and k is in cm^2. Note: the tortuosity term τ is canceled out in the derivations. Our analytical solution is consistent with that by Teeuw & Hesselink (1980), contrary to other derivations (Hirasaki & Pope, 1974; Sorbie, 1991) which has a tortuosity term in their final expressions.

A porous medium differs from a bundle of uniform capillary bundles from several aspects (Teeuw and Heeselink, 1980; Cannella *et al.,* 1988): 1. Pores in the porous medium have various shapes while in the uniform capillary bundle model, capillary tubes are assumed to be circular; 2. Pore size in the porous medium has a distribution while in the uniform capillary bundle model, capillary tubes are assumed to be of the size; 3. Pores are interconnected while in the uniform capillary bundle model, capillary tubes are assumed to be not interconnected. Flow in porous media has fluctuating rates when fluids go through small throats and large pores. Besides, the wall exclusion from the rock surface due to the size of polymer molecule may result in a depleted layer of lower polymer concentration near the rock surface, and enhances the flow velocity of polymer solutions (Sorbie, 1990). A simple way to correct the deviation of a "real" porous medium from the ideal uniform capillary bundle model is to introduce a shear rate correction factor or shear rate coefficient, C as shown below:

$$\dot{\gamma}_{eq} = C\left(\frac{3n+1}{4n}\right)^{\frac{n}{n-1}} \frac{4|u|}{\sqrt{8k\phi}} \qquad [2.50]$$

where $\dot{\gamma}_{eq}$ is an empirical form of Eq. [2.49] and C should be a function of permeability, porosity, polymer molecule properties, etc. In UTCHEM, we follow the treatment by Cannella *et al*. (1988) to extend Eq. [2.50] to multiphase flow:

$$\dot{\gamma}_{eq} = C\left(\frac{3n+1}{4n}\right)^{\frac{n}{n-1}} \frac{4|\vec{u}_l|}{\sqrt{8\bar{k}k_{rl}\phi S_l}} \qquad [2.51]$$

where the magnitude of average Darcy velocity, $|\vec{u}_l|$ (in cm/s), is calculated as

$$|\vec{u}_l| = \sqrt{u_{xl}^2 + u_{yl}^2 + u_{zl}^2} \qquad [2.52]$$

and the average permeability is calculated as

$$\bar{k} = \left[\frac{1}{k_x}\left(\frac{u_{xl}}{|\vec{u}_l|}\right)^2 + \frac{1}{k_y}\left(\frac{u_{yl}}{|\vec{u}_l|}\right)^2 + \frac{1}{k_z}\left(\frac{u_{zl}}{|\vec{u}_l|}\right)^2\right]^{-1} \qquad [2.53]$$

The term $\left(\frac{3n+1}{4n}\right)^{\frac{n}{n-1}}$ is bounded within a small range of 0.78 to 1 for n values in the range of 0 to 1. Assuming n = 0.7, which is a typical value for non-Newtonian polymer solutions, gives $\left(\frac{3n+1}{4n}\right)^{\frac{n}{n-1}} \frac{4}{\sqrt{8}} = 1.1153$. Theoretically, the effects of inaccessible pore volume and permeability reduction need to be included in Eq. [2.51].

However, it is hard to differentiate these effects with the shear rate correction factor, C, practically from experimental results. Thus in UTCHEM, Eq. [2.51] neglects these effects. A further conversion of the CGS untis ($|\vec{u}_l|$ in cm/s, and $\bar{k}$ in cm^2) to the English units in UTCHEM ($|\vec{u}_l|$ in ft/d, and $\bar{k}$ in darcy) gives:

$$\dot{\gamma}_{eq} = \frac{\gamma_c |\vec{u}_l|}{\sqrt{\bar{k} k_{rl} \phi S_l}} \qquad [2.54]$$

where $\gamma_c \left(= 3.96C\right)$ is the shear correction factor (GAMMAC) in UTCHEM.

In UTCHEM, shear-thinning behavior of polymer solutions in porous media is modeled using either Meter's or Carreau models. The Meter's equation (Meter and Bird, 1964) is described as

$$\mu_{app} - \mu_\infty = \frac{\mu_P^0 - \mu_\infty}{1 + \left(\frac{\dot{\gamma}_{eq}}{\dot{\gamma}_{\frac{1}{2}}} \right)^{P_\alpha - 1}} \qquad [2.55]$$

where the infinite shear rate viscosity, μ_∞, is approximated with brine viscosity. The Carreau model (Eq. [2.26]) can model shear-thinning behavior in porous media by replacing $\dot{\gamma}$ with $\dot{\gamma}_{eq}$.

Polymer solutions of Synthetic polymers such as HPAM show shear-thickening behavior at very high shear rates, which exceeds the modeling capability of shear-thinning models. To solve this problem, Delshad *et al*. (2008) developed a Unified Viscosity Model (UVM) which covers the entire range of shear rate and was implemented in UTCHEM. The apparent viscosity consists of two parts:

$$\mu_{app} = \mu_{sh} + \mu_{el} \qquad [2.56]$$

where the shear-thinning part is using the Carreau model:

$$\mu_{sh} = \mu_{\infty} + (\mu_P^0 - \mu_{\infty})\left[1 + (\lambda_1 \dot{\gamma}_{eq})^2\right]^{(n_1-1)/2} \qquad [2.57]$$

and the shear-thickening or elongational viscosity part is

$$\mu_{el} = \mu_{\max}\left\{1 - \exp\left[-(\lambda_2 \tau_r \dot{\gamma}_{eq})^{n_2-1}\right]\right\} \qquad [2.58]$$

Here, τ_r (in sec) is the relaxation time treated as a function of polymer concentration:

$$\tau_r = \tau_0 + \tau_1 C_{4l} \qquad [2.59]$$

and λ_1 (in sec) is calculated as

$$\lambda_1 = \beta_1 \exp\left(\beta_2 C_{4l}\right) \qquad [2.60]$$

and $\mu_{\max}$ (in cp) is given as

$$\mu_{\max} = \mu_w \left(AP_{11} + AP_{22} \ln C_{pl}\right) \qquad [2.61]$$

and n_1, n_2, β_1 (in sec), β_2 (in wt%$^{-1}$), λ_2, τ_0 (in sec), τ_1 (in sec/wt%), AP_{11}, and AP_{22} are constant fitting parameters for matching experimental data.

2.4.5.2 Shear Rate Correction

By matching experimental data with the capillary bundle model, it is observed that the shear rate correction factor, or the shear rate coefficient, C, is related to polymer type and rock properties such as porosity and permeability (Gogarty, 1967; Wreath, 1990). A correlation proposed by Wreath *et al*. (1990) was implemented in UTCHEM for roughly estimation of C accounting the influence of shear rate, porosity, permeability, and polymer type.

Assuming that the shear-thinning rheology of a polymer solution can be represented by the power law model, we can get:

$$\mu_{app} = K_{core}\dot{\gamma}_{eq,capil}^{n-1} = KK^{*}\dot{\gamma}_{eq,capil}^{n-1} \qquad [2.62]$$

where K^* is an empirical parameter used to correct the deviation between experimental results and the capillary bundle model prediction. K_{core} is the power law coefficient matched from coreflood experimental data and K is the power law coefficient measured using a viscometer. Comparing Eq. [2.62] with Eq. [2.48] ~ Eq. [2. 50] gives:

$$C = \left(K^{*}\right)^{\frac{1}{n-1}} \qquad [2.63]$$

Wreath *et al*. (1990) found that K^* can be correlated with a dimensional group, called the viscosity number:

$$N_v = \frac{\sqrt{kk_{rw}\phi S_w}}{\Theta u^{n-1}} \qquad [2.64]$$

where u is in cm/s, k is in cm^2, and Θ is the relaxation time coefficient and constant for the same type of polymer. N_v has the unit of *cm/s*. The correlation based on experimental observations is given below:

$$K^* = \max\left[0.1, \min\left(1.0, aN_v^b\right)\right] \qquad [2.65]$$

where a and b are fitting parameters. Thus C can be calculated from Eq. [2.63] using the correlated K^*. Fig. 2.2 shows the correlated line for K^* as a function of N_v.

2.4.5.3 Grid Effect and Near Wellbore Correction

Numerical simulation studies (Sharma, 2010; Yuan, 2012) show a strong grid effect when simulating chemical EOR processes using polymer for mobility control. Prediction of polymer injectivity is sensitive to the selection of wellblock grid size. In coarse-grid simulations, high shear rates near wellbore are averaged (Eq. [2.47]) and smear in the coarse well blocks. Synthetic polymer solutions that show Newtonian/shear-thinning behavior at low shear rates and shear-thickening behavior at high shear rates may thus appear only Newtonian/shear-thinning which may give an optimistic estimate of polymer injectivity. In field tests, injecting polymer solutions at a designed injection rate based on those simulation results may cause excessive wellbore pressure above formation parting pressure and induce fractures (Seright *et al*., 2009; Khodaverdian *et al*., 2010; van den Hoek *et al*., 2012; Teklu *et al*., 2012; Clemens *et al*., 2013). However, it is also observed, for biopolymers such as Xanthan, polymer injectivity benefits from the

shear-thinning behavior and may be significantly underestimated due to no correction for the high near-wellbore shear rates (Sorbie *et al*., 1982).

Several methods are proposed to improve the injectivity calculations. Sorbie *et al.* (1982) calculated polymer injectivity for a 2D cross-sectional model through numerical integration of pressure drop for a single-phase shear-thinning polymer flow in a curvilinear wellblock. Buell *et al.* (1990) developed a methodology using the Hall plot for analyzing shear-thinning polymer injectivity data from fields and verified the method with a radial reservoir simulator.

In UTCHEM, an empirical method proposed by Sharma *et al.* (2011) was adopted. The apparent polymer viscosity at a wellblock is treated by assuming that polymer flux rate in a wellblock is equal to the radial flux rate using an effective radius:

$$\left|\vec{u}_l\right|_{i_m j_m k_m} = \frac{Q_{l,i_m j_m k_m}}{2\pi r_{weff} \Delta z_{i_m j_m k_m}} \qquad [2.66]$$

where $\Delta z_{i_m j_m k_m}$ is the thickness of the m-th wellblock or the gridblock (i_m, j_m, k_m), and r_{weff} is an empirical input parameter. This model is specified as a near-wellbore option using the input flag, ISHEAR. ISHAER = 0 means no near-wellbore treatment, and ISHEAR = 1 means using the effective radius for near-wellbore treatment.

Sharma (2010) modeled an inverted 5-spot with a constant-pressure injection well located in the center of a homogeneous and isotropic reservoir. Simulated cases use uniform grid sizes (12 ft, 20 ft, 36 ft, 60 ft, 100 ft, 180 ft, and 300 ft) and polymer rheology is assumed to be shear-thinning only. When no near-wellbore treatment is used (ISHEAR=0), injection rate is plotted for various grid sizes as shown in Fig. 2.3. The legend “300.0.0” stands for 300 ft grid size, ISHEAR=0, and Rweff=0 ft. As the grid size

increases, injection rate decreases. Assuming the injection rate simulated from the case using the grid size of 12 ft is accurate, he tested near-wellbore treatment for the case using the grid size of 300 ft. As shown in Fig. 2.4, the injection rate from the fine-grid model is matched using an effective well radius of 26 ft. Peaceman's well radius was also tested to see if it was a good guess for the effective well radius. Simulation results show that using Peaceman's well radius as r_{weff} significantly underestimates the injectivity.

Simulation studies by Sharma (2010) show that r_{weff} is a complicated function of polymer rheology, grid size, and other factors. In applications, it needs to be determined by matching injectivity of a coarse-grid simulation with fine-grid simulations, which is impractical for large-scale field simulations with several hundred wells.

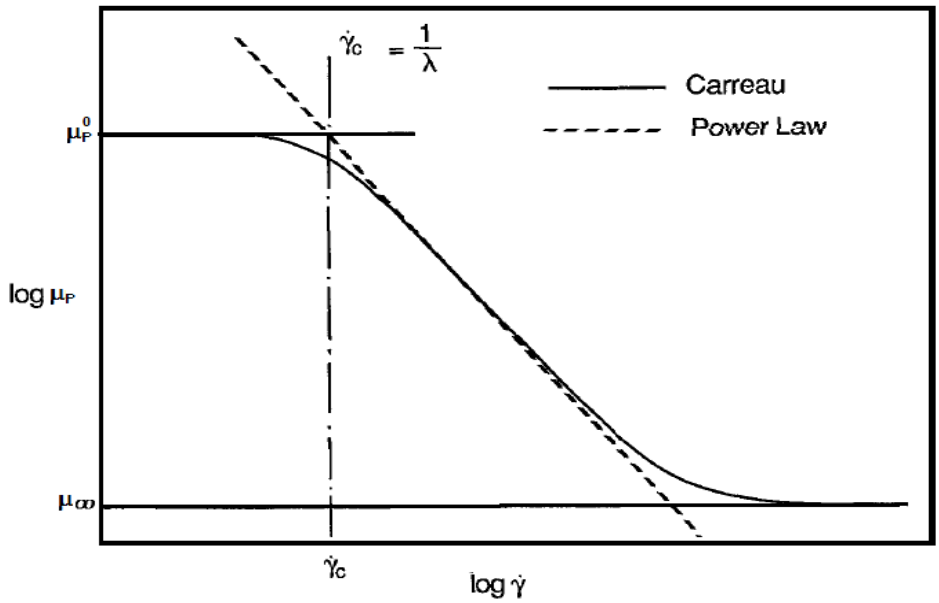

Figure 2.1: Comparison of the power law model with the Carreau model from Sorbie, *Polymer-Improved Oil Recovery*, Chapter 3, Fig. 3.8 (1990).

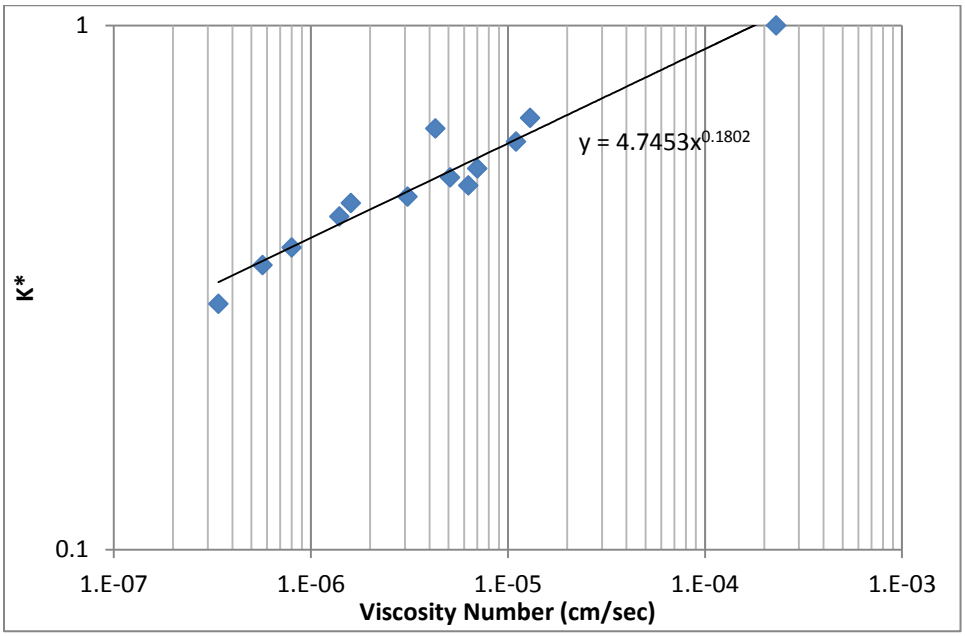

Figure 2.2: K* correlated as a function of viscosity number in log-log scale for n=0.48.

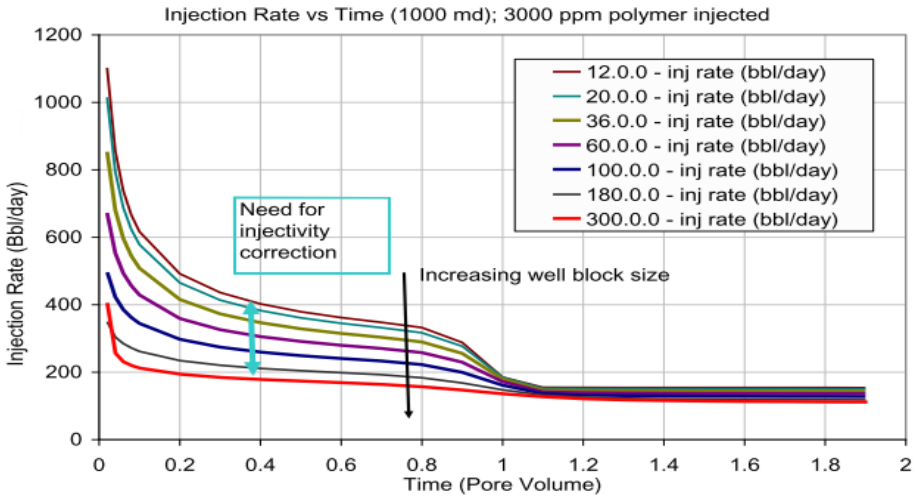

Figure 2.3: Injection rates for various grid sizes (From Sharma, Thesis, *Assessment of Polymer Injectivity during Chemical Enhanced Oil Recovery Processes*, Chapter 3, Fig. 3.4)

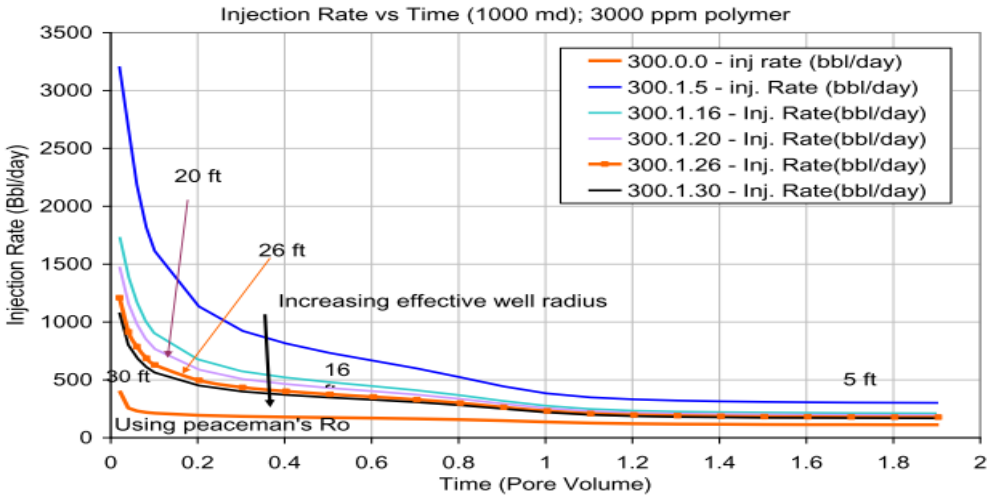

Figure 2.4: Rweff effect on injection rate using ISHEAR=1 for 300 ft well grid size model (From Sharma, Thesis, *Assessment of Polymer Injectivity during Chemical Enhanced Oil Recovery Processes*, Chapter 3, Fig. 3.18)

Chapter 3: Numerical Enhancements[1]

In this chapter, we describe our numerical enhancements to current UTCHEM to improve its accuracy, robustness, and computational efficiency in simulating large-size and heterogeneous reservoir models.

3.1 Implicit Well Rate Allocation Scheme

3.1.1 Analytical Solution and Deficiency of Explicit Well Rate Allocation Scheme

In Chapter 2, we briefly reviewed the mobility method which explicitly allocates well rate for a multi-segmented well specified with a total rate constraint. This explicit scheme may lead to erroneous calculations for heterogeneous reservoirs with limited cross flow between layers of different pay zones.

Polymer flooding is a mature chemical EOR method widely used in heterogeneous reservoirs for improving the volumetric sweep efficiency leading to additional oil recovery. The accuracy of the mobility method for application in heterogeneous reservoirs was examined with the numerical study of polymer flooding of a reservoir simplified with a uniformly heterogeneous horizontal layer-cake model of 2 layers (Lake, 1989). This 2D case is a simplification of many realistic cases which are focused on using polymer to improve the vertical sweep efficiency.

For a reservoir of two horizontal *non-communicating* layers as shown in Fig. 3.1, each layer is uniform in permeability, porosity, and water saturation. The upper layer has a constant isotropic permeability of k_1 and a constant porosity of ϕ_1, and the lower layer

[1] Li, Z., Delshad, M., Lotfollahi, M., Koh, H., Luo, H., Chang, H., Zhang, J., Dempsey, P., Lucas-Clements, C., and Brennan, B., "Polymer Flooding of a Heavy Oil Reservoir with an Active Aquifer", SPE 169149, presented at the *SPE Improved Oil Recovery Symposium*, Tulsa, OK, USA, 12-16 April, 2014. In this work, Li implemented aquifer models, performed simulation studies and wrote the paper. Lotfollahi provided a residual oil reduction model. Koh provided experimental data. Delshad, Luo, Chang, Zhang, Dempsey, Lucas-Clements and Brennan made revisions.

has a constant isotropic permeability of k_2 and a constant porosity of ϕ_2. The displaced phase (reservoir brine) has a saturation of one and a constant viscosity of μ_2, and the displacing phase (polymer solution) has a constant viscosity of μ_1. Given $k_1 > k_2$, more injected fluid is allocated to the upper layer and the displacement front in the upper layer travels faster than that in the lower layer. An analytical solution derived by Lake (1989) gives the fraction of the volumetric flow rate into layer 1:

$$\frac{q_1}{q_1+q_2}=\frac{1}{1+\frac{k_2h_2}{k_1h_1}\left[\frac{M^o+x_{D_1}\left(1-M^o\right)}{M^o+x_{D2}\left(1-M^o\right)}\right]} \qquad [3.1]$$

where x_{D1} is the dimensionless form of x_{f1}, the displacement front location of the displacing phase in the upper layer (Layer 1). $x_{D1}=\frac{x_{f1}}{L}$ where L is the length of the reservoir. x_{D2} and x_{f2} refer to the lower layer (Layer 2). h_1 and h_2 are the layer thicknesses. The end point relative mobility ratio is defined as

$$M^o=\frac{\mu_2 k_{r1}^o}{\mu_1 k_{r2}^o} \qquad [3.2]$$

where k_{r1}^o is the endpoint relative permeability of the displacing phase (polymer solution) and k_{r2}^o is the endpoint relative permeability of the displaced phase (in-situ brine). In our study, we assume that the water saturation is one and the displacing phase is the injected polymer solution. Therefore, the end point mobility ratio is reduced to the viscosity ratio.

The dimensionless displacement front locations, x_{D1} and x_{D2}, are related to each other using the equation below:

$$x_{D1} = 1 + r_{12}\left[\frac{1-M^o}{2}\left(x_{D2}^2 - \left(x_{D2}^0\right)^2\right) + M^o\left(x_{D2} - x_{D2}^0\right)\right] \quad [3.3]$$

where the heterogeneity contrast r_{12} for the single-phase model is defined as

$$r_{12} = \frac{k_1\phi_2}{k_2\phi_1} \quad [3.4]$$

and the dimensionless displacement front position in the lower layer at the polymer breakthrough x_{D2}^0 is calculated as

$$x_{D2}^0 = \frac{\left[\left(M^o\right)^2 + \frac{1-\left(M^o\right)^2}{r_{12}}\right]^{\frac{1}{2}} - M^o}{1-M^o} \quad [3.5]$$

For any given x_{D1} and x_{D2}, the dimensionless time t_D (unit: injected pore volume) is calculated from:

$$t_D = \frac{\phi_1 h_1 x_{D1} + \phi_2 h_2 x_{D2}}{\phi_1 h_1 + \phi_2 h_2} \quad [3.6]$$

For a given x_{D2}, x_{D1}, t_D can then be calculated. Thus we can obtain the fraction of the volumetric flow rate into layer 1, $\frac{q_1}{q_1+q_2}$ as a function of t_D, which

gives us a reference solution for checking the accuracy of the improved well rate allocation scheme.

To validate the "mobility method", we set up an x-z cross-sectional model. The reservoir and fluid properties are given in Table 3.1. The injection rate is at total rate constraint and the production well is at pressure constraint. Polymer solution is assumed to be Newtonian and its apparent viscosity is dependent on concentration only. The simulation result was compared with the analytical solution by Lake (1989) detailed above as shown in Fig. 3.2. Another curve given in Fig. 3.2 is the simulation result by specifying constant pressure conditions for both injection production wells. The results in Fig. 3.2 show that the mobility method leads to erroneous calculations of well rate allocation in the layered reservoir because of its explicitness. So the performance of polymer flooding for improving vertical sweep efficiency is also underestimated. When wells are under pressure-constraint, they are treated implicitly in UTCHEM. UTCHEM gives exactly the same results as the analytical solution does. The problem with the mobility method is because it assumes an equal potential gradient between the wellbore and the gridblock pressure for all the layers in the reservoir model. To improve the accuracy, the potential differences need to be included. This method is called the "potential method". Nolen & Berry (1972) showed that explicitly including the potential differences might result in stability problem.

In summary, it is necessary to develop an implicit well rate allocation scheme for the rate-constraint wells and the potential differences need to be accounted. The analytical solution by Lake (1989) can be used as a reference solution for validation.

3.1.2 Implicit Well Rate Allocation Scheme for Fixed Total Rate

For a multi-segmented well, the well rate is related to the difference between wellbore pressure and wellblock pressure based on the equation derived from Darcy's law:

$$Q_{l,i_m j_m k_m} = PI_{l,m}\left(P_{wf} + \overline{\gamma}_m \Delta h_{i_m j_m k_m} - P_{R,i_m j_m k_m} - P_{cl,i_m j_m k_m}\right) \quad [3.7]$$

where all the variables were defined in the second section of Chapter 2.

Eq. [3.7] differs from Eq. [2.10] slightly. Summation of Eq. [3.7] over all phases gives:

$$Q_{i_m j_m k_m} = \sum_{l=1}^{n_p} PI_{l,m}\left(P_{wf} + \overline{\gamma}_m \Delta h_{i_m j_m k_m} - P_{R,i_m j_m k_m} - P_{cl,i_m j_m k_m}\right) \quad [3.8]$$

Then the total rate of a well, Q, is the summation of Eq. [3.8] over all wellblocks as

$$Q = \sum_{m=1}^{n_{wb}} \sum_{l=1}^{n_p} PI_{l,m}\left(P_{wf} + \overline{\gamma}_m \Delta h_{i_m j_m k_m} - P_{R,i_m j_m k_m} - P_{cl,i_m j_m k_m}\right) \quad [3.9]$$

Then the wellbore pressure is calculated from Eq. [3.9] as

$$P_{wf} = \frac{Q + \sum_{m=1}^{n_{wb}} \sum_{l=1}^{n_p} PI_{l,m}\left(P_{R,i_m j_m k_m} + P_{cl,i_m j_m k_m} - \overline{\gamma}_m \Delta h_{i_m j_m k_m}\right)}{\sum_{m=1}^{n_{wb}} \sum_{l=1}^{n_p} PI_{l,m}} \quad [3.10]$$

For a total-rate-constraint production well, the well rate term is calculated by substitution of Eq. [3.10] into Eq. [3.8] as

$$Q_{i_m j_m k_m} = \sum_{l=1}^{n_p} PI_{l,m} \left\{ \left[\frac{Q + \sum_{m=1}^{n_{wb}} \sum_{l=1}^{n_p} PI_{l,m} \left(P_{R,i_m j_m k_m} + P_{cl,i_m j_m k_m} - \overline{\gamma}_m \Delta h_{i_m j_m k_m} \right)}{\sum_{m=1}^{n_{wb}} \sum_{l=1}^{n_p} PI_{l,m}} \right] + \overline{\gamma}_m \Delta h_{i_m j_m k_m} - P_{R,i_m j_m k_m} - P_{cl,i_m j_m k_m} \right\} \quad [3.11a]$$

Implicit treatment of Eq. [3.11a] gives:

$$Q^{n+1}_{i_m j_m k_m} = \sum_{l=1}^{n_p} PI^n_{l,m} \left\{ \left[\frac{Q + \sum_{m=1}^{n_{wb}} \sum_{l=1}^{n_p} PI^n_{l,m} \left(P^{n+1}_{R,i_m j_m k_m} + P^n_{cl,i_m j_m k_m} - \overline{\gamma}^n_m \Delta h_{i_m j_m k_m} \right)}{\sum_{m=1}^{n_{wb}} \sum_{l=1}^{n_p} PI^n_{l,m}} \right] + \overline{\gamma}^n_m \Delta h_{i_m j_m k_m} - P^{n+1}_{R,i_m j_m k_m} - P^n_{cl,i_m j_m k_m} \right\} \quad [3.11b]$$

Substitution of Eq. [3.11b] into the discretized form of the pressure equation for the reference phase gives, $P^{n+1}_{R,i_m j_m k_m}$, which can be used to obtain $Q^{n+1}_{i_m j_m k_m}$ using Eq. [3.11b]. The wellbore pressure P^{n+1}_{wf} can be solved using Eq. [3.10]. Eq. [3.7] is used to solve the well rate term of the *l*-th phase, which is required in the mass conservation equation.

For a total-rate-constraint injection well, the total injection rate of the *l*-th phase, Q_l, is specified for each phase. Eq. [3.11] is still used by setting the total well rate to be $Q = \sum_{l=1}^{n_p} Q_l$. Instead of using Eq. [3.7], the well rate term for the *l*-th phase is forced to be:

$$Q_{l,i_m j_m k_m}^{n+1} = \frac{Q_l}{\sum_{l=1}^{n_p} Q_l} Q_{i_m j_m k_m}^{n+1} \qquad [3.12]$$

where $\frac{Q_l}{\sum_{l=1}^{n_p} Q_l}$ is the phase cut specified for the total-rate-constraint injection well.

3.1.3 Implicit Well Rate Allocation Scheme for Fixed Oil Rate

In Chapter 2, we discussed how to treat well rate allocation explicitly for a production well with total oil rate constraint. In this section, we use the implicit method to treat oil-rate-constraint wells.

For a multi-segmented production well, the oil production rate is related to the difference between wellbore pressure and wellblock pressure based on the following equation derived from Darcy's law:

$$Q_{2,i_m j_m k_m} = PI_{2,m}\left(P_{wf} + \overline{\gamma}_m \Delta h_{i_m j_m k_m} - P_{R,i_m j_m k_m} - P_{c2,i_m j_m k_m}\right) \qquad [3.13]$$

Summation of Eq. [3.13] over all well segments gives:

$$Q_2 = \sum_{m=1}^{n_{wb}} PI_{2,m}\left(P_{wf} + \overline{\gamma}_m \Delta h_{i_m j_m k_m} - P_{R,i_m j_m k_m} - P_{c2,i_m j_m k_m}\right) \qquad [3.14]$$

Then the wellbore pressure is calculated from Eq. [3.14] as

$$P_{wf} = \frac{Q_2 + \sum_{m=1}^{n_{wb}} PI_{2,m}\left(P_{R,i_m j_m k_m} + P_{c2,i_m j_m k_m} - \overline{\gamma}_m \Delta h_{i_m j_m k_m}\right)}{\sum_{m=1}^{n_{wb}} PI_{2,m}} \qquad [3.15]$$

Then the well rate term is calculated based on Eq. [3.8] as

$$Q_{i_m j_m k_m} = \sum_{l=1}^{n_p} PI_{l,m}\left[\frac{Q_2 + \sum_{m=1}^{n_{wb}} PI_{2,m}\left(P_{R,i_m j_m k_m} + P_{c2,i_m j_m k_m} - \overline{\gamma}_m \Delta h_{i_m j_m k_m}\right)}{\sum_{m=1}^{n_{wb}} PI_{2,m}} + \overline{\gamma}_m \Delta h_{i_m j_m k_m} - P_{R,i_m j_m k_m} - P_{cl,i_m j_m k_m}\right] \qquad [3.16]$$

Implicit treatment of Eq. [3.11] gives:

$$Q^{n+1}_{i_m j_m k_m} = \sum_{l=1}^{n_p} PI^{n}_{l,m}\left[\frac{Q_2 + \sum_{m=1}^{n_{wb}} PI^{n}_{2,m}\left(P^{n+1}_{R,i_m j_m k_m} + P^{n}_{c2,i_m j_m k_m} - \overline{\gamma}^{n}_m \Delta h_{i_m j_m k_m}\right)}{\sum_{m=1}^{n_{wb}} PI^{n}_{2,m}} + \overline{\gamma}^{n}_m \Delta h_{i_m j_m k_m} - P^{n+1}_{R,i_m j_m k_m} - P^{n}_{cl,i_m j_m k_m}\right] \qquad [3.17]$$

Substitution of Eq. [3.17] into the discretized form of the pressure equation for the water phase gives, $P^{n+1}_{R,i_m j_m k_m}$, which is used to obtain $Q^{n+1}_{i_m j_m k_m}$ using Eq. [3.17]. And the

wellbore pressure P_{wf}^{n+1} can be solved using Eq. [3.15]. Eq. [3.7] is used to solve the well rate term of the *l*-th phase required in the mass conservation equation.

Eq. [3.11b] and Eq. [3.16] are derived based on the IMPEC scheme for UTCHEM. In these Equations, fluid viscosities are taken from previous timestep. However, for non-Newtonian fluids, viscosities are treated as functions of pressure (which relates to flow velocity) and concentrations. To reduce numerical errors in the IMPEC solutions, viscosity values can be iteratively calculated based on updated pressure values. For a fully implicit code, the Newton-Raphson method is required and derivatives of viscosity with respect to pressure and saturation/concentrations need to be calculated tediously.

3.1.3 Verification of the Potential Method

We test the same problem in Section 3.1.1 using the implicit potential method. As shown in Fig. 3.3, the solution from the implicit well rate allocation matches exactly the analytical solution.

Another simulation case was set up using a uniformly heterogeneous horizontal layer-cake model of 4 layers with permeabilities from the top layer to the bottom layer are 1100 md, 100 md, 10 md, and 1 md respectively. Other properties are the same shown in Table 3.1. The solution using a pressure-constraint injection well is considered as the true solution. Fig. 3.4 shows propagation of polymer solution front in different layers. Solutions using the explicit mobility method and the implicit potential method are compared for two values of cross flow: $k_z/k_x = 0.3$ and $k_z/k_x = 0$. As shown in Fig. 3.5, when cross flow is significant, explicit mobility method gives similar results as the implicit potential method. When there is no cross flow, explicit mobility method results in large errors and the implicit potential method is still accurate.

3.2 MODELING AQUIFERS

An aquifer is modeled using either water-saturated gridblocks or constant pressure boundary option (the saturated zone option) in the original UTCHEM. Due to the default no-flow boundary condition in UTCHEM, the former model may underestimate the strength of aquifer influx when there is pressure depletion in the reservoir. In contrast, the latter model neglects the pressure drawdown in the aquifer zone and may overestimate the strength of aquifer influx. There is an increasing interest in applying polymer flooding for improving oil recovery in reservoirs with aquifer. Optimization of polymer flooding design requires a more accurate description of the aquifer strength, which motivated us to implement an aquifer model into UTCHEM.

Commonly used aquifer models include the Carter-Tracy model (Carter and Tracy, 1960), the Fetkovitch model (Fetkovitch, 1971), and the semi-analytical model (Vinsome and Westerveld, 1980) among others. The Carter-Tracy model and the Fetkovitch model were developed to simulate water influxes from a finite aquifer, which requires exact descriptions of the aquifer geometries. However, in field applications, it is very likely that information on aquifer geometry is limited or missing. We chose the semi-analytical model considering its simplicity for implementation and its flexibility for modeling aquifer distribution without the need of exact descriptions of aquifer geometry.

The semi-analytical model assumes a one-dimensional linear pressure diffusivity equation for aquifer influx calculations:

$$\frac{\partial p}{\partial t} = \kappa_p \frac{\partial^2 p}{\partial z^2} \qquad [3.18]$$

where in SI units the pressure p is in Pa, t is in sec, z is in m, and the pressure diffusivity κ_p (in m^2/s) is given as

$$\kappa_p = \frac{k}{c_t \phi \mu} \qquad [3.19a]$$

in which k is the aquifer permeability (in m^2), c_t is the total compressibility (in 1/Pa), and μ is the brine viscosity (in Pa·s). For the English units adopted in UTCHEM, the pressure diffusivity equation, Eq. [3.18] still holds the same form; the pressure p is in psi, t is in day, z is in ft, and the pressure diffusivity κ_p (in ft^2/day) is given as

$$\kappa_p = 6.3283 \frac{k}{c_t \phi \mu} \qquad [3.19b]$$

in which k is in darcy, c_t is in 1/psi, and μ is in cp.

The pressure at the aquifer boundary, or $z = 0$, is assumed to be p_θ. The pressure at the $z = \infty$ is assumed to be constant, p_∞. p_θ and p_∞ are in Pa for SI units, or psi for English units.

An empirical function is chosen for the pressure change profile in an infinite aquifer boundary as

$$\Delta p(t,z) = p(t,z) - p_\infty = \left(p_\theta + az + bz^2 \right) \exp(-z/d) \qquad [3.20]$$

where a (in Pa/m for SI units or psi/ft for English units) and b (in Pa/m^2 for SI units or psi/ft^2 for English units) are fitting parameters and d (in m for SI units or ft for English units) is the diffusion length:

$$d = \frac{\sqrt{\kappa_p t}}{2} \qquad [3.21]$$

At $z = 0$,

$$\left.\frac{\partial p}{\partial t}\right|_{z=0} = \kappa_p \left.\frac{\partial^2 p}{\partial z^2}\right|_{z=0} \qquad [3.22]$$

Substitution of Eq. [3.20] into Eq. [3.22] and using a finite difference discretization gives:

$$\frac{p_\theta - p_\theta^N}{\Delta t} = \kappa_p \left(\frac{p_\theta}{d^2} - \frac{2a}{d} + 2b \right) \qquad [3.23]$$

where the superscript N is the time level. Integrating Equation [3.18] over z gives:

$$\frac{\partial}{\partial t} \int_{z=0}^{z=\infty} p dz = \kappa_p \left.\frac{\partial p}{\partial z}\right|_{z=0}^{z=\infty} \qquad [3.24]$$

Substitution of Eq. [3.20] into Eq. [3.24] and using a finite difference discretization gives:

$$\frac{I - I^N}{\Delta t} = \kappa_p \left(\frac{p_\theta}{d} - a \right) \qquad [3.25]$$

where I (in pa·m for SI units or psi·ft for English units) is defined as

$$I = p_\theta d + a d^2 + 2b d^3 \qquad [3.26]$$

Solving Eq. [3.23] and Eq. [3.25] gives:

$$a = \frac{\frac{\kappa_p \Delta t p_\theta}{d} + I^N - \frac{d^3 (p_\theta - p_\theta^N)}{\kappa_p \Delta t}}{3d^2 + \kappa_p \Delta t} \qquad [3.27]$$

and

$$b = \frac{2ad - p_\theta + d^2 \frac{p_\theta - p_\theta^N}{\kappa_p \Delta t}}{2d^2} \qquad [3.28]$$

where in SI units, a is in pa/m and b is in pa/m^2; in English units, a is in psi/ft and b is in psi/ft^2.

The aquifer influx from an aquifer to the oil reservoir is calculated in SI units as

$$Q_{aquifer} = -\frac{Ak}{\mu} \left. \frac{dp}{dz} \right|_{z=0} = -\frac{Ak}{\mu} \left(\frac{p_\theta}{d} - a \right) \qquad [3.29a]$$

where $Q_{aquifer}$ is in m^3/s, and the interface area between aquifer and reservoir, A, is in m^2. For English units in UTCHEM,

$$Q_{aquifer} = -6.3283 \frac{Ak}{\mu} \left. \frac{dp}{dz} \right|_{z=0} = -6.3283 \frac{Ak}{\mu} \left(\frac{p_\theta}{d} - a \right) \qquad [3.29b]$$

where $Q_{aquifer}$ is in ft^3/day, and the interface area between aquifer and reservoir, A, is in ft^2.

To couple the aquifer model with the reservoir model, we assume the aquifer boundary pressure, p_θ, equals the gridblock pressure to which the aquifer is connected. For UTCHEM which is a block-centered finite difference model, the assumption above may introduce some errors. The aquifer boundary pressure and the aquifer influx terms in the pressure equation are implicitly solved. In addition, the aquifer flux term has been included in the mass conservation equation and the aquifer ion concentrations have also included in the calculations.

The aquifer model was validated against CMG-STARS semi-analytical aquifer model using a 1D aquifer model case. Figs. 3.9 and 3.10 compare the results from UTCHEM and CMG-STARS. The simulation results show a very close match.

3.3 IMPROVED TIMESTEP CONTROL

UTCHEM is an IMPEC-type reservoir simulator whose computational efficiency is restricted by its stability requirement for using small time steps. Overestimated time step may cause nonphysical solutions such as negative concentrations or saturations while underestimated time step may lead to prohibitive time cost. An optimum time step selector is important for speeding up the simulation and also improving its stability.

In UTCHEM, the maximum and minimum time steps can be specified in the input file. Another option is to use the Courant number, C_N, defined as

$$C_N = \underset{All\ wells}{Max}\left[\underset{m=1}{\overset{n_{wb}}{Max}}\left(\frac{Q_{i_m j_m k_m}\Delta t}{V_b \phi}\right)\right] \qquad [3.18]$$

where V_b is the wellblock bulk volume. In the calculations, C_N is limited between [$C_N min$, $C_N max$]. $C_N min$ and $C_N max$ are input parameters. Typically, $C_N min$ =0.04 and $C_N max$ =0.4. Then respectively the minimum time step and the maximum time step are:

$$\Delta t_{\min} = \frac{C_{N\min}}{\underset{All\ wells}{Max}\left[\underset{m=1}{\overset{n_{wb}}{Max}}\left(\frac{Q_{i_m j_m k_m}}{V_b \phi}\right)\right]} \qquad [3.19]$$

and

$$\Delta t_{\max} = \frac{C_{N\max}}{\underset{All\ wells}{Max}\left[\underset{m=1}{\overset{n_{wb}}{Max}}\left(\frac{Q_{i_m j_m k_m}}{V_b \phi}\right)\right]} \qquad [3.20]$$

In simulations of chemical flooding processes involving polymer or surfactant, some pores may not be accessible to the polymer or surfactant molecules, and this is modeled using a decreased effective porosity, ϕ_e. When the same time step constraints are used, simulation of polymer/surfactant flooding process may become unstable for small effective porosity, ϕ_e. Take a one-dimensional polymer coreflood simulation for example. The core and fluid properties are given in Table 3.2. The effective porosity is considered as a variable. As shown in Fig. 3.6, produced polymer concentration is plotted against injected pore volume for different effective pore volume values. When the effective pore volume is reduced to 0.75, the simulated polymer concentration becomes unstable. To avoid such problem, Eq. [3.18], Eq. [3.19] and Eq. [20] are modified to include the effect of inaccessible pore volume. The definition of courant number then becomes:

$$C_N = \max_{All\ wells}\left[\max_{m=1}^{n_{wb}}\left(\frac{Q_{i_m j_m k_m}\Delta t}{V_b \phi \phi_e}\right)\right] \qquad [3.21]$$

Similar treatments apply to Eq. [3.19] and Eq. [3.20]. After modification, the simulation results are shown in Fig. 3.7. Simulation results are all stable and consistent.

In UTCHEM, the automatic time step selection methods are based on the method of relative changes (Bailey, 1969):

$$\Delta t^{n+1} = \Delta t^n \min_{\kappa=1}^{n_c^*} \left[\frac{\Delta C^*_{\mathrm{lim},\kappa}}{\max_{i=1}^{n_{bl}} \left| \Delta C^*_{i,\kappa} \right|} \right] \qquad [3.22]$$

where n_c^* refers to the first three components: water, oil, and surfactant, $\Delta C^*_{\mathrm{lim},\kappa}$ is an input parameter and the same for all three components (IMES = 2). $\Delta C^*_{i,\kappa}$ is the change in total concentration of the component κ; n_c^* refers to all the components, $\Delta C^*_{\mathrm{lim},\kappa}$ are input parameters and can be different for each component (IMES = 3). $\Delta C^*_{i,\kappa}$ is the change in total concentration of the component κ, n_c^* refers to all the components, $\Delta C^*_{\mathrm{lim},\kappa}$ are input parameters and can be different for each component (IMES = 4), and $\Delta C^*_{i,\kappa}$ is the relative change in total concentration of the component κ, or $\frac{\Delta C_{i,k}}{C_{i,k}}$.

To improve the performance of the relative change method, a modified method is adopted in UTCHEM by introducing a relaxation parameter, ω:

$$\Delta t^{n+1} = \Delta t^n \min_{\kappa=1}^{n_c^*} \left[\frac{(1+\omega)\,\Delta C^*_{\mathrm{lim},\kappa}}{\max_{i=1}^{n_{bl}} \left| \Delta C^*_{i,\kappa} \right| + \omega \Delta C^*_{\mathrm{lim},\kappa}} \right] \qquad [3.23]$$

where ω is an empirical parameter as assumed to be 0.75 such that the subsequent time step does not exceed a value of (1+0.75)/0.75 times the previous time step. The value of

0.75 was selected following the timestep size treatment in CMG-STARS. This modification was proposed by Grabowski *et al*. (1979) and is expected to perform more efficiently "where the nature of the equations changes rapidly" (Mehra *et al*., 1982).

3.4 INACTIVE CELL TREATMENT

Inactive or keyout cells are gridblocks which have zero permeability in the *x*, *y* and *z* directions or zero transmissibility coefficients between their neighboring gridblocks. Two sources contribute to the existence of inactive cells in a reservoir model. Firstly, inactive cells may result from representing an actual reservoir of irregular boundaries with a numerical model of regular shapes, e.g., a rectangular box model in a Cartesian system. Thus the no flow boundary condition is modeled with inactive cells which are impermeable to flow and dispersion. Secondly, reservoir blocks of very low permeability or porosity are treated as inactive cells to avoid numerical errors.

Originally in UTCHEM, all cells of permeability less than or equal to 10^{-5} md or porosity less than or equal to 0.01 were treated as inactive cells. Then the permeability in the *x* and *y* directions were set to 10^{-5} md and porosity of 0.01 with water saturation was of 1. All these cells were still included in all the calculations of mass conservation equations, the pressure equation, and other petrophysical models. Inclusion of these inactive cells in the pressure equation may cause ill-conditioned matrices when solving linear systems of equations and sometimes causes solvers to crash. Besides, numerical errors are induced during solving the mass conservation equations or other physical property models.

To skip inactive cells in reservoir simulation not only reduces redundant calculations when a significant portion of cells are inactive, but also improves the stability and accuracy of the simulation. To remove inactive cells in UTCHEM

simulation, a flag array called ACTNUM was introduced. When the cell is considered as active, the ACTNUM value of the cell is set to be 1. For inactive cells, it is set to be 0. This ACTNUM array is used to skip inactive cells in all of the cell-based calculations in UTCHEM. Besides, the transmissibility coefficients of the inactive cells are set to be zero. In the pressure equation, the inactive cells are specially handled. Their pressures are kept as the initial reservoir pressures which are constant and not affected by active cells. For well index calculation, perforations in the zone of inactive cells are skipped. Besides, the default cut-off criterion for inactive cells ($k_x, k_y \le 10^{-5}$ md, or $\phi \le 0.01$) is now adjustable in the INPUT file for users who study chemical EOR in "unconventional resources".

Ideally, removal of inactive cells caused by irregular boundaries from the pressure matrix would speed up the simulation. This can be achieved by using a variable band-width solver (Abou-Kassem and Ertekin, 1992) or an unstructured reservoir simulator (Karpinski *et al*, 2009), which requires more programming efforts than our current work and is an important research area for reservoir simulation.

3.5 SOLVERS FOR LINEAR SYSTEMS OF EQUATIONS

The discretized form of pressure equation for all n_{bl} gridblocks is a set of linear systems of equations:

$$Ax = b \qquad [3.24]$$

where A is the coefficient matrix ($n_{bl} \times n_{bl}$) or the transmissibility matrix, b is the right-hand-side vector ($n_{bl} \times 1$) or the forcing function vector (source terms and pressure at

previous time step), and x is the vector of unknowns ($n_{bl} \times 1$) or the pressure at current time step.

In UTCHEM, the default solver for linear systems of equations is the Jacobi Conjugate Gradient (JCG) method (Saad, 2003), which is referred as the solver option of ISOVER = 0. The iterative method is designed for diagonally dominant, positive-definite coefficient matrix and stores only the upper or lower triangle matrix elements. It is proven to be highly efficient for most cases with well-conditioned coefficient matrices. However, simulation of large-size problem with high heterogeneity and many inactive cells may cause the coefficient matrix to become ill-conditioned. Besides, implicit treatment of the constant oil rate option for a production well makes the coefficient matrix non-symmetric. JCG may fail to converge or crash for ill-conditioned coefficient matrices and doesn't apply to non-symmetric coefficient matrices. In order to solve these two problems, other solvers need to be investigated.

The first option is to use the direct solver for sparse matrices in the package of Parallel Sparse Direct Solver (PARDISO) (Schenk *et al.*, 2001). PARDISO is regarded as one of the most popular direct solver since its release. Currently it is under development by both PARDISO-Project group (Schenk et al., 2014) and Intel's Math Kernel Library research group (Intel™, 2014). This solver can deal with non-symmetric matrix and is robust for ill-conditioned problems. Besides, it is memory efficient and automatically parallel. Therefore, PARDISO is sometimes even faster than some direct solvers. It is currently implemented as the solver option of ISOLVER = 1 in UTCHEM.

Although direct solvers are robust, they are not as efficient as iterative solvers when dealing with large-size problems. To avoid this problem, we implemented another option in UTCHEM as ISOLVER = 2, which is the iterative solver named the Generalized Minimal Residual (GMRES) algorithm. GMRES is a popular solver of

excellent stability and accuracy and approximates the solution by the vector in a Krylov subspace with minimum residual. The version of source code we adopted in UTCHEM is the MGMRES (the restarted GMRES) code by Ju and Burkardt (2012), which uses the incomplete LU decomposition for preconditioning. GMRES is robust and can handle non-symmetric matrices. However, it needs to store both the upper and lower triangle matrix elements. Thus it requires more space for storage than the Jacobi Conjugate Gradient method.

3.5.1 Simulation Studies

To compare the performance of different solvers, several simulation cases were set up and tested. All of the tests were performed under the UT-Austin PGE-Petros cluster (Linux OS) using a node. Each node has 16 GB of memories and 4 CPG cores with frequency of 2.73 GHz. And the tests were based on UTCHEM_2014 version in which the performance of JCG in heterogeneous problems has been improved by skipping inactive cell calculations in solving pressure equations.

The first simulation case is a surfactant/polymer flood case in a quarter of a 5-spot pattern as shown in Fig. 3.11. Reservoir model description is given in Table 3.3. The simulation results from the three solvers matched very well with each other. The overall CPU times and the CPU times by solving the pressure equations using the solvers are compared in Fig. 3.12. It shows that for this case, JCG is the fastest and the percentages of the CPU times by solver in overall CPU times are relatively small.

The second simulation case is a polymer flood case in a heterogeneous reservoir as shown in Fig. 3.13. Reservoir model description is given in Table 3.4. Before skipping inactive cells in solving pressure equation using JCG, JCG was not able to converge well which brought numerical errors. After skipping inactive cells, the simulation results from

the three solvers matched very well with each other. The overall CPU times and the CPU times by solving the pressure equations using the solvers are compared in Fig. 3.14. It shows that for this case, JCG is still the fastest and the CPU times for solving pressure equation by GMRES or PARDISO are about 3 times of the CPU time by JCG.

The third simulation case is a water flood case in a heterogeneous reservoir as shown in Fig. 3.15. Reservoir model description is given in Table 3.5. Even after skipping inactive cells in solving pressure equation, JCG is not able to converge while the simulation results from the other two solvers matched very well with each other. The overall CPU times and the CPU times by solving the pressure equations using the solvers are compared in Fig. 3.16. It shows that for this case, for this small-size problem, PARDISO is about 3 times faster than GMRES.

5 more simulation cases were tested. All of the test results are summarized in Table 3.6. In all cases that JCG didn't fail, the simulation results from the three solvers matched very well with each other.

3.5.2 Conclusions and Recommendations

Based on the simulation test results from JCG, PARDISO and GMRES, we made the follow conclusions:

- In terms of computational efficiency, JCG is the fastest in most situations when it converges and runs successfully. JCG is about 1-3 times faster than GMRES and is about 2-12 times faster than PARDISO. This is because JCG is intrinsically designed for symmetrical matrices while PARDISO or GMRES is intrinsically designed for non-symmetric matrices.
- In terms of robustness, PARDISO and GMRES are both stable and worked for every tested case. However, JCG is not as stable as PARDISO or GMRES. It may

fail to converge which leads to inaccurate simulation results or even crash directly for some cases.

- In terms of applicability, PARDISO and GMRES can both be applied to non-symmetric matrices while JCG can only be applied to symmetric matrices.

Considering the computational efficiency, robustness and applicability, recommendations are given as follows:

- For a model that is relatively homogeneous and simple and uses no implicit treatment of the constant oil rate, JCG is recommended for its computational efficiency.
- For a model that is heterogeneous with many inactive cells or inactive layers, GMRES is recommended for its computational efficiency and robustness.
- For users using a powerful machine that has many cores, PARDISO is recommended due to its capability of automatic parallelization.

Length, L, ft	7.8
Width, W, ft	0.04
Upper layer thickness, h_1, ft	0.19029
Lower layer thickness, h_2, ft	0.19029
Upper layer porosity, ϕ_1	0.38
Lower layer porosity, ϕ_2	0.38
Upper layer permeability, k_1, md	11000
Lower layer permeability, k_2, md	1000
Total Injection Rate, ft^3/D	0.16951
Displaced fluid viscosity (Brine), cp	1
Displacing fluid viscosity (Polymer), cp	5
Polymer Concentration	0.1 wt%
Polymer model input parameters	
Visc. vs. conc. : AP1, AP2, AP3	40, 0, 0
Shear Rate: GAMMAC, GAMHF, POWN, GAMHF2	0, 35, 1, 0

Table 3.1: Reservoir and fluid properties for 2D cross-sectional model.

Length, L, ft	0.744
Cross area, A, ft^2	0.0121
Porosity	0.219
Permeability, md	72
Initial water saturation, S_{wi}	0.59
End-point water/oil relative permeability	0.3, 0.6
Corey exponents for water/oil	2, 2
Residual water/oil saturations	0.3, 0.33
Oil viscosity, cp	7
Brine viscosity, cp	0.678
Total injection rate, ft^3/D	0.0123
Polymer concentration	0.15 wt%
Polymer model input parameters	
Viscosity. vs. conc.: AP1, AP2, AP3	12.54, 41, 715
Shear rate: GAMMAC, GAMHF, POWN, GAMHF2	130, 450, 1.8, 0
Perm. reduction: BRK, CRK, RKCUT	100, 0.13, 10
Adsorption: AD41, AD42, B4D	0.97, 0.5, 100
Effective PV: EPHI4	Variable

Table 3.2: Core and fluid properties for 1D polymer flooding model.

Reservoir model description	values
Dimension, ft	250×250×10
Number of grid blocks	11×11×2
Permeability, md	Variable
Porosity	0.2
Injection time, days	1500

Table 3.3: Reservoir model description for solver test case 1.

Reservoir model description	values
Dimension, ft	566.5×1323×622.4
Number of grid blocks	7×18×89
Permeability, md	Variable
Porosity	0.2
Injection time, PV	1.5

Table 3.4: Reservoir model description for solver test case 2.

Reservoir model description	values
Dimension, ft	3100×4500×24
Number of grid blocks	45×31×3
Permeability, md	Variable
Porosity	0.139
Injection time, days	2550

Table 3.5: Reservoir model description for solver test case 3.

Case #	Process	# of Cells	Brief Description	CPU Time (JCG/GMRES/PARDISO)
1	SP	11×11×2	Simple 5-spot	0.7 sec/ 2 sec/ 3.3sec
2	P	7×18×89	Heterogeneous	0.68 h/ 2.04 h/ 2.11 h
3	W	45×31×3	Layered	Fail/ 2011 sec/ 668 sec
4	P	50×1×4	Implicit well	3.5 sec/1.8 sec/7.9 sec
5	ASP	15×15×36	Heterogeneous	0.53 h/ 1.55 h/ 6.25 h
6	ACP	37×42×5	Corner inactive cells	0.49 h/ 2.03 h/ 1.34 h
7	W	22×40×22	Boundary inactive cells	414 sec/ 525 sec/ 1972 sec
8	P	58×47×36	Boundary inactive cells, deviated wells	Fail/ 31.4 h/ 65.2 h

Table 3.6: Summary of solver performance results in 8 simulation tests.

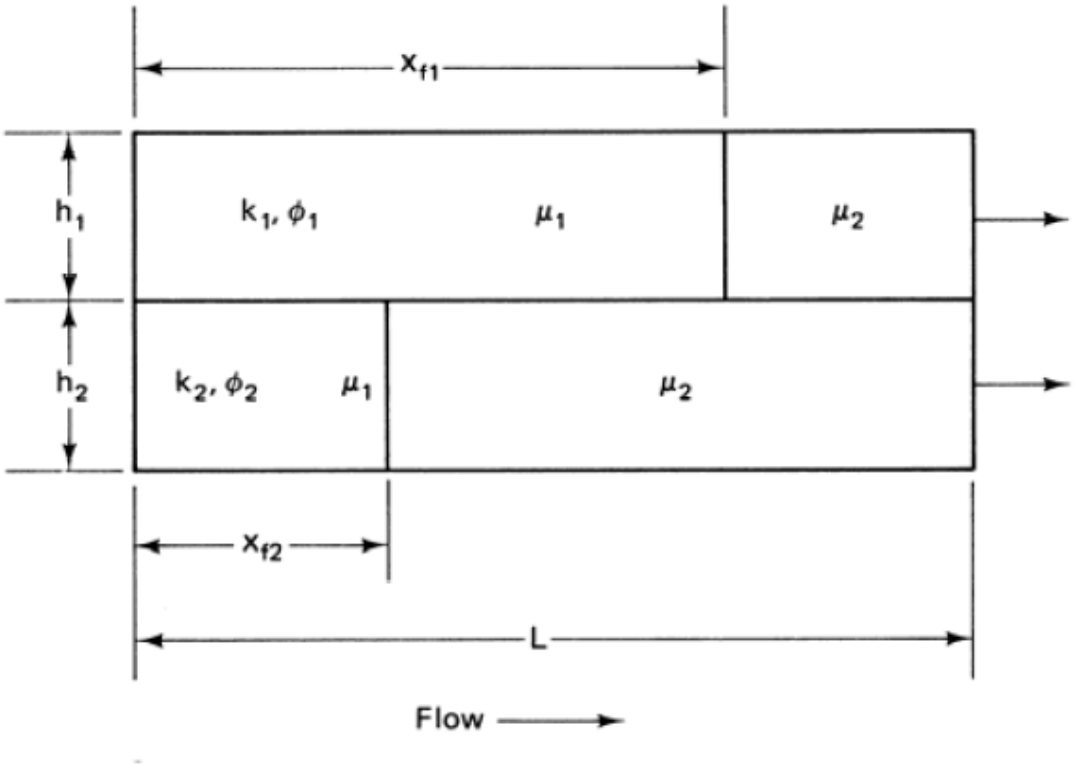

Figure 3.1: Polymer flooding of a heterogeneous reservoir of two layers (From Lake, *Enhanced Oil Recovery*, Chapter 6, Figs. 6-9).

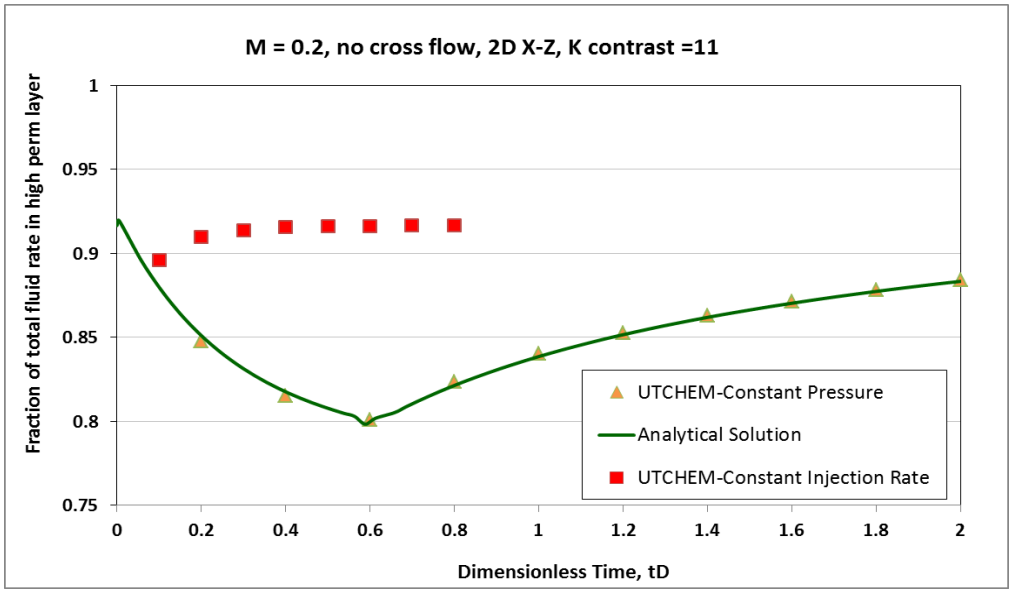

Figure 3.2: Fraction of total fluid rate in high perm layer vs. dimensionless time.

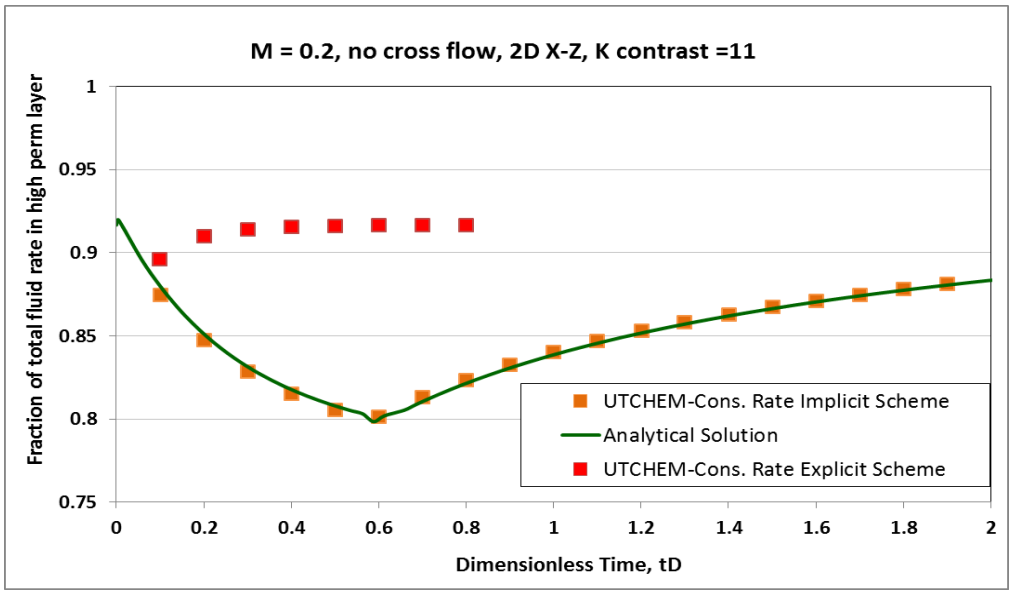

Figure 3.3: Fraction of total fluid rate in high perm layer vs. dimensionless time.

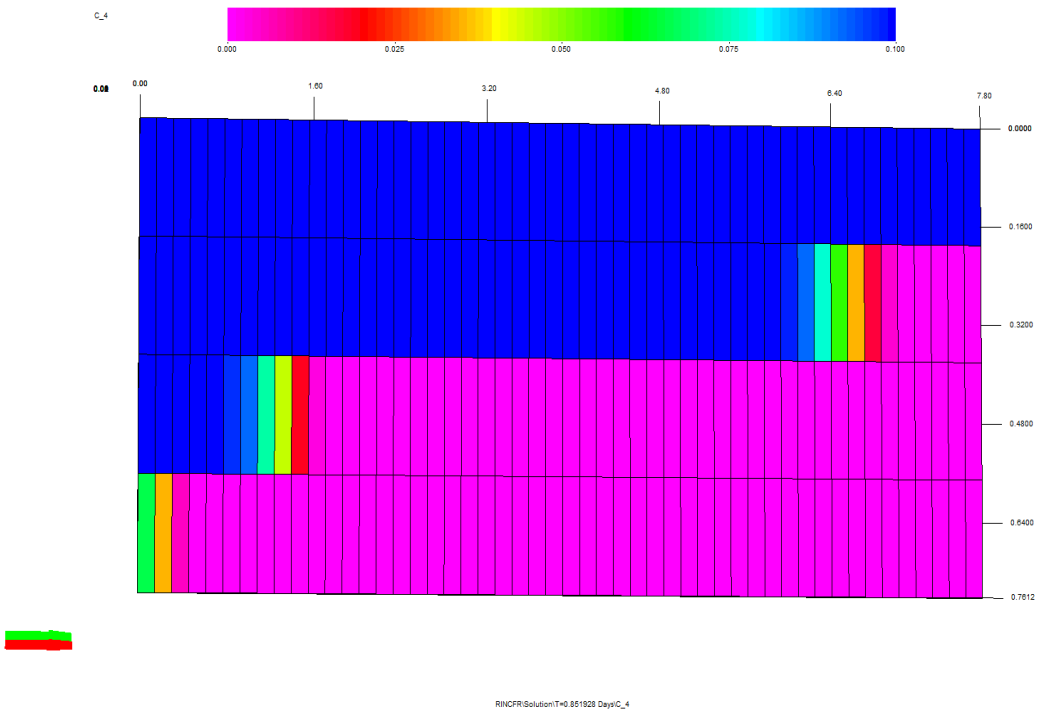

Figure 3.4: Propagation of polymer solution fronts in different layers.

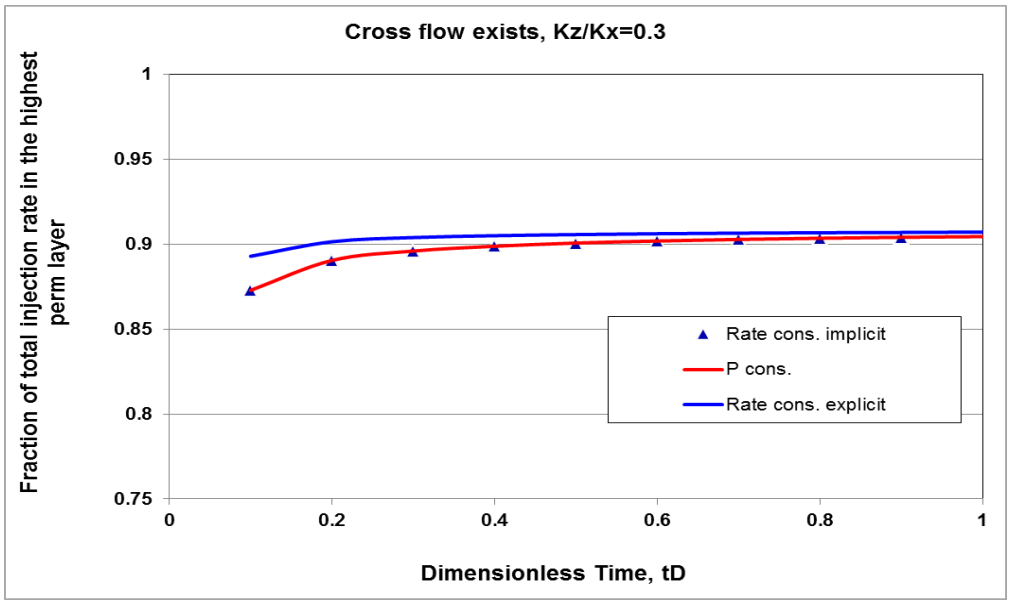

Figure 3.5: Fraction of total fluid rate in the highest perm layer vs. dimensionless time.

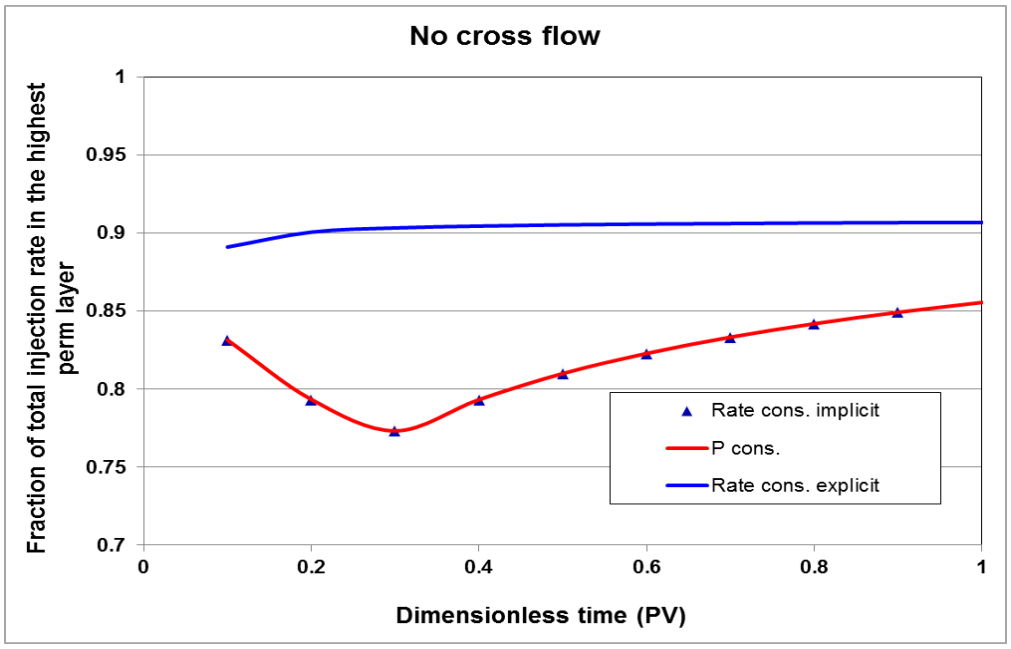

Figure 3.6: Fraction of total fluid rate in the highest permeability layer vs. dimensionless time.

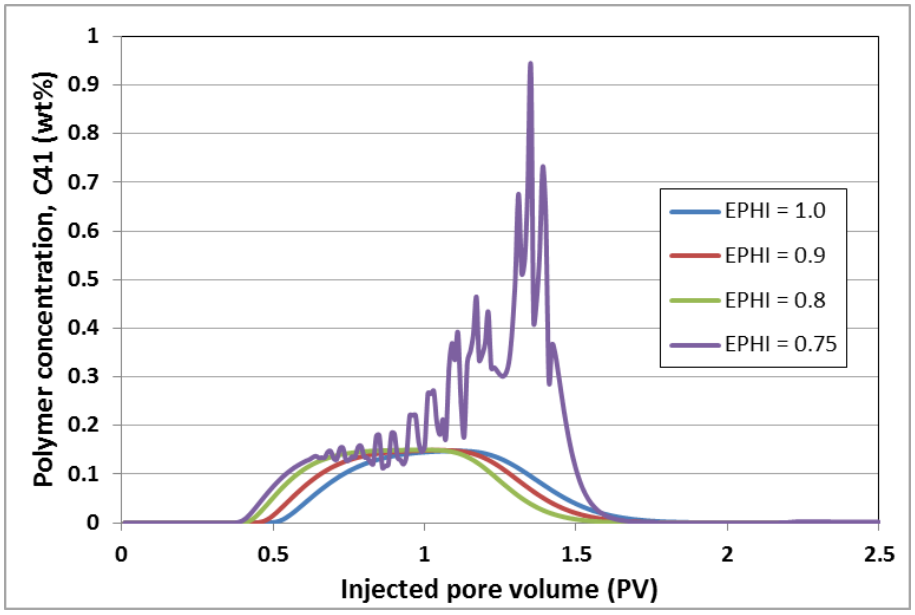

Figure 3.7: Produced polymer concentration vs. injected pore volume for different effective pore volume values.

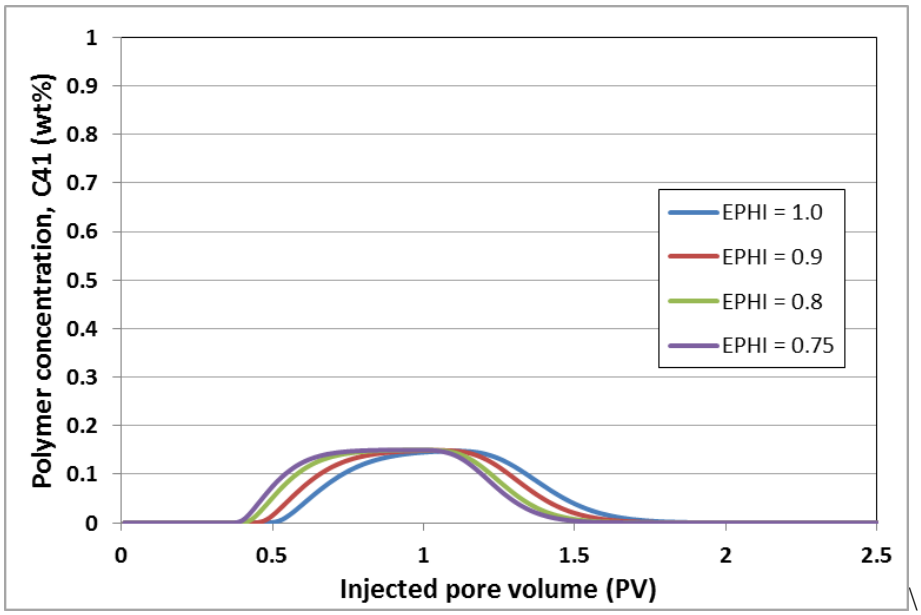

Figure 3.8: Produced polymer concentration vs. injected pore volume for different effective pore volume values using modified courant number.

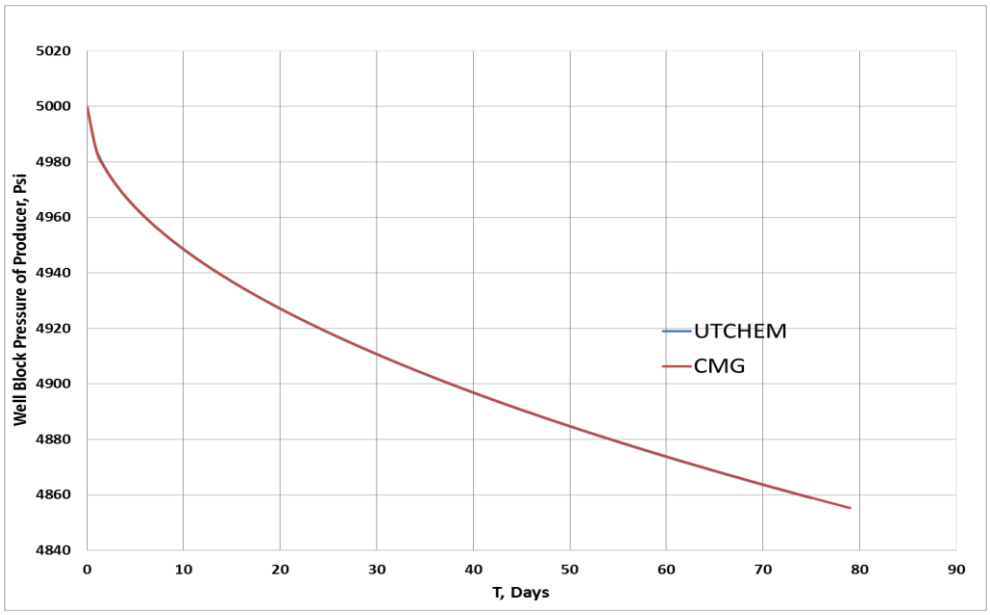

Figure 3.9: Comparison of the producer wellblock pressure between UTCHEM and CMG-STARS for 1D aquifer model.

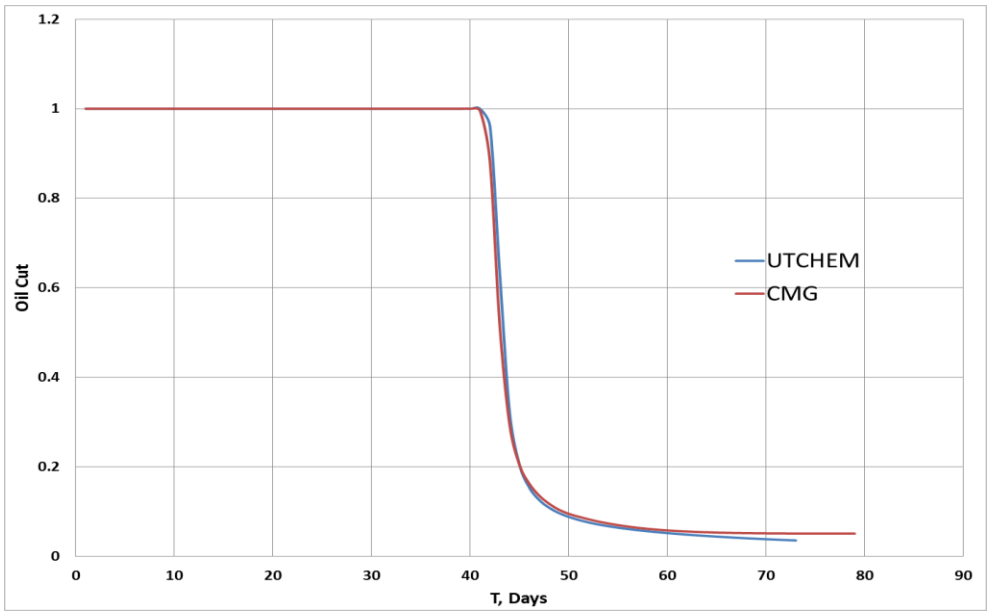

Figure 3.10: Comparison of oil cut between UTCHEM and CMG-STARS for 1D aquifer model.

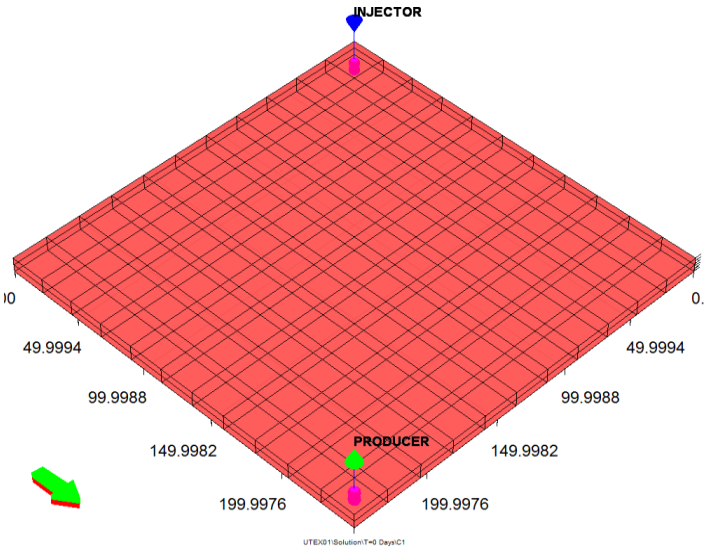

Figure 3.11: Well configuration in the reservoir model of solver test case 1.

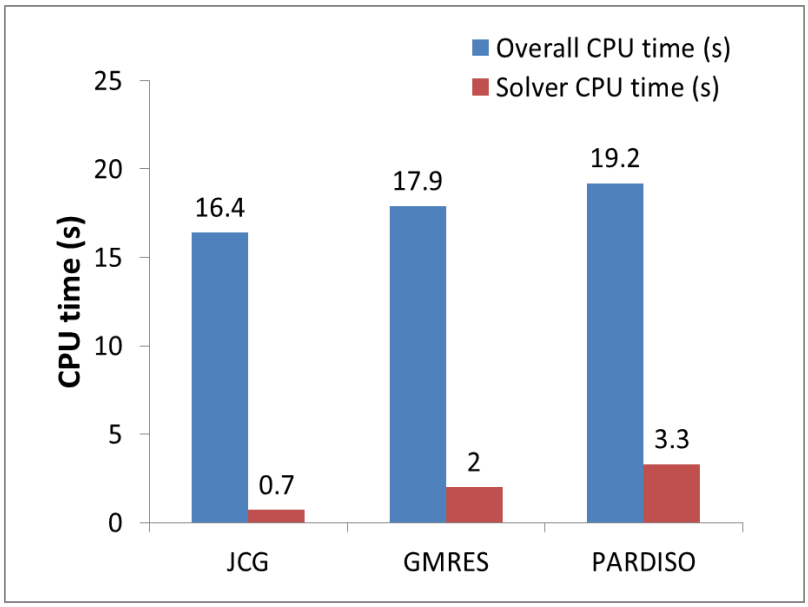

Figure 3.12: Comparison of CPU times for solver test case 1.

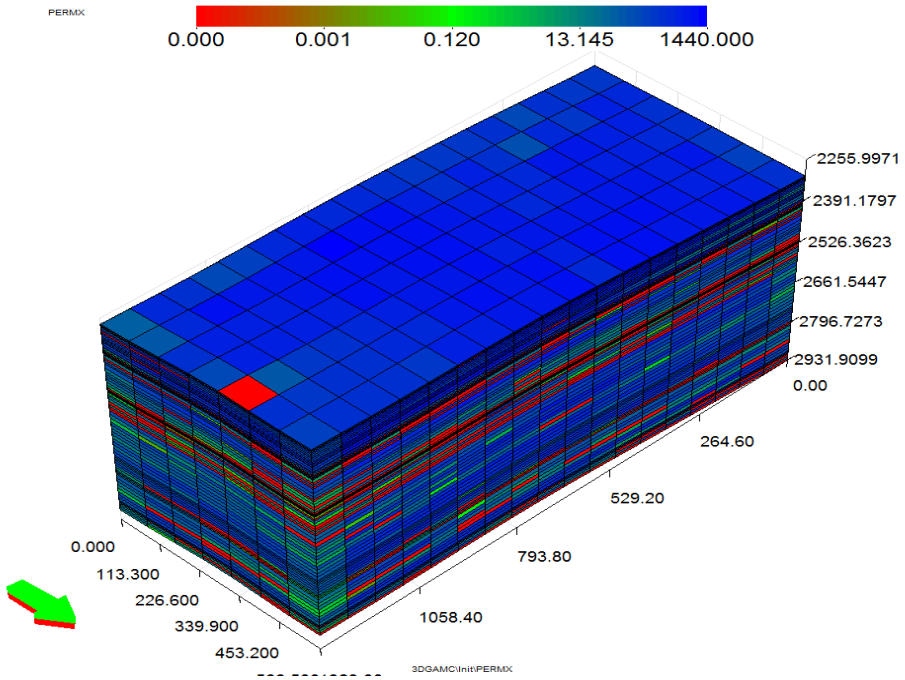

Figure 3.13: Permeability distribution in the reservoir model of solver test case 2.

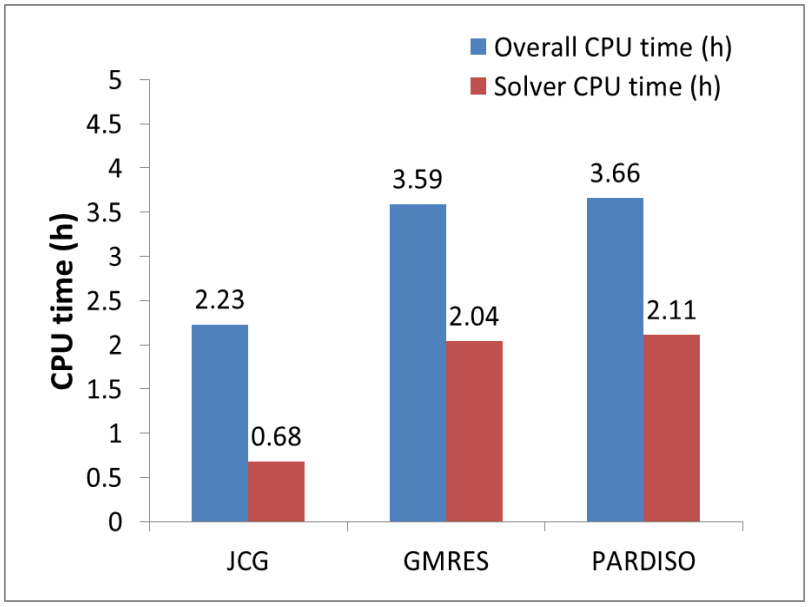

Figure 3.14: Comparison of CPU times for solver test case 2.

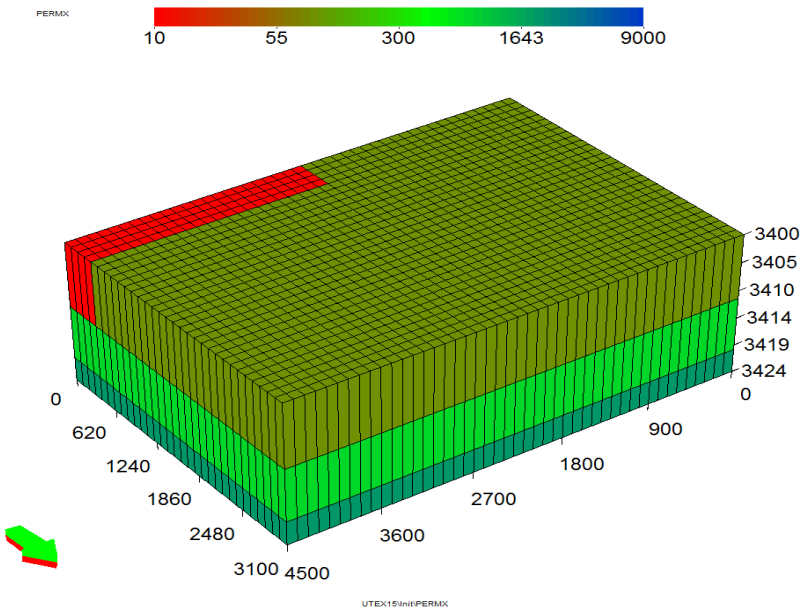

Figure 3.15: Permeability distribution in the reservoir model of solver test case 3.

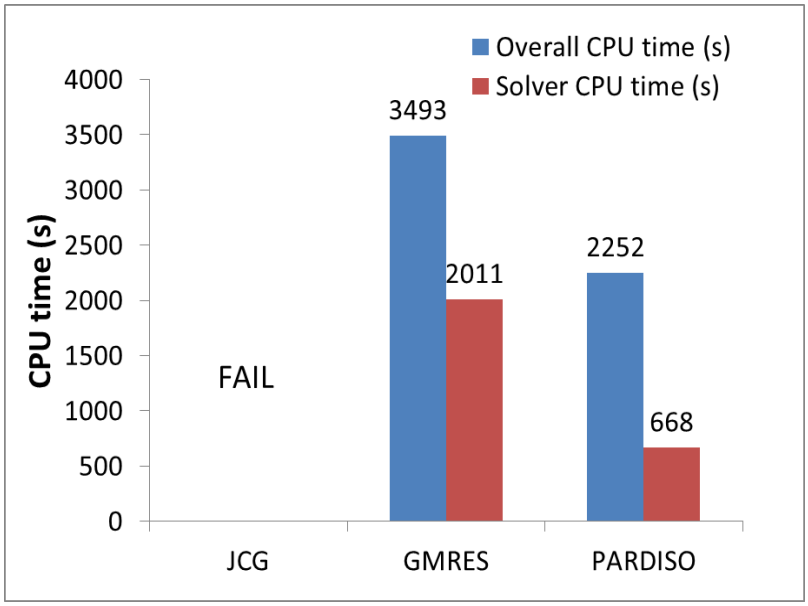

Figure 3.16: Comparison of CPU times for solver test case 3.

Chapter 4: Accurate Modeling of Polymer Injectivity[2]

In conventional reservoir simulations, analytical well models relate wellblock pressure, wellbore pressure and geometric factors such as wellbore radius and grid size. A basic assumption for these models is that fluid viscosity is Newtonian. Using these well models for simulating injection of non-Newtonian polymer solutions often predict unrealistic well injectivity. Apparent viscosity of polymer solution is a complicated function of fluid velocity, polymer properties, permeability, porosity, etc. As the distance from an injection well increases, fluid velocity decreases; meanwhile, apparent polymer viscosity changes drastically. For coarse-grid simulations, the average well block fluid velocity may be several orders of magnitude smaller than fluid velocity near wellbore. Very fine grids can be used to improve the simulation results at the cost of computational time. This "grid effect" was discussed in Chapter 2 and is an important concern in simulating chemical flooding processes using polymer for mobility control.

In order to eliminate the grid effect on fluid velocity and the subsequent viscosity calculations, a semi-analytical injectivity model for non-Newtonian polymer solutions was proposed and implemented in UTCHEM. Both shear-thinning and shear-thickening rheologies are considered.

4.1 Semi-Analytical Polymer Injectivity Model

In this section, we describe a methodology to extend Peaceman's well model (Peaceman, 1983) to non-Newtonian polymer solutions.

[2] Li, Z., and Delshad, M., "Development of an Analytical Injectivity Model for Non-Newtonian Polymer Solutions", SPE 163672, SPE Journal, 19(03): 24-585, 2014. In this work, Li developed the semi-analytical injectivity model and conducted simulation studies. Delshad gave suggestions and made revisions.

4.1.1 Development of a Semi-Analytical Injectivity Model

Peaceman (1983) developed a general well model for reservoir simulation accounting for the effects of nonsquare grids and anisotropic permeability. If we follow Peaceman's derivations, the *x*-*y* coordinates are converted to

$$\begin{cases} u = (k_y/k_x)^{1/4} x \\ v = (k_x/k_y)^{1/4} y \end{cases} \quad [4.1]$$

The basic assumption for deriving a closed-form semi-analytical polymer injectivity model is that in the *u*-*v* plane, the critical region involved in strong near-wellbore effects that affect pressure change is the annular area between the two radii:

$$\bar{r}_w = 0.5\left[(k_y/k_x)^{1/4} + (k_x/k_y)^{1/4}\right] r_w \quad [4.2]$$

and

$$r_o^{uv} = 0.14\left[(k_y/k_x)^{1/2}\Delta x^2 + (k_x/k_y)^{1/2}\Delta y^2\right]^{1/2} \quad [4.3]$$

where Δx and Δy are the grid sizes in the x and y directions, k_x and k_y are the permeabilities in the x and y directions, r_w is the wellbore radius, $\bar{r}_w$ is the Peaceman's well radius in the *u*-*v* plane, and r_o^{uv} is the Peaceman's equivalent radius in the *u*-*v* plane. The critical region of Peaceman's well model is shown in Fig. 4.1. We assume that for both Newtonian flow and non-Newtonian flow, the r_o^{uv} represents "the radius of an almost circular isobar in the *u*-*v* plane that has the same pressure as the well block" (Peaceman, 1983). Other assumptions for the critical region include:

1. Related reservoir properties such as permeability, porosity, etc. are homogeneous;
2. Fluid and rock compressibilities are negligible;
3. Radial flow dominates the critical region;
4. Polymer is in the aqueous phase only;
5. The wellblock is fully penetrated.

To study anisotropic permeability, Peaceman (1983) used a conformal mapping to the *u*-*v* coordinates into an elliptic coordinate system ($\rho-\theta$) as

$$\begin{cases} u = b\cosh\rho\cos\theta \\ v = b\sinh\rho\sin\theta \end{cases} \qquad [4.3]$$

where $b^2 = r_w^2(k_y - k_x)/(k_y k_x)^{1/2}$ assuming $k_x < k_y$. If $k_x > k_y$, we can just interchange *x* and *y*. Using the derivations by Peaceman (1983), one obtains the Darcy's law in the form of

$$q_1 = -\frac{2\pi h k_{r1}(k_x k_y)^{1/2}}{\mu_1}\frac{dP_1}{d\rho} \qquad [4.4]$$

where *h* is the reservoir depth. Peaceman also defined a mean radius as

$$\bar{r} = (b\sinh\rho + b\cosh\rho)/2 = \frac{b}{2}\exp(\rho) \qquad [4.5]$$

Using Eqs. [4.4] and Eqs. [4.5], it is observed that

$$dP_1 = -\left[\frac{q_1}{2\pi h(k_x k_y)^{1/2} k_{r1}}\right]\mu_1 \frac{d\bar{r}}{\bar{r}} \qquad [4.6]$$

For flow of a polymer solution through porous media,

$$\mu_1 = \mu_{app}(\dot{\gamma}_{eq}) \qquad [4.7]$$

where

$$\dot{\gamma}_{eq} = \frac{\gamma_c |\vec{u}_1|}{\sqrt{\bar{k}k_{r1}\phi S_1}} = \frac{\gamma_c}{\sqrt{\bar{k}k_{r1}\phi S_1}} \frac{q_1}{2\pi h\bar{r}} \qquad [4.8]$$

which is a short form for Eq. [2.51]. Instead of calculating the average permeability $\bar{k}$ using Eq. [2.53], for the critical region which the radial flow pattern dominates, we assume:

$$\bar{k} = \sqrt{k_x k_y} \qquad [4.9]$$

In Peaceman's well model (Peaceman, 1983), it is found that

$$P_1(\bar{r} = r_o^{uv}) = P_o \qquad [4.10]$$

where P_o is the well block pressure. Eq. [4.10] is taken to be valid for non-Newtonian fluids based on the assumption we made earlier.

Substitution of Eqs. [4.7] through Eq. [4.10] into Eq. [4.6] and integrating Eq. [4.6] from $\bar{r}_w$ and r_o^{uv} gives:

$$P_{wf} - P_o = \left[\frac{q_1}{2\pi h (k_x k_y)^{1/2} k_{r1}} \right] \bar{\mu}_1 \ln \frac{r_o^{uv}}{\bar{r}_1} \qquad [4.11]$$

where the average apparent viscosity $\bar{\mu}_1$ is:

$$\bar{\mu}_1 = \frac{\int_{\bar{r}=\bar{r}_w}^{\bar{r}=r_o^{uv}} \mu_{app}(\bar{r}) \frac{d\bar{r}}{\bar{r}}}{\ln \frac{r_o^{uv}}{\bar{r}_w}} \qquad [4.12]$$

All of the derivations up to now apply to a general polymer rheology and can be easily extended to many rheological models of non-Newtonian fluids (e.g., Bird *et al*., 2007; Stavland *et al*., 2010).

Application of Meter's equation (Eq. [2.54]) in Eq. [4.12] gives:

$$\bar{\mu}_1 = \mu_\infty + \frac{\mu_p^0 - \mu_\infty}{P_\alpha - 1} \frac{\ln \left(\frac{\left(r_o^{uv}\right)^{P_\alpha - 1} + R_p^{P_\alpha - 1}}{\bar{r}_w^{P_\alpha - 1} + R_p^{P_\alpha - 1}} \right)}{\ln \frac{r_o^{uv}}{\bar{r}_w}} \qquad [4.13]$$

where

$$R_p = \frac{q_1 \gamma_c}{2\pi h \dot{\gamma}_{\frac{1}{2}} \sqrt{\bar{k} k_{r1} \phi S_1}} \qquad [4.14]$$

The physical meaning of R_p is that for a radial flow, at $\bar{r} = R_p$, the equivalent shear rate becomes $\dot{\gamma}_{\frac{1}{2}}$, the shear rate at which apparent viscosity is $\frac{\mu_\infty + \mu_p^0}{2}$. If a fine-grid simulation is used to capture polymer injectivity and $\bar{r}_w < R_p$, the grid size should be much smaller than $2R_p$. When $R_p \ll \bar{r}_w$, the polymer rheology will have little impact on polymer injectivity and no grid refinement is needed. As injection rate increases, R_p increases, and $\bar{\mu}_1$ approaches μ_∞; as injection rate decreases, R_p decreases, and $\bar{\mu}_1$ approaches μ_p^0.

Application of the Unified Viscosity Model (Eq. [2.56]) in Eq. [4.12] gives:

$$\bar{\mu}_1 = \frac{\int_{\bar{r}=\bar{r}_w}^{\bar{r}=r_o^{uv}} \left\{ \mu_\infty + (\mu_p^0 - \mu_\infty)\left[1+(\frac{R_{pc}}{\bar{r}})^2\right]^{(n_1-1)/2} + \mu_{\max}\left\{1-\exp\left[-\left(\frac{R_{pv}}{\bar{r}}\right)^{n_2-1}\right]\right\}\right\} \frac{d\bar{r}}{\bar{r}}}{\ln \frac{r_o^{uv}}{\bar{r}_w}} \quad \text{……} \quad [4.15]$$

where

$$\begin{cases} R_{pc} = \dfrac{\lambda_1 q_1 \gamma_c}{2\pi h \sqrt{\bar{k}k_{r1}\phi S_1}} \\ R_{pv} = \dfrac{\lambda_2 \tau q_1 \gamma_c}{2\pi h \sqrt{\bar{k}k_{r1}\phi S_1}} \end{cases} \quad [4.16]$$

where R_{pc} and R_{pv} can be used to estimate the grid size for fine-grid simulations. Besides, as injection rate increases, R_{pc} and R_{pv} increase, and the shear-thinning part of $\bar{\mu}_1$ approaches μ_∞ while the shear-thickening part of $\bar{\mu}_1$ approaches $\mu_{\max}$; as injection

rate decreases, R_{pc} and R_{pv} decrease, and the shear-thinning part of $\bar{\mu}_1$ approaches μ_p^0 while the shear-thickening part of $\bar{\mu}_1$ approaches zero. Eq. [4.15] can be calculated using numerical integration.

All of the derivations above are for a single layer reservoir in an *x*-*y* plane with the well orientated in the *z*-direction. Generally, *x, y* and *z* are interchangeable. So our model is applicable to 3D reservoir simulations.

4.1.2 Application in Reservoir Simulation

The injectivity index of a well block (i_m, j_m, k_m) is:

$$PI_{l,m} = \frac{k_{rl,i_m j_m k_m}}{\mu_{l,i_m j_m k_m}} WI_m \qquad [4.17]$$

where the constant portion WI_m is given in Eq. [2.14]. To correct polymer injectivity, the semi-analytical injectivity model is applied to the aqueous phase by replacing $\mu_{1,i_m j_m k_m}$ with the average apparent polymer viscosity, $\bar{\mu}_{1,i_m j_m k_m}$. For a multi-segmented well, the injection rate in Eq. [4.14] or Eq. [4.16] is the rate of aqueous phase in a certain well block given in Eq. [3.7]. In UTCHEM, we use the semi-analytical injectivity model for both injection wells and production wells.

The difference between the equivalent wellblock radius r_o defined in Eq. [2.15] and r_o^{uv}, or the wellbore radius r_w and $\bar{r}_w$ is small. If we neglect the small differences, the derivation for obtaining an average viscosity (Eq. [4.12]) will apply to many Peaceman-type well models using the concept of "equivalent wellblock radius", for example, Abou-Kassem and Aziz's work (1985) for wells located at anywhere in rectangular blocks, Babu and Odeh's work for horizontal wells (1989), and Dogru's work (2010a; 2010b) for partially penetrated wells which account for partial penetration and

vertical flow. However, rigorous derivations are required to extend these well models to non-Newtonian fluids, which is not the focus of current study. For modeling horizontal wells, the range of validity of Peaceman's well model was explored in the work by Peaceman (1993). Our semi-analytical polymer injectivity model would be restricted by the same valid conditions for Peaceman's well model.

The semi-analytical model was implemented in UTCHEM as a near wellbore option (ISHEAR=2). Other near-wellbore options include:

1. The effective radius method (Sharma et al., 2010)

   This is the method discussed in Chapter 2 (Eq. [2.64]). This option is an empirical method using an effective well radius, r_{weff}, to match the injectivity in a coarse grid simulation with a fine-grid simulation without correction.

2. The area equivalent radius method from ECLIPSE (Schlumberger, 2010)
   In ECLIPSE 2010, a similar treatment as the first method is used, where r_{weff} is taken as

$$r_{weff} = \sqrt{r_A r_w} \qquad [4.18]$$

   where r_A is an area equivalent radius of the well block equal to $\sqrt{\Delta x \Delta y / \pi}$.

   The method is also empirical.

One possible numerical issue with the semi-analytical model implemented in UTCHEM is that both apparent viscosity and the average apparent viscosity are explicitly calculated from previous timestep. Both apparent viscosity and the average apparent viscosity are functions of flow velocity (or pressure gradient) and saturation. The explicit nature of the UTCHEM may cause divergence in viscosity calculation or excessive numerical error. In UTCHEM simulations, small timesteps are used to guarantee

numerical stability of this IMPEC-type simulator, which could also help reduce numerical error in viscosity calculations. In our simulation studies, the current semi-analytical model works properly for both shear-thinning and shear-thickening polymers.

4.1.3 Validation of the Analytical Polymer Injectivity Model

4.1.3.1 Validation against Fine Grid Simulation

The semi-analytical polymer injectivity model was first tested using a single-phase polymer flooding case as a validation study. A 2D homogeneous isotropic reservoir (2700 ft × 2700 ft × 4 ft) with an inverted 5-spot well pattern was modeled. Injection well is on constant rate-constraint. Polymer solution is injected at 4000 ft^3/d and produced at 1000 ft^3/d at each production well. The details of the reservoir properties and polymer rheology are given in Table 4.1. The polymer solution is assumed to be shear-thinning and Meter's equation (Eq. [2.54]) is used.

The simulation model was run using different uniform grid sizes (300 ft × 300 ft × 4 ft, 30 ft × 30 ft × 4 ft, and 15 ft × 15 ft × 4 ft). As shown in Fig. 4.2, wellbore pressure of the injection well decreases drastically as grid size decreases, which is the "grid effect" mentioned earlier. Since 300 ft is not uncommon in conventional reservoir simulations, there is much room left for us to improve our prediction. We assume that the finest grid (15 ft × 15 ft × 4 ft) gives us the "true" value of the wellbore pressure. The coarsest grid (300 ft × 300 ft × 4 ft) was then repeated using the semi-analytical injectivity model (Eq. [4.13]) and also the Eq. [4.18] from ECLIPSE. From Fig. 4.2, we can see that the semi-analytical injectivity model gives a close estimate of well injectivity even for the coarsest grid simulation while the area equivalent method overestimates the apparent polymer viscosity at wellblocks.

4.1.3.2 Validation against Radial Grid Simulation

The second validation case has the same reservoir properties as the first one shown in Table 4.1. This case is at a constant-pressure outer boundary condition. A rate-constraint injection well is located in the center of the reservoir which has a radius of 350 ft. Two pore volumes (PV) of polymer solution were injected at a rate of 4000 ft^3/d. A radial reservoir simulation was run to accurately capture polymer injectivity using a grid size of 1 ft in the *r*-direction. Fig. 4.3 shows the pressure distribution of the radial case at 2 PVs. Three simulation cases were performed with different near-wellbore options (no modification, the semi-analytical injectivity model, and the area equivalent radius method) using coarse Cartesian grids. The model size of 770 ft × 770 ft × 4 ft was discretized into 11 × 11 × 1 grid blocks. The constant-pressure outer boundary condition was achieved with 16 pressure-constraint peripheral production well. Fig. 4.4 gives the pressure distribution using the analytical model at 2 PVs.

As shown in Fig. 4.5, the semi-analytical injectivity model predicted wellbore pressure very well after 1 PV of polymer solution was injected. The small discrepancy between the wellbore pressure from the semi-analytical model and that from the radial reservoir simulation is mainly due to the imperfection of using pressure-constraint well to mimic the constant-pressure outer boundary condition. Before injection of 1 PV of polymer solution, there is a relatively large discrepancy between the radial and the Cartesian grid simulation results. This discrepancy may be because of the dilution of polymer solution in the coarse Cartesian grids which smears the front of polymer solution. As more polymer solution was injected, the effect was gradually eliminated. From Fig. 4.5, we can see that without near-wellbore correction, wellbore pressure was erroneously calculated and the area equivalent method still overpredicted the injectivity.

4.2 FURTHER ENHANCEMENT IN SEMI-ANALYTICAL INJECTIVITY MODEL

4.2.1 Development of an Apparent Skin Model

The semi-analytical injectivity model needs to be programmed and implemented in a reservoir simulator. It is not practical for users of commercial simulators without access to the source code. To fix this problem, we revisited the semi-analytical injectivity model and proposed a non-intrusive way to correct well model by introducing an apparent skin factor which can be used as an input parameter to a simulator. The apparent skin factor, s_p, is estimated using polymer rheology, grid size, wellbore radius, etc.

The apparent skin factor, s_p, is defined following Bondor *et al.* (1972) as follows:

$$P_{wf} - P_o = \frac{q_1}{2\pi\left(k_x k_y\right)^{\frac{1}{2}} k_{r1}} \mu_1 \left(\ln \frac{r_o}{r_w} + s_p \right) \qquad [4.19]$$

where μ_1 is the viscosity at the wellblock based on average Darcy velocity from Eq. [2.52]. Then substitution of Eq. [4.19] into Eq. [4.11] gives:

$$s_p = \frac{\int_{\bar{r}=\bar{r}_w}^{\bar{r}=r_o^{uv}} \mu_{app}\left(\bar{r}\right) \frac{d\bar{r}}{\bar{r}}}{\mu_1} - \ln \frac{r_o}{r_w} \qquad [4.20]$$

Here we introduce an important assumption: the apparent viscosity of the aqueous phase at the wellblock can be estimated as

$$\mu_1 = \mu_{app}\left(r_A\right) \qquad [4.21]$$

where r_A is the area equivalent radius of the wellblock:

$$r_A = \sqrt{\frac{\Delta x \Delta y}{\pi}} \qquad [4.22]$$

Then Eq. [4.20] becomes:

$$s_p = \frac{\int_{\bar{r}=\bar{r}_w}^{\bar{r}=r_o^{uv}} \mu_{app}(\bar{r}) \frac{d\bar{r}}{\bar{r}}}{\mu_{app}(\bar{r}=r_A)} - \ln \frac{r_o}{r_w} \qquad [4.23]$$

For power-law model,

$$\mu_{app}(\bar{r}) = K \left(\frac{\gamma_c}{\sqrt{\bar{k}\bar{k}_{r1}\phi S_1}} \frac{q_1}{2\pi h \bar{r}} \right)^{n-1} \qquad [4.24]$$

Substitution of Eq. [4.24] into Eq. [4.23] gives:

$$s_p = \frac{1}{1-n} \left[\left(\frac{r_o^{uv}}{r_A} \right)^{1-n} - \left(\frac{\bar{r}_w}{r_A} \right)^{1-n} \right] - \ln \frac{r_o}{r_w} \qquad [4.25]$$

Eq. [4.25] is an interesting finding showing that the apparent skin factor for power-law fluid is a function of grid size, wellbore radius, and power law exponent n. It is irrelevant to the power law coefficient, K, and the injection rate. Besides, when n is close to 1, s_p is close to zero.

For Meter's equation (Eq. [2.54]), using similar treatment gives:

$$s_p = \frac{\mu_\infty \ln \frac{r_o}{r_w} + \frac{\mu_p^0 - \mu_\infty}{P_\alpha - 1} \ln \frac{\left(r_o^{uv}\right)^{P_\alpha - 1} + R_p^{P_\alpha - 1}}{\left(\bar{r}_w\right)^{P_\alpha - 1} + R_p^{P_\alpha - 1}}}{\mu_\infty + \frac{\mu_p^0 - \mu_\infty}{1 + \left(\frac{R_p}{r_A}\right)^{P_\alpha - 1}}} - \ln \frac{r_o}{r_w} \qquad [4.26]$$

and for the Carreau model (Eq. [2.56]), this approach gives:

$$s_p = \frac{\int_{\bar{r}=\bar{r}_w}^{\bar{r}=r_o^{uv}} \left\{ \mu_\infty + \left(\mu_p^0 - \mu_\infty\right) \left[1 + \left(\frac{R_{pc}}{\bar{r}} \right)^2 \right]^{(n_1-1)/2} \right\} \frac{d\bar{r}}{\bar{r}}}{\mu_\infty + \left(\mu_p^0 - \mu_\infty\right) \left[1 + \left(\frac{R_{pc}}{r_A} \right)^2 \right]^{(n_1-1)/2}} - \ln \frac{r_o}{r_w} \qquad [4.27]$$

Finally, a more complex form can be obtained for the UVM model (Eq. [2.55]) based on Eq. [4.23] and Eq. [4.15].

Intuitively, we know that Eq. [4.25] gives good approximation for Eq. [4.26] and Eq. [4.27] when the shear regime of a polymer solution is power-law within the wellblock. Moreover, the apparent skin factor from Eq. [4.26] or Eq. [4.27] should be relatively independent of injection rate, thickness of grid block, and permeability. However, the apparent skin factor from Eq. [4.25] fails to give a good estimate of the apparent skin factor for the UVM model due to the impact of the shear-thickening behavior.

4.2.2 Validation of the Apparent Skin Model

For a homogeneous and isotropic reservoir with square and uniform grid blocks with grid size equal to 300 ft, 150 ft, 30 ft and 3 ft, the corresponding apparent skin factor for power law model (Eq. [4.25]) as a function of power-law exponent, n, was plotted in Fig. 4.6. For shear-thinning fluids, n ranges from 0 to 1. When n increases from 0 to 1, the non-Newtonian fluid becomes less shear-thinning and magnitude of the negative skin factor decreases from the maximum value to zero as shown in Fig. 4.6. Another observation from Fig. 4.6 is that the magnitude of the apparent skin factor increases as the grid size increases, which means fine grid models capture the shear-thinning behavior better than models with coarse grid sizes. For a homogeneous and isotropic reservoir with square and uniform gridblocks, the corresponding apparent skin factor for power law model (Eq. [4.25]) as a function of grid size with n equal to 0.9, 0.8, 0.7 or 0.1 was plotted in Fig. 4.7. For a wellbore radius of 0.25 ft, the grid size allowed for Peaceman's well model should be greater than 1.25 ft. When the grid size approaches 1.25 ft, the apparent skin factor approaches 0. When the grid size increases, the magnitude of skin factor increases to such an extent that even for slightly shear-thinning fluid with n = 0.9, a correction to injectivity is necessary.

The apparent skin factor model for power law fluids may not be accurate enough for non-Newtonian fluids with near-wellbore effective shear rates outside of power law range. Therefore, it is necessary to compare the results from power law model with other rheological models. For the Meter's equation with parameters shown in Table 4.2 and the same homogeneous and isotropic reservoir with square and uniform grids (fixed at 300 ft), we can compare the calculated apparent skin factor with that from the power law model as shown in Fig. 4.8. After the key parameter $q_1 / \left(2\pi h \sqrt{k k_{r1} \phi S_1}\right)$ increases above about 100 m/s, the apparent skin factor decreases to about -4 and remains almost

constant. For typical values, q_1 = 800 bbls/d, $k\ k_{r1}$ = 1 Darcy, and ϕS_w = 0.2, the key parameter $q_1/\left(2\pi h\sqrt{kk_{r1}\phi S_1}\right)$ is calculated as 432.6 m/s, which is large enough to reach the "constant regime" of the apparent skin factor. For the constant regime, Meter's equation and the power law model (n = 2-P_α) give similar results. Take q_1 = 800 bbl/d, kk_{r1} = 1 Darcy, and ϕS_w = 0.2 as an example. Meter's equation gives s_p = -4.22 and the power-law model gives s_p = -4.62. The difference is because when the shear rate is very high, power-law model gives ultra-low viscosity instead of the second Newtonian Plateau at high shear rates. Thus, power-law model overpredicts the apparent skin factor. For the Carreau model with parameters shown in Table 4.3 and the same reservoir with grid size of 300 ft, similar results to those from Meter' equation in Fig. 4.9 are observed. For q_1 = 800 bbl/d, kk_{r1} = 1 Darcy, and ϕS_w = 0.2, the Carreau model predicts s_p = -2.52 and the power -law model ($n = n_1$) gives s_p = -2.81.

If we switch to the UVM model with parameters given in Table 4.4, the calculated apparent skin factor compared with that from the power law model is shown in Fig. 4.10. Different from those results from Meter's equation or the Carreau model, no constant regime exists for apparent skin factor in the shear rate regime of interest. As the key parameter $q_1/\left(2\pi h\sqrt{kk_{r1}\phi S_1}\right)$ increases, the apparent skin factor decreases at the beginning until $q_1/\left(2\pi h\sqrt{kk_{r1}\phi S_1}\right)$ reaches a critical value. After that, the apparent skin factor gradually increases to positive values, which means polymer shear-thickening may limit the injectivity. For q_1 = 800 bbl/d, kk_{r1} = 1 Darcy, and ϕS_w = 0.2, the UVM model gives s_p = 2.05 and the power-law model ($n = n_1$) gives s_p = -2.81.

The studies on apparent skin factor for different polymer rheology show that for shear-thinning fluids, the apparent skin factor is almost constant for a wide range of injection rates. Therefore, the apparent skin factor can be used as an input parameter to simulate the injectivity of polymer solutions. For shear-thickening fluids, the apparent

skin factor is sensitive to the injection rate and may be used in some simple simulation cases with constant injection rates and homogeneous permeabilities. For pressure constraint wells, the injection rate may vary from a small value with the shear rate in the Newtonian regime of high polymer viscosity to a high value in the shear rate of the power-law or the shear-thickening regimes. Then the apparent skin factor may vary significantly and cannot be represented with a constant value.

To validate the apparent skin factor concept, the radial grid simulation case in Section 4.1.3.2 for validating the semi-analytical polymer injectivity model was repeated. A coarse-grid simulation using a predicted apparent skin factor of -2.86 was compared with other simulation cases as shown in Fig. 4.11. The results show that the model using an apparent skin factor gives very close results compared with the semi-analytical injectivity model and the fine-grid radial simulation.

Rock Compressibility, psi^{-1}	0
Permeability in X or Y Direction, md	1000
Porosity	0.2
Initial Reservoir Pressure, psi	1200
Initial Water Saturation	1
Residual Water Saturation	0
Anion Concentration, meq/ml	0.33
Water Viscosity, cp	0.85
Water Compressibility, psi^{-1}	0.000003
Polymer Concentration, wt%	0.3
AP1, AP2, AP3	20.3, 0, 2390.7
BETAP, CSE1, SSLOPE	1, 0.01, 0
GAMMAC, GAMHF, POWN, GAMHF2	24, 1354.9, 1.7, -13.97
Well Radius, ft	0.3

Table 4.1: Reservoir and polymer properties for validation cases 1 and 2.

μ_p^0, cp	60.89
μ_w, cp	0.85
P_α	1.7
$\dot{\gamma}_{1/2}$, sec^{-1}	20.50
C	6
Grid size, ft	300

Table 4.2: Parameters for Meter's equation.

μ_p^0, cp	13.13
μ_w, cp	0.80
n_1	0.78
λ_1 ,sec	0.22
C	6
Grid size, ft	300

Table 4.3: Parameters for the Carreau model.

μ_p^0, cp	13.13
μ_w, cp	0.80
n_1	0.78
λ_1, sec	0.22
μ_{max}, cp	10.93
n_2	3.5
$\lambda_2\tau$, sec	0.00048
C	6
Grid size, ft	300

Table 4.4: Parameters for the UVM model.

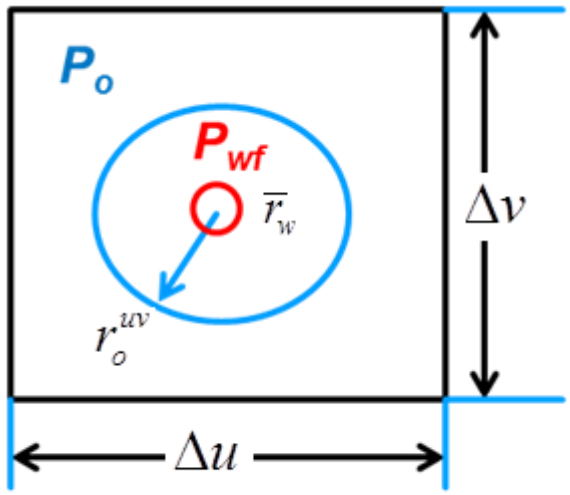

Figure 4.1: The critical region of Peaceman's well model.

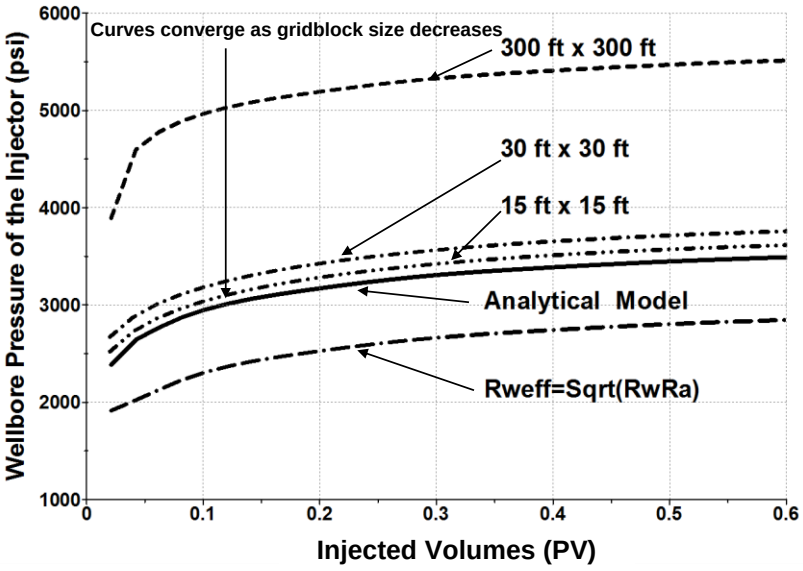

Figure 4.2: Validation case 1: injector wellbore pressure vs. pore volume injected.

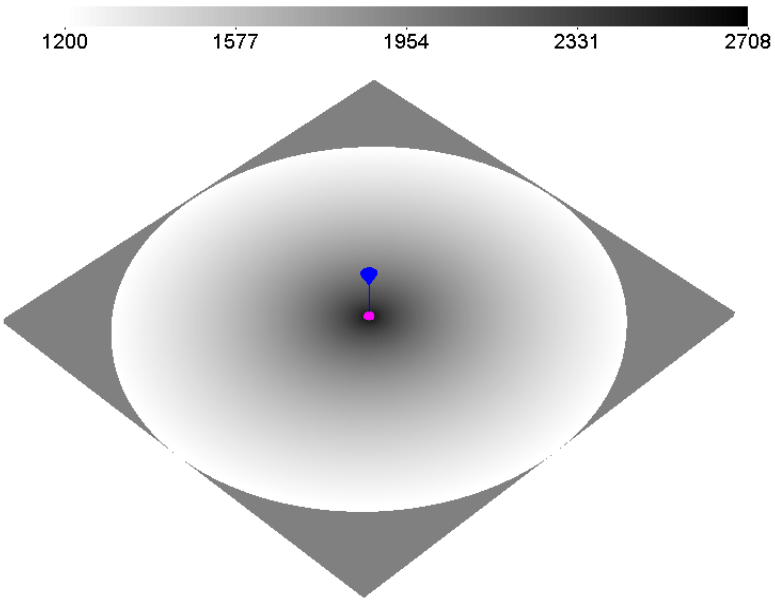

Figure 4.3: Validation case 1 (radial grid simulation): reservoir pressure (psi) distribution at 2 PVs.

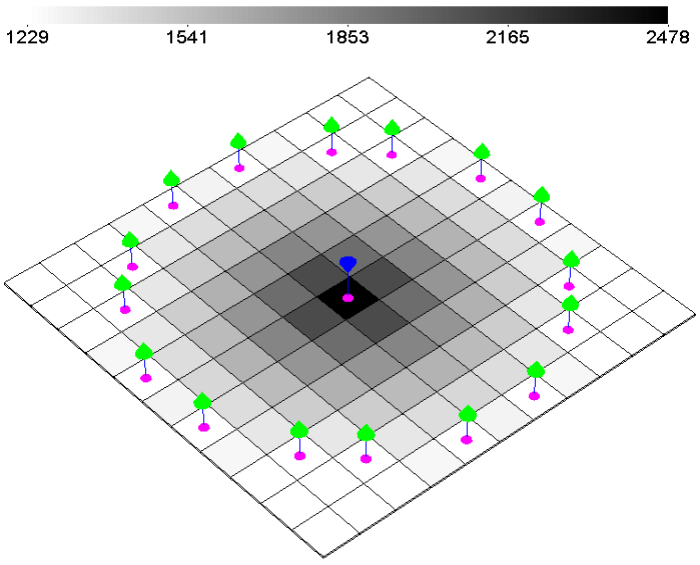

Figure 4.4: Validation case 1 (Cartesian grid simulation): reservoir pressure (psi) distribution at 2 PVs.

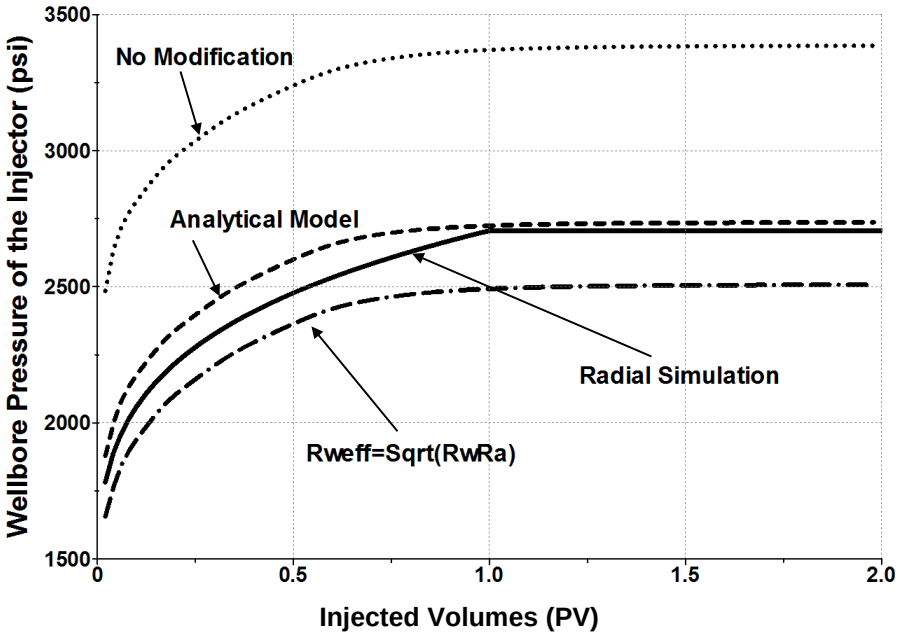

Figure 4.5: Validation case 2: injector wellbore pressure vs. pore volume injected.

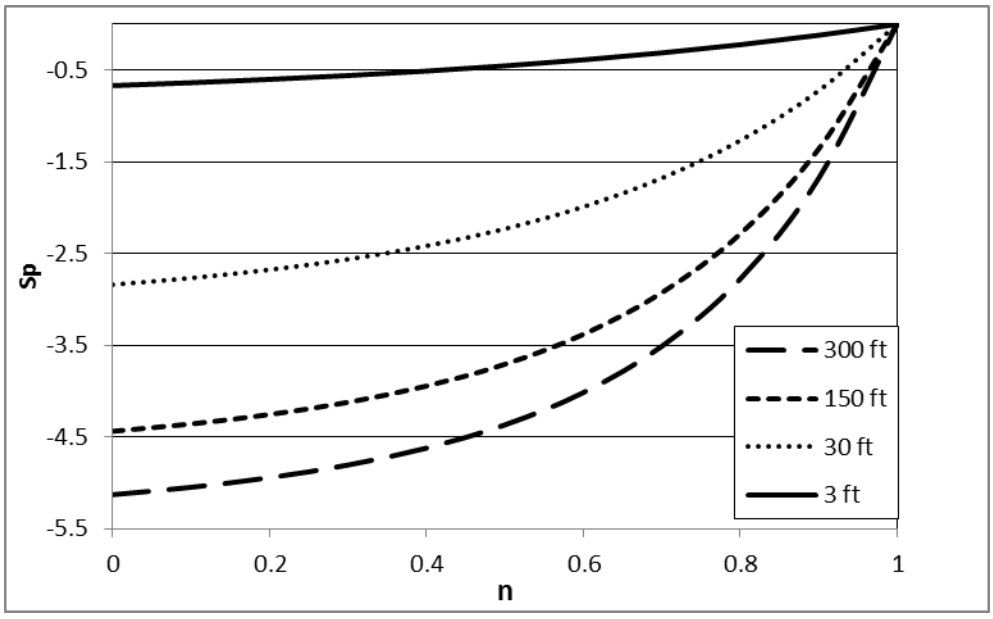

Figure 4.6: Apparent skin factor of different grid sizes vs. power law exponent for the power law model.

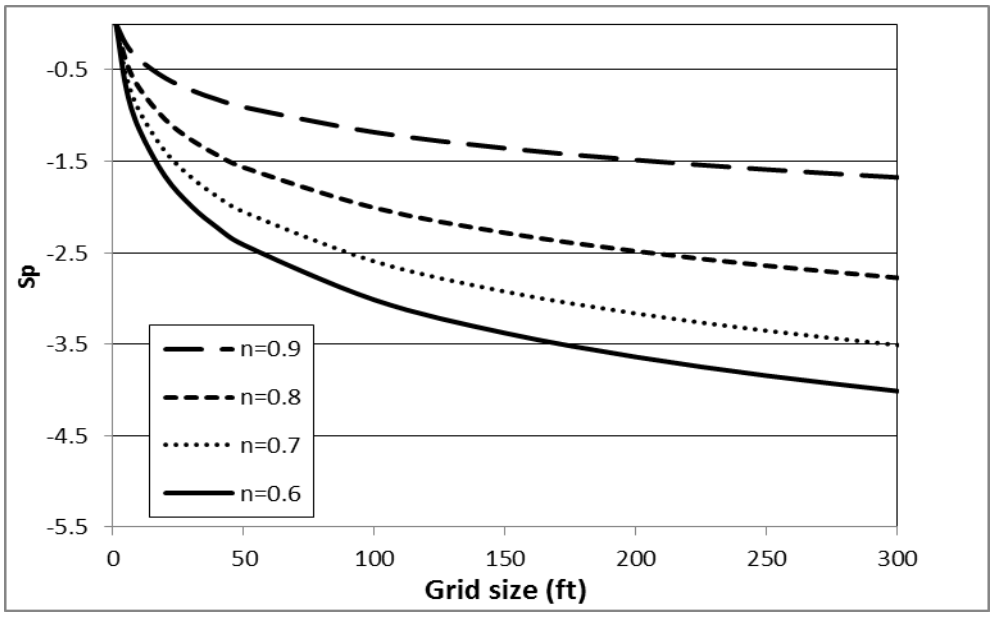

Figure 4.7: Apparent skin factor of power law exponents vs. gridblock size for the power law model.

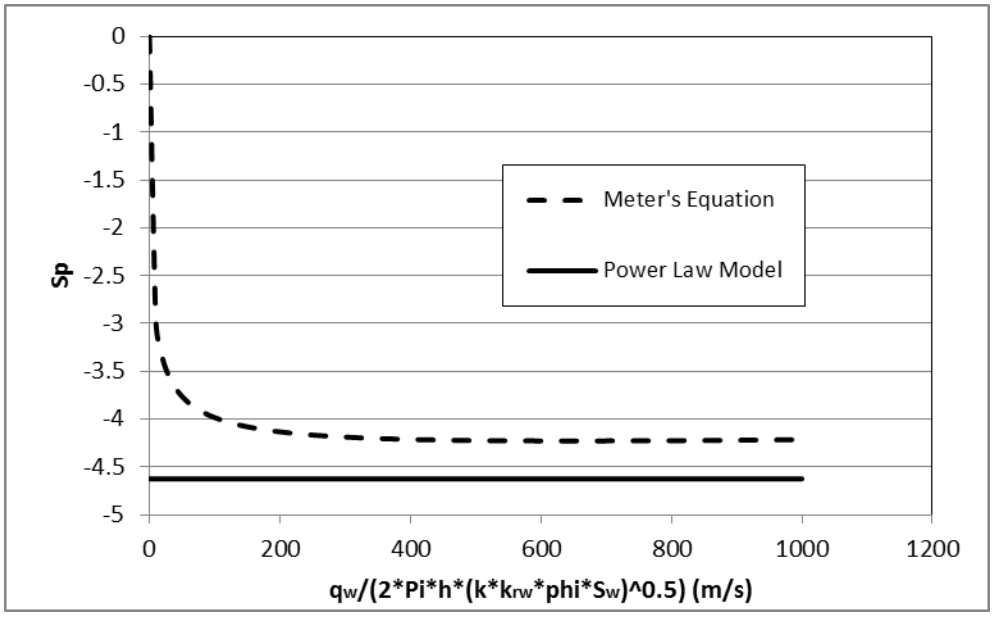

Figure 4.8: Meter's equation vs. power law model for apparent skin factor estimation.

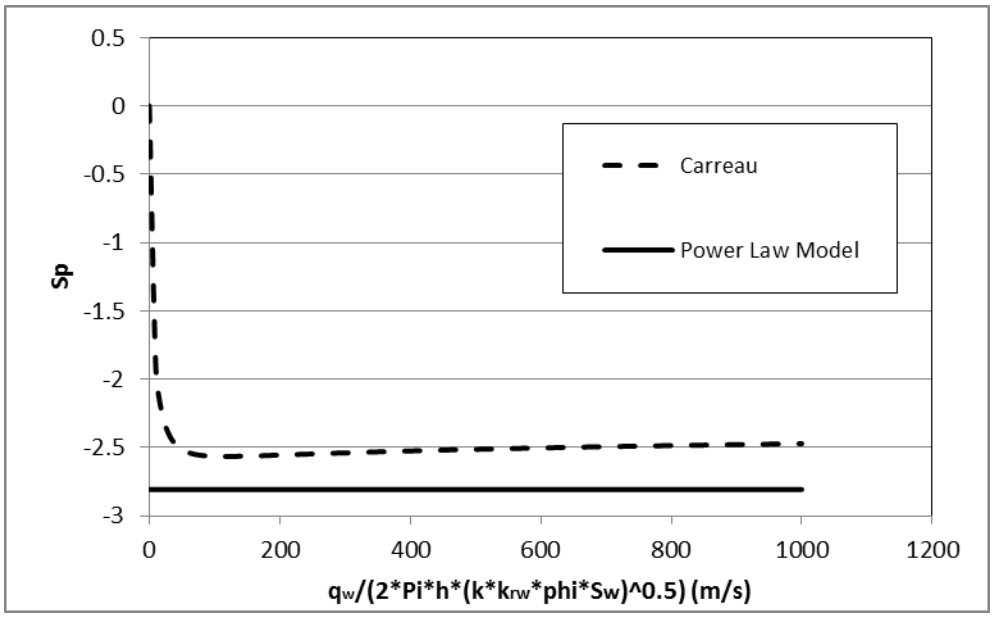

Figure 4.9: The Carreau model vs. power law model for apparent skin factor estimation.

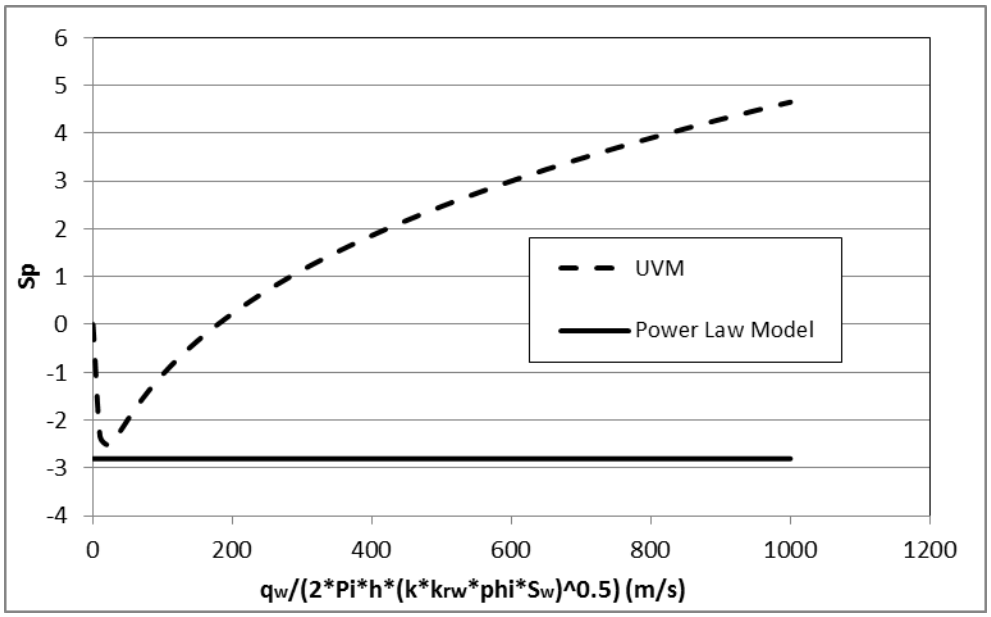

Figure 4.10: The UVM model vs. power law model for apparent skin factor estimation.

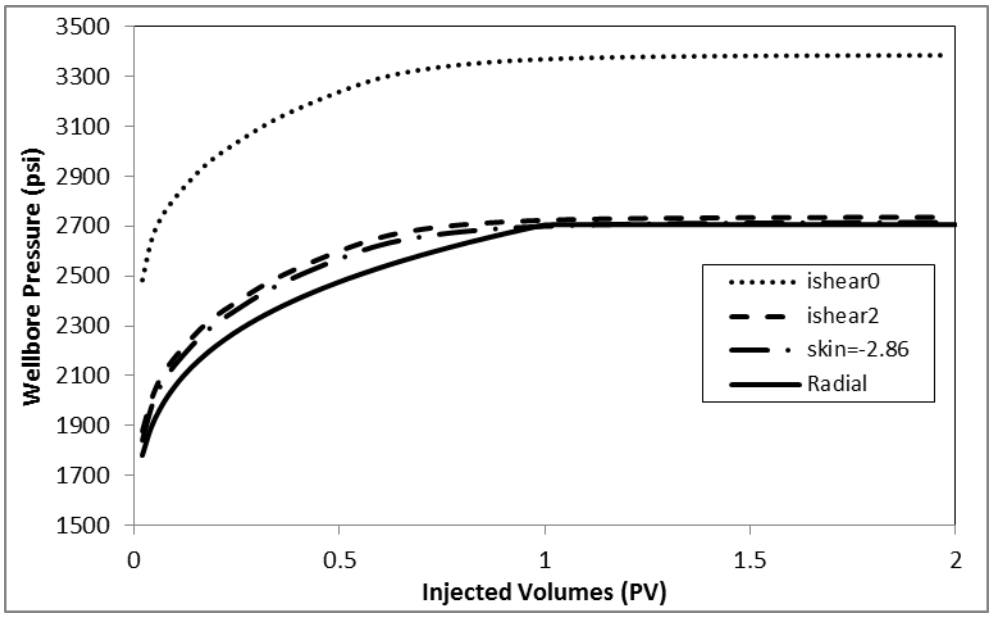

Figure 4.11: Wellbore pressure calculated using well model without modification (ishear0), analytical injectivity model (ishear 2), apparent skin factor (s_p = -2.86), and fine-grid radial simulation.

Chapter 5: Simplified Representation of Fracture

In this chapter, we model a two-dimensional fracture with a fixed height along a vertical well. Our induced fracture model includes three equations: (1) an elasticity equation that determines the fracture shape with the fluid pressure in fracture and rock properties; (2) a fluid-flow equation that determines the fluid pressure distribution from wellbore to fracture tip; and (3) a propagation criterion that determines fracture extension/shrinkage. It differs from many conventional hydraulic fracture models which emphasize a mass/volume balance equation that relates fracture propagation rate with injection rate and leak-off rate (Settari, 1980; Nghiem *et al*., 1984), which many cause singularity due to large injection and leak-off rates compared to cases with negligible fracture volume growth rate (Ji *et al*., 2004). The induced fracture model is implicitly coupled with UTCHEM.

5.1 Polymer Rheology Inside of Fracture

Induced fracture is created during injection of displacing phase, e.g. water or polymer solutions, at high injection rate. The displacing phase is not deliberately designed viscous fracturing fluids with proppants which are used to maintain fracture aperture after injection ceases. The induced fracture is considered to be void and will close completely if the injection ceases. Zechner *et al*. (2013) conducted micromodel experiments of polymer flow through designed fractures, and confirmed that polymer rheology inside of the fracture is shear-thinning only. In this study, we assume polymer viscosity inside fracture can be described as the bulk viscosity and shows only shear-thinning behavior. The bulk viscosity is modeled using the power law model (Eq. [2.28]). Hejri *et al.* (1991) showed that the power law parameters K and n could be correlated smoothly with polymer concentration for their experimental data:

$$K = a_1 + a_2 C_p^{\,a_3} \qquad [5.1]$$

and

$$n = \frac{1}{1 + b_1 C_p^{b_2}} \qquad [5.2]$$

where a_1, a_2, a_3, b_1 and b_2 are all positive value fitting parameters. For data from Hejri *et al*. (1991), the best match gives a_1, a_2, a_3, b_1 and b_2 equal to 5.435, 0.00002362, 2.286, 0.002 and 0.943 respectively. Eqs. [5.1] and [5.2] show that K increases as polymer concentration increases; n decreases as polymer concentration increases. In this study, Eqs. [5.1] and [5.2] are used to correlate polymer viscosity in fracture with polymer concentration. Factors such as brine salinity, temperature, etc. are not considered.

5.2 FRACTURE MECHANICS

A simplified representation of fracture was proposed based on assumptions below:

- The fracture can be described with the KGD model which is a two-dimensional model. It has two symmetrical wings and a fixed height. Each wing of the fracture is a rectangular slit with varying width. The elasticity equation based on the KGD model determines fracture geometry at given fracture/pore pressure and in-situ stresses;
- The fracture length is determined using the Barenblatt's Equilibrium Condition;
- Fluid pressure inside fracture varies from the wellbore to fracture tip;

- Polymer concentration inside fracture is assumed to be the same as what in the wellbore (i.e. injected concentration);
- Single-phase fluid inside the fracture;
- Fluid leak-off is uniform along the fracture and overall leak-off rate equals to the total injection rate. The increase in fracture volume is neglected;
- Currently the impact of thermal stresses due to cold fluid injection is neglected;
- Impact of water quality or particle plugging is neglected;
- Natural fractures or shadow effects are not considered;
- Only one injection well is fractured and only one injection-induced fracture is modeled.

5.2.1 Fracture Initiation

The pressure equation for fracture initiation was derived by Hagoort (1978):

$$p_{fi} = \frac{3\sigma_h - \sigma_H - A_{pe}\Delta p + \sigma_t}{2 - A_{pe}} \qquad [5.3]$$

where p_{fi} is the fracture initiation pressure, Δp is the change in reservoir pressure, σ_t is the tensile strength of reservoir rock, σ_H is the maximum horizontal stress, σ_h is the minimum horizontal stress, and A_{pe} is the poroelastic constant of the rock:

$$A_{pe} = \alpha_B \frac{1-2\nu}{1-\nu} = \left(1 - \frac{c_m}{c_r}\right)\frac{1-2\nu}{1-\nu} \qquad [5.4]$$

where α_B is the Biot's constant, ν is the Poisson's ratio, c_m is the compressibility of rock matrix, and c_r is the compressibility of porous media.

5.2.2 Fracture Opening/Closing

The pressure equation for fracture opening/closing is:

$$p_{foc} = \sigma_h \tag{5.5}$$

where p_{foc} is the fracture opening/closing pressure.

5.2.3 In-Situ Stresses

The change of reservoir pressure has an impact on in-situ stresses (Gidley *et al*., 1989). For minimum horizontal stresses,

$$\sigma_h = \sigma_{hi} + A_{pe}\Delta p \tag{5.6}$$

where σ_{hi} is the initial minimum horizontal stress. For maximum horizontal stresses,

$$\sigma_H = \sigma_{Hi} + A_{pe}\Delta p \tag{5.7}$$

where σ_{Hi} is the initial maximum horizontal stress.

5.2.4 Fracture Geometry

Two-dimensional fracture models assume a fracture of specified height but variable lengths and widths. Two well-known 2D fracture models, which are widely used in industry, are the PKN model and the KGD model. The PKN model was introduced by Perkins and Kern (1961) and further developed by Nordgren (1972), while the KGD

model originated from Khristianovich and Zheltov's first work (1955) and was proposed by Geertsma and de Klerk (1969). These two models differ from each other in one assumption: while the PKN model assumes plain strain in vertical directions, the KGD model assumes plain strain in horizontal directions. Due to this difference, these two models are incompatible. The PKN model is a good approximation when the fracture length/height ratio is large while the KGD model is good for small length/height ratio.

In this study, we adopted the KGD model. Based on the KDG model, the relationship between fracture width, fracture fluid pressure and fracture opening/closing pressure can be given as

$$w_f(x_f) = \frac{4(1-\nu^2)}{E} L_f \left[p_f(x_f) - p_{foc} \right] \qquad [5.7]$$

where w_f is the fracture width, E is the Young's modulus, p_f is the fracture fluid pressure, x_f is the distance from the wellbore to an arbitrary location along one wing of the fracture.

5.2.5 Fluid Mechanics inside Fracture

Fluid pressure distribution inside of the fracture has an impact on fracture geometry and fracture propagation. Perkins *et al*. (1961) approximated the fracture with a two-parallel-plane slit of variable width and obtained an analytical solution of the pressure drop for their PKN-shape fracture considering Newtonian fluids and turbulent effect. Suri *et al.* (2009) assumed uniform leak-off along the fracture and extended the solution by Perkins *et al*. (1961) to power law fluids. Geertsma *et al*. (1969) derived another solution for their KGD-shape fracture considering Newtonian fluids and they pointed out that Perkins' solution would underestimate fluid pressure or fracture width.

To calculate pressure distribution within a KGD-shape fracture considering non-Newtonian fluids and also turbulent effect, we employed the analytical solution by Bird *et al*. (2007) on flow of a power law fluid through a narrow slit. If uniform leak-off is assumed, we obtain the analytical form of the solution for pressure drop in the fracture as follows (see Appendix A for derivations):

$$\Delta p_{f\max} = \left\{ 4C_{Turb} K \left(\frac{2n+1}{n} \frac{1}{h_f} \right)^n \left(\frac{E}{4(1-\nu^2)L_f} \right)^{2n+1} q_{inj}^n L_f \right\}^{\frac{1}{2n+2}} \quad [5.8]$$

where $\Delta p_{f\max}$ is the maximum pressure drop within the fracture, and C_{Turb} is the correction factor for turbulent effect. C_{Turb} equals 1 when the flow is laminar and C_{Turb} equals $16/3\pi$ when it is turbulent. The pressure drop along the fracture is calculated as

$$p_f(x_f) - p_{foc} = \Delta p_{f\max} \left(1 - \frac{x_f}{L_f} \right)^{\frac{1}{2}} \quad [5.9]$$

Thus substitution of Eq. [5.9] into Eq. [5.7] gives:

$$w_f(x_f) = \left[\frac{4(1-\nu^2)L_f}{E} \Delta p_{f\max} \right] \left(1 - \frac{x_f}{L_f} \right)^{\frac{1}{2}} \quad [5.10]$$

The solution, Eq. [5.8] qualitatively agrees with the solution proposed by Suri *et al*. (2009) or the one by Geertsma *et al.* (1969). Further discussion of this solution is given in Appendix B.

5.2.6 Barenblatt's Equilibrium Condition

The Barenblatt's equilibrium condition gives (Gidley *et al.,* 1989):

$$\int_0^{L_f} \frac{p_f(x_f) - p_{foc}}{\sqrt{L_f^2 - x_f}} dx_f = \frac{K_{IC}}{\sqrt{\pi L_f}} \qquad [5.11]$$

where K_{IC} is the critical stress-intensity factor. Geertsma *et al*. (1969) calculated the pressure drop after assuming K_{IC}=0. Similar treatment was adopted for deriving Eq. [5.8]. To take K_{IC} into account, inclusion of Eq. [25] into our derivations gives:

$$p_{f\max} = p_{foc} + \Delta p_{f\max} + \frac{K_{IC}}{\sqrt{\pi L_f}} \qquad [5.12]$$

where the maximum fluid pressure in the fracture, p_{fmax}, should be equal to the wellbore pressure, p_{wf} .

5.3 Coupling Fracture Model with Reservoir Simulation

Accurate modeling of fracture in reservoir simulation requires very fine grids of the same width as the fracture width. This limits the timestep size and increases the number of gridblocks (Lee *et al.*, 2011). When fracture propagates, fracture length may experience numerical oscillation if fracture grid size is not fine enough along the propagation direction. As a result, representation of fracture with fine fracture grids dramatically increases the computational time and also causes numerical instabilities (Ji

et al., 2004). Several other methods were proposed to achieve better computational efficiency and numerical stability. Few methods to represent fractures in reservoir simulation using only one grid system are listed below:

- The "transmissibility modification" proposed by Settari *et al*. (1990) represents a fracture through a reservoir block and its neighboring block by modifying their transmissibilities. Besides, the well index of a fractured wellblock needs to be modified to include the effect of fracture. This method has been fully studied and discussed in the work by Ji *et al*. (2004a) and Ji *et al*. (2004b).
- The "source and sink" method proposed by Nghiem *et al*. (1983) assumes an infinite conductivity fracture and an elliptical flow around fracture and represents fracture with sink or source terms similar to the treatment of well in reservoir simulation. However, it is not easy to extend this method to heterogeneous reservoirs.
- The "average permeability" method proposed by Gadde *et al*. (2001) models the fracture by averaging its high permeability with the low matrix permeability, which is very similar to the transmissibility modification method. This method is adopted in this study and elaborated as follows for gridblocks fully/partially penetrated by a fracture.

Assuming the fracture is not propped and flow is single-phase and laminar, the fracture permeability in a reservoir block can be calculated as

$$k_f = \frac{\bar{w}_f^2}{12} \qquad [5.13]$$

where $\bar{w}_f$ is the average fracture width. When fracture propagates, it penetrates through or into neighboring reservoir blocks. For a *fully penetrated* reservoir block, the reservoir permeabilities in the x- and z- directions are modified as

$$k_x^{'} = \frac{\bar{w}_f}{\Delta y}(k_f - k_x) + k_x \qquad [5.14]$$

and

$$k_z^{'} = \frac{\bar{w}_f}{\Delta y}(k_f - k_z) + k_z \qquad [5.15]$$

Unlike the method proposed by Gadde *et al.* (2001), permeability in the y-direction is not modified. For a *partially penetrated* matrix block, the reservoir permeabilities in the x- and z- directions are modified as

$$k_x^{"} = \frac{\Delta x}{\frac{L_{fp}}{k_x^{'}} + \frac{\Delta x - L_{fp}}{k_x}} \qquad [5.16]$$

and

$$k_z^{"} = \frac{\bar{w}_f L_{fp}}{\Delta x \Delta y}(k_f - k_z) + k_z \qquad [5.17]$$

where L_{fp} is the partial length of the fracture in the partially penetrated reservoir block, and Δx and Δy are the matrix block sizes in the x- and y- directions respectively. For a

partially penetrated well block, slight changes are made to Eq. [5.16] and Eq. [5.17] to guarantee a continuous transition when fracture initiates:

$$k_x''' = \frac{\Delta x}{\frac{2(L_f - r_w)}{k_x'} + \frac{\Delta x - 2(L_f - r_w)}{k_x}} \qquad [5.18]$$

and

$$k_z'' = \frac{2\bar{w}_f (L_f - r_w)}{\Delta x \Delta y}(k_f - k_z) + k_z \qquad [5.19]$$

where r_w is the wellbore radius. Without a fracture, L_f=r_w, the matrix block permeabilities are not changed.

The impact of fracture volume on pore volume is assumed negligible and porosity of the gridblock is not adjusted in current study. Permeability contrast between matrix and fracture affects the stability of the coupled model. This can be improved by using an upper limit for the fracture permeability and predefined infinite dimensionless fracture conductivity (Ji *et al.,* 2004):

$$InfCond = \frac{\left(k_f w_f\right)_{\max}}{k_x L_f} \qquad [5.20]$$

where k_x is the reservoir permeability in the x-direction.

5.4 SIMULATION PROCEDURE

An iterative scheme is used to implicitly couple the fracture model with UTCHEM. The iterative scheme is designed to minimize changes to UTCHEM and adapt to simulations of a variety of EOR processes using polymers.

In UTCHEM, the pressure equation is solved first. When wellbore pressure is greater than fracture initiation pressure, fracture module is activated. Then the iterative process begins. The information of fracture geometry to update its permeability/transmissibility matrix are required to calculate the reservoir pressure. The fracture geometry is determined by fracture half-length, fracture fluid pressure and reservoir pressure given rock mechanical properties. Fracture fluid pressure is a function of fracture half length. Three unknowns are interrelated the fracture geometry, fracture fluid pressure, and the reservoir pressure, which requires an iterative solution. Our solution scheme is outlined below:

1. Calculate the fracture opening/closure pressure, p_{foc}, from the reservoir pressure p at previous timestep n;
2. Assume the fracture geometry is unchanged and calculate the reservoir pressure p and the wellbore pressure p_{wf};
3. Calculate the maximum fracture fluid pressure p_{fmax} using Eq. [5.11].
4. If the difference between the wellbore pressure p_{wf} and the maximum fracture fluid pressure p_{fmax} is smaller than the given tolerance, accept the current fracture geometry and update other reservoir/fluid properties and proceed to the next timestep, $n+1$; if the error is not acceptable, continue to the procedure below:
    a. Calculate the fracture fluid pressure distribution, fracture geometry and update the reservoir permeability/transmissibility;
    b. Calculate the reservoir pressure and wellbore pressure;

c. Update the fracture half-length using the Illinois algorithm (Dowell and Jaratt., 1971) based on the difference between p_{wf} and p_{fmax};

d. If the difference between the fracture half-length calculated by the current iteration (v+1) and that from previous iteration (v) is small enough, accept the current fracture half-length and geometry, and update reservoir/fluid properties; go to next timestep $n+1$. If the error is not acceptable, go back to Step a.

The Illinois algorithm is explained in Appendix C. The solution of fracture half-length is limited within the range between wellbore radius and the prefixed maximum allowable fracture length. When there is no solution within this range, the simulation process ceases since fracture exceeds the bound. To avoid possible multiple solutions of fracture half-length, the fracture half-length is searched in the direction based on the sign of the value of (p_{wf}-p_{fmax}). Besides, the search region starts from the region around the previous solution and the span gradually increases until a single solution is found. The flow chart is shown in Fig 5.3.

5.5 VALIDATION OF THE AVERAGE PERMEABILITY METHOD

To validate the implementation of the average permeability method for coupling a fracture with the reservoir matrix, a single-phase 2D model was set up. One injector is located at the center of the reservoir with fixed injection rate. This model is discretized using 51×51×1 gridblocks. The input parameters are given in Table 5.1. Two simulation cases were studied. The first one uses the average permeability method for coupled static fracture through the injector. The second one uses equivalent high permeability reservoir block based on the dimensionless fracture conductivity. The calculated equivalent permeability is 5263.74 darcys. The reservoir pressure distribution after 5 days of water

injection is shown in Fig. 5.4. Results for the two simulation cases show a very close match.

Reservoir dimensions in x, y, z directions, ft	1181, 1181, 13
Rock compressibility, psi^{-1}	0
Porosity	0.2
Matrix permeability, md	1026
Fracture length, ft	196.85
Fracture width, ft	0.0109
Initial water saturation	1
Initial reservoir pressure, psi	1000
Fluid viscosity, cp	7.776
Water compressibility, psi^{-1}	0.00000069
Oil compressibility, psi^{-1}	0.00001
Injection rate, bbl/D	37.764

Table 5.1: Reservoir and fluid properties for a 2D areal model.

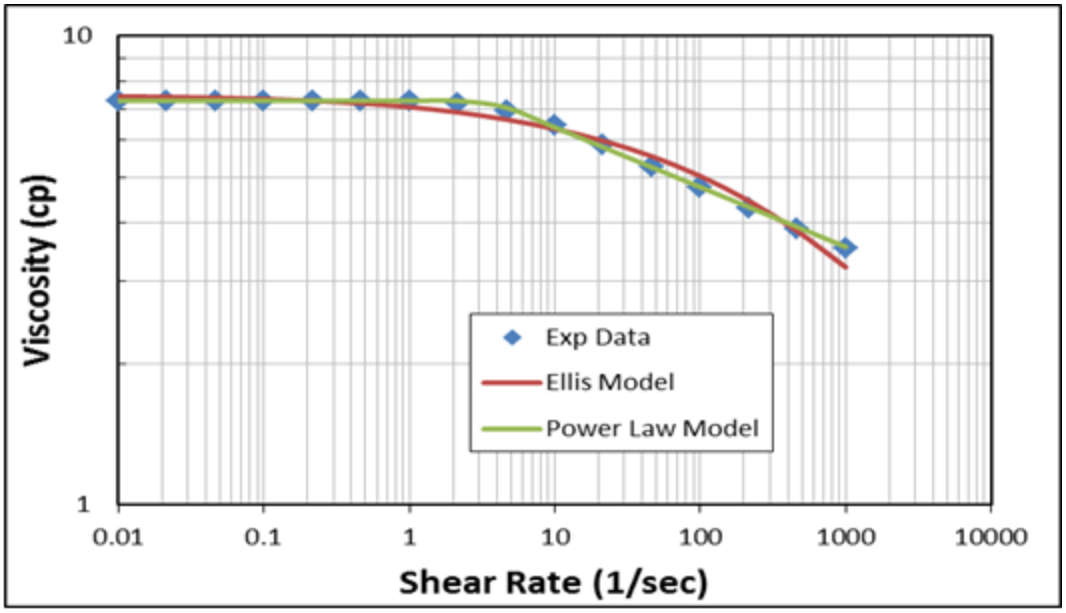

Figure 5.1: Polymer rheological data of Flopaam 3330S at 1000 ppm matched with the Ellis model and the modified power law model.

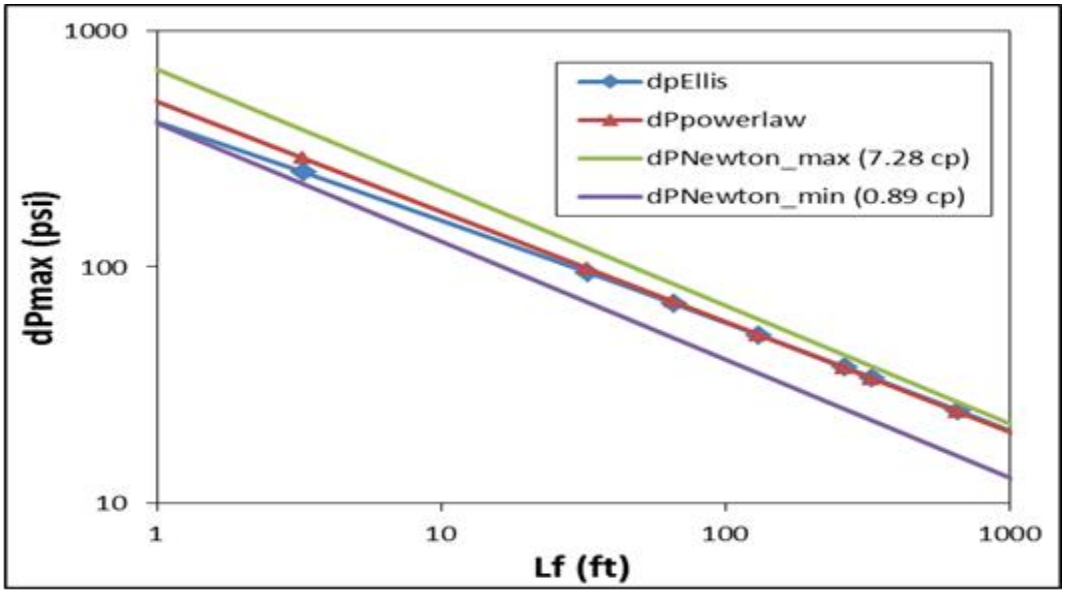

Figure 5.2: Maximum pressure in the fracture (log scale) vs. fracture length (log scale) calculated from different models: the Ellis model, the power law model, the Newtonian fluid model (upper and lower Newtonian viscosity).

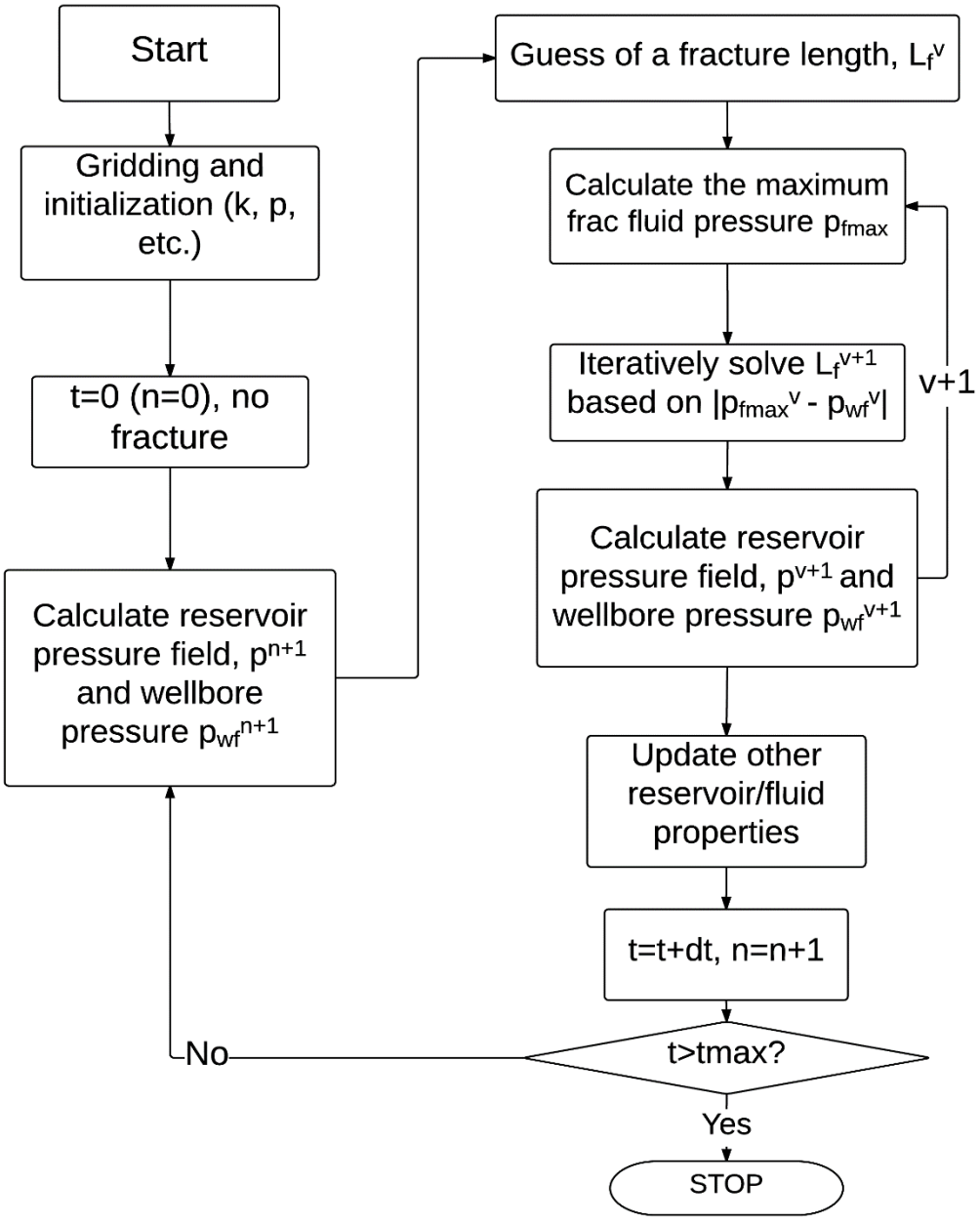

Figure 5.3: Flow chart for UTCHEM coupled with fracture model.

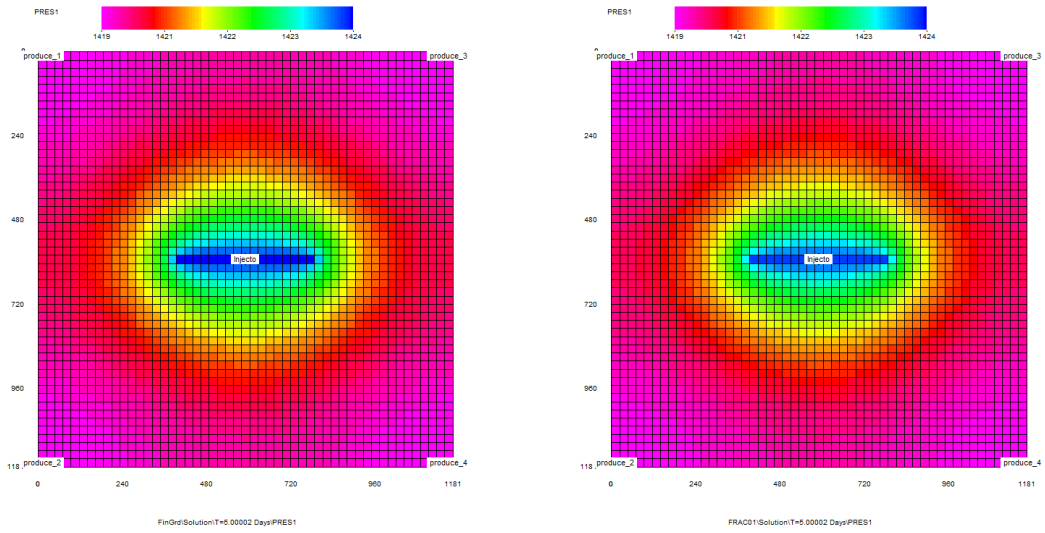

(a) (b)

Figure 5.4: Pressure distribution for 2D verification model with one injection well in the center: (a) simulation case using the average permeability method; (b) simulation case using high permeability reservoir block.

Chapter 6: Polymer Flooding Simulation Case Studies[3][4]

In this chapter, we present several polymer flooding simulation case studies based on our modeling improvements for polymer rheology, complex reservoir studies, near wellbore effects and fracture propagation.

6.1 Polymer Rheological Properties

A thorough understanding of polymer rheology is crucial to polymer flooding simulation and forecasting the field response and forms the basis of our study in this dissertation. Polymer shear-thinning behavior can be well-described using the capillary bundle model. One of the most arguable and ambiguous concept in modeling the polymer rheology using the capillary bundle model is the shear rate correction factor briefly explained in Chapter 2.

Experimental studies by Gogarty (1967) showed that C should be correlated to permeability and porosity; small permeability and porosity would lead to large C. Besides, Gogarty included an additional parameter to correct the effect resulted from the possibility that the power law exponent of a shear-thinning polymer might be different from that measured from a rheometer. Theoretically, Teeuw and Hesselink (1980) proved that C was related to power law exponent and geometric parameters for describing the constrictions and dilatations of a porous medium; C should be bigger for more tortuous

---

[3] Li, Z., Delshad, M., Lotfollahi, M., Koh, H., Luo, H., Chang, H., Zhang, J., Dempsey, P., Lucas-Clements, C., and Brennan, B., "Polymer Flooding of a Heavy Oil Reservoir with an Active Aquifer", SPE 169149, presented at the *SPE Improved Oil Recovery Symposium*, Tulsa, OK, USA, 12-16 April, 2014. In this work, Li implemented aquifer models, performed simulation studies and wrote the paper. Lotfollahi provided a residual oil reduction model. Koh provided experimental data. Delshad, Luo, Chang, Zhang, Dempsey, Lucas-Clements and Brennan made revisions.

[4] Li, Z., and Delshad, M., "Development of an Analytical Injectivity Model for Non-Newtonian Polymer Solutions", SPE 163672, SPE Journal, 19(03): 24-585, 2014. In this work, Li developed the semi-analytical injectivity model and conducted simulation studies. Delshad gave suggestions and made revisions.

porous media. Cannella *et al*. (1988) derived a similar correlation of C which was related to pore size distribution and the network structure of the porous medium; similarly C should be bigger for complex network. However, Cannella *et al*. found that C = 4.24 fitted well with all of their experimental data with different permeabilities (the shear rate coefficient defined by Cannella et al. is equal to $\sqrt{2}C$, which is 6 when C = 4.24). To explain this contradiction, they argued that polymer has a preference to flow through bigger pores without branching into small pores and the effect of pore channel connectivity was more important than the constrictions and dilatations of the porous medium. Wreath *et al.* (1990) summarized a list of literature results for shear rate correction factor, or the shear rate coefficient, C. Their correlation was adopted in UTCHEM as an option for modeling shear rate correction factor (IGAMC = 1) as discussed in Chapter 2. This correlation considers the possibility of deviation of power law exponent in porous media from that from a rheometer and suggests C should be bigger for porous media of lower permeability, lower porosity and higher oil saturation, which basically suggests more torturous flow channels. Recently, Koh (2015) showed that the fitted C equal to about 1.1 correlated well with his experimental data for HPAM solutions through porous media without oil. However, for biopolymer such as scleroglucan, a shear correction factor of 2~3 gave a better match. For oil recovery experiments, C equal to 4 correlated well with all of his experimental data. Koh suggested that the existence of oil increased the tortuosity of the polymer flow channels and led to a larger C. However, this didn't explain why he was able to reach a constant C for a wide range of core permeabilities (22 md to 7900 md). It was worth mentioning that the shear correction factor of 4.24 from Cannella et al. (1988) was for polymer flood experiments without oil being present. Therefore it would be interesting to understand why significantly smaller C values were found to fit Koh's experimental data. Lee (2015)

studied both scleroglucan and HPAM, and obtained similar C values varying from 1.2 to 2.3 in his coreflood experimental studies, except one case matched with C equal to 12 for polymer flooding in a Berea core using scleroglucan. In summary, many researchers suggested different C values varying for orders of magnitude in their study. It is still not clear how to find an exact correlation for C based on reservoir properties such as porosity, permeability, tortuosity, etc. without doing many tedious experimental studies. For limited coreflood studies, C values fitted for some representative permeabilities of the reservoir might not be enough to construct the correlation. It is thus important for us to figure out some guidelines for choosing C values in heterogeneous reservoirs without causing severe errors.

6.1.1 Simulation Study of Shear Correction Factor

In the latter simulation study, we used the Wreath's correlation for its flexibility to tune the value of C to reflect the effects of reservoir heterogeneity and the possible deviation of power law exponent in porous media from that from a rheometer. The C values based on the Wreath's correlation as shown in Fig. 6.1 were considered to be accurate. For a 2D cross section model with 2 layers as shown in Fig. 6.2, the upper layer has a permeability of 500 md and the lower layer has a permeability of 50 md. The injector is at the pressure constraint of 22.5 psi and the producer is at the pressure constraint of 14.7 psi. No cross flow is allowed between two layers. The reservoir and fluid properties are given in Table 6.1. The polymer viscosity is shown in Fig. 6.3. To estimate the shear rate correction factor for this case, both layers are assumed to be at residual oil saturation after injection of polymer solution for enough time. Then the shear rate correction factors for the upper layer permeability can be calculated from Eqs. [2.62]~ [2.64] and was estimated to be 11.6 while the shear rate correction factors for the

lower layer permeability was estimated to be 26.1. Three simulation studies were conducted: 1) Variable C based on the Wreath's correlation as shown in Fig. 6.1; 2) C = 11.6; 3) C = 26.1. As shown in Fig. 6.4, oil recoveries from case 1 of variable C and case 2 of C = 11.6 estimated from the high permeable zone match well while that from case 3 of C=26.1 from low permeable zone deviates slightly from case 1 and case 2. Fig. 6.5 shows that injection rates from case 1 of variable C and case 2 of C = 11.6 match well while that from case 3 of C=26.1 deviates significantly from case 1 and case 2. It is clear in this case that different C values result in slightly different oil recovery; however, C values may result in very different flow rates (if wells are at pressure constraint) or pressures (if wells were at rate constraint). So for this heterogeneous reservoir, it is important to characterize the C value in the high permeable zone which contributes to a larger portion of the flow rate compared with the low permeable zone.

Another simulation study is to show the impact of choosing different constant C values on coreflood simulation results. For a 1D coreflood model shown in Fig. 6.6, the injector is at the rate constraint of 0.0123 ft^3/d and the producer is at the pressure constraint of 14.7 psi. Three pore volumes of polymer solutions are injected. The core and fluid properties are given in Table 6.2. The coreflood simulations were tested with C equal to 1, 4, 10 and 30 which are typical shear correction factor values used for high permeability to low permeability rocks. As shown in Fig. 6.6, oil recoveries for C = 1, 4 and 10 are close to each other while oil recovery from the case of C=30 deviates for less than 6%. Fig. 6.7 shows the oil cuts for cases of different C values. Small C values give higher peaks of oil cut. However, the trends of the oil cuts are similar to each other. Fig. 6.8 shows the comparison of pressure drops across the core. It is clear in this plot that different C values result in significantly different pressure drops. At t = 3 PVs, the pressure drop for C = 30 is 44% less than that for C = 1. This sensitivity study shows that

in history matching of polymer coreflood experimental results, to accurately capture the C value, we need to match the pressure drop values. The cumulative oil recovery and oil cut are not sensitive to C for a wide range of typical C values.

6.1.2 Summary and Conclusions

- The variation of shear correction factor, C, in heterogeneous reservoir can be modeled using Wreath's correlation which considers the effects of permeability, porosity, saturation, and polymer type on shear correction factor.
- Wreath's correlation can be obtained by matching multiple sets of polymer coreflood experimental data. This is time-consuming and might be impossible for realistic studies.
- Simulation study shows that for a heterogeneous reservoir, it is important to characterize the C value in its high permeable zone which contributes to a larger portion of the flow rate compared with the low permeable zone.
- It is found that in coreflood simulation studies, pressure drop is sensitive to the selection of C values, while cumulative oil recovery or oil cut curves are insensitive to C values.

6.2 Impact of an Aquifer on Recovery Factor of a Heavy Oil Reservoir

Polymer flooding is a mature EOR technology for augmenting recovery of moderately viscous oil (Chang, 1978). Water soluble polymers are used to reduce water mobility and improve sweep efficiency (Stahl and Schulz, 1986; Sorbie, 1991). Widely accepted EOR screening criteria (Taber *et al*., 1997) suggest 150 cp as the upper limit of oil viscosity for economic application of polymer flooding. In recent years, oil price has maintained favorably high; meanwhile, newly introduced polymer manufacturing techniques improve polymer quality and keep polymer price relatively low.

Waterflooding of heavy oil reservoir leads to early water breakthrough and leaves considerable amount of remaining oil even at producing high water cuts. In contrast, polymer flooding reduces water cut and improves displacement sweep efficiency of heavy oil via lowering the mobility ratio and reducing viscous fingers (Levitt *et al*., 2011). The great potential of polymer flooding in heavy oil recovery attracts extensive interest from both academia and industry (Wassmuth *et al*., 2007; Wassmuth *et al*., 2009; Brooks *et al*., 2010; Al-Azri *et al*., 2010; Doorwar and Mohanty, 2011; Kamaraj *et al*., 2011; Levitt *et al*., 2011; Clemens *et al.,* 2012; Skauge *et al*., 2012; Fabbri *et al*., 2013; Delamaide *et al*., 2013). Claimed as "the first successful application of polymer flooding" in very viscous oil reservoir (1000-2500 cp), the Pelican Lake heavy oil field gives some exciting results — polymer flooding doubles the recovery factor of waterflooding and meanwhile reduces water cut although mobility ratio is still much higher than 1 (Delamaide *et al.,* 2013). Very few studies discuss polymer flooding of heavy oil fields with an underlying aquifer. The main concerns are polymer loss to the aquifer and low injectivity. A recent simulation study in South Oman identified polymer flooding as an economic EOR method compared to in-situ combustion and high-pressure steam injection for a medium-heavy oil reservoir (250-500 cp) with a very active bottom aquifer (Brooks *et al*., 2010; Al-Azri *et al*., 2010). Furthermore the application of thermal techniques in an offshore environment can prove expensive to install and technically challenging to preserve the heat where long reach horizontal wells extend from a single drill center. For offshore fields such as Bentley, chemical EOR methods therefore have the potential to be more attractive.

The Bentley field, currently owned and operated by Xcite Energy Resources Limited, is one of several heavy oil fields located in the United Kingdom Continental Shelf (about 160 km to the east of Lerwick, Shetland) (Brennan *et al*., 2011). This

offshore field contains about 900 MMstb sweet crude at low gravity (10-12 ^{o}API) and high viscosity (approximately 1500 cp). This sandstone reservoir has high permeability (average horizontal permeability is about 47 D) and medium reservoir temperature (37.5 ^{o}C), both favorable for polymer transport and stability. Sandpack experimental results (Li *et al.*, 2014) showed significant incremental oil recovery by polymer flooding over waterflooding and more than 90% of oil was recovered using polymer, ChemPam 8177.

The Bentley field is being drilled using horizontal drilling technology. High reservoir permeability and horizontal well technology also eliminate the concern of low polymer injectivity when using high-concentration polymers with large molecular size. Flow tests confirmed the existence of a large, active aquifer which should provide long-term pressure support during life-of-field production. Water analysis showed that ions of ferrous iron (Fe^{2+}) are present in the aquifer water which is harmful to most polymers and common pretreatment reduces iron ion down to less than one ppm. Besides, the brine contains Total Dissolved Solids (TDS) of approximately 50,000 ppm. However, with modern polymers available today, effective polymer viscosities can be achieved without either aerating or desalinating the water. Due to the high oil viscosity, water drive either with water injection or from the strong aquifer would have high unfavorable mobility ratios and, therefore, relatively poor lateral sweep efficiency. The aim of our study is to analyze the impact of the aquifer on heavy oil recovery efficiency by polymer flooding using UTCHEM.

6.2.1 Field Pilot Simulation Study

The objective is to set up a simple geometry numerical model (cube) for Bentley reservoir properties, fluid properties, and polymer properties measured in the lab to investigate polymer displacement process with different well configurations. The base

case well configuration is one horizontal well pair, i.e., one injector and one producer in the same vertical cross section.

Specific description of the model is given in Table 6.3. Relative permeability data used in the model are shown in Fig. 6.10 and fitting parameters are also given in Table 6.3. Viscosity data of polymer (ChemPam 8177) as a function of polymer concentration and shear rates were matched with polymer models as shown in Figs. 6.11 and 6.12**.** Polymer model parameters are listed in Table 6.4. Polymer rheology is assumed to be shear-thinning only because of the high reservoir permeability.

To model aquifer influxes, an analytical infinite aquifer was attached to the bottom of the reservoir model. Although the capability exists within UTCHEM to use a different salinity for the aquifer, it was assumed the aquifer water has the same salinity as the reservoir brine and the brine used for polymer injection.

To optimize reservoir development strategy, several scenarios were studied:

- Production scenarios
    - Primary oil production
    - Water injection
    - Polymer injection
    - Multiple producers with the same production rate
    - All cases have the producer in the 2nd layer
    - All cases with 2000 ft producer and 2000 ft injector
- Injection scenarios
    - Injector is located vertically below the producer.
    - Injector offsets the producer by 60 meters
    - Simulate injection well location at various heights above the WOC.
    - Multiple injectors with the same injection rate

6.2.1.1 Optimization of injection well depth

Oil recovery is very sensitive to how deep the injection well is placed. The optimum injection well location sweeps most of the oil column at the cost of polymer loss to the aquifer. Variables that affect the optimum injection well depth include aquifer strength, reservoir permeability, production and injection rates, oil and polymer prices, etc. Here, we assume constant injection rate for the same period of time so that the amount of injected polymer is the same. Besides, reservoir permeability and production rate are given. Then the optimum injection well location can be determined by the maximum oil recovery at a given aquifer strength. The basic simplification of the aquifer is to assume that it could be mimicked with an infinite aquifer. The semi-analytical aquifer model by Vinsome and Westerveld can be used as a good approximation for the infinite aquifer. Nine cases for one well pair scenario were simulated with (1) extended primary production which gives similar performance as waterflooding because of the strong aquifer influxes and (2) polymer floods. Table 6.5 is a summary of nine simulation cases. Fig. 6.13 gives the incremental oil recovery (percentage) vs. injector location above the water-oil contact (WOC) for different polymer flooding cases when using the infinite aquifer model. Fig. 6.14 gives the cumulative oil recovery for primary production, the optimized polymer flooding (Case # 1p1i00, injector at WOC) and the polymer flooding case with injector at 35 ft above the WOC. These results show that polymer flooding can increase the oil production by about 48% over extended primary recovery. The optimum well location is found to be just above the water-oil contact. However, little information is known about the aquifer permeability or strength. We assumed a permeability of 25 D for aquifer permeability. More simulations are underway to investigate the impact of aquifer permeability and its strength on polymer performance. Well tests show that during the initial production of the reservoir, no

significant pressure drawdown was observed. As a sensitivity study, it was assumed that two pressure-constrained injection wells in the bottom aquifer can be used to mimic the maximum aquifer strength at which the aquifer pressure remains constant. Fig. 6.15 shows the cross section of the model with two pressure-constraint injection wells. Fig. 6.16 gives the incremental oil recovery vs. injector location above the water-oil contact for different polymer flooding cases when using pressure-stabilized aquifer. In these simulations, it was found that the best location for the injector is 10 ft above the WOC. Although incremental oil recovery decreases compared with those cases with an infinite aquifer, polymer flooding still increases the oil production by about 37% over extended primary recovery for the optimum injection well location. Typical distributions of oil saturation in several horizontal and vertical cross-sections after polymer flooding are shown in Figs. 6.17 through 6.20. The swept area is tent-like, which is large near the bottom injection well and shrinks quickly to the top production well. Fig. 6.20 shows that the swept area of extended primary production is increased when polymer is injected.

6.2.1.2 One producer to one injector offset

The basic premise is to improve sweep efficiency by offsetting the injection well. In this case, the injector, which is just above the WOC, offsets the producer in the x-direction for 60 meters. However, if we examine the results shown in Fig. 6.21, oil recovery decreases from 2.47 MM bbls to 2.09 MM bbls (note: extended primary production gives cumulative oil recovery of 1.67 MM bbls). The effect of polymer flooding in this well configuration is not obvious. This result may be explained by the unfavorable mobility ratio and short production time.

6.2.1.3 Delay polymer flooding

Five more runs were performed to investigate the impact of delaying polymer injection. The base case was run for 35 years (1 producer to 1 injector model, polymer injection commencing at 5% water cut, and injector just above the WOC). For comparison purposes, an extended primary production and waterflood simulations were conducted without polymer injection. A sensitivity study was conducted to compare the recovery when polymer injection commenced, corresponding to 50% and 90% water cut. Fig. 6.22 shows that polymer flood starting at 5% water cut gives the best performance (oil recovery is about 4.27 MM bbls) and waterflooding gives the lowest oil recovery (3.26 MM bbls). The incremental oil recovery is about 31.1%. During primary production, water breaks through at around 140 days and water cut increases abruptly from 5% (at around 145 days) to 50% (at around 160 days). The difference is negligible between 5% water cut and 50% water cut for polymer injection (in Fig. 6.22, the black curve and the red curve overlap each other). Water cut for primary recovery reaches 0.9 in 720 days. Cumulative oil recovery from the 90% water cut case catches up with other cases in 2 to 3 years (Fig. 6.22). The final difference is only about 0.05 MM bbls. The incremental recovery from polymer flood is therefore relatively independent of the time at which it commences. This is very useful for planning purposes as it allows time to develop and implement the necessary polymer facilities and it enables well performance to be monitored prior to polymer flood commencing.

6.2.1.4 Number of wells

In realistic field conditions, we have several producers and injectors with multiple laterals. One key optimization parameter is the number of wells. Initially, five simulations were set up by adding producers to the box model with well spacing of 80 meters. There is no injection in any of these cases. All of the cases were simulated for

3080 days. The results are shown in Fig. 6.23. The oil recovery increases linearly as more producers are added with no injection. This implies that interference is negligible among those producers when the well spacing is 80 meters. The unfavorable mobility ratio of oil to brine constrains the oil production capability of a single well. In order to optimize the number of injection wells, a sensitivity study was conducted. Three cases were compared: a 3 to 1, a 3 to 2 and a 3 to 3 (producer to injector). The 3 to 1 well configuration is shown below and the exact locations of these well are shown in Fig. 6.24a.

3 Producers and 1 Injector Case

P P P

I

Producer spacing = 6 grid blocks = 120 meters

The 3 to 2 well configuration is shown below and the exact locations of these wells are shown in Fig. 6.24b.

3 Producers and 2 Injectors Case

P P P

I I

Producer spacing = 6 grid blocks = 120 meters

Injector spacing = 6 grid blocks = 120 meters

The 3 to 3 well configuration is shown below and the exact locations of these wells are shown in Fig. 6.24c. Injection wells are all located just above the aquifer.

3 Producers and 3 Injectors Case

P P P

I I I

Producer spacing = 6 grid blocks = 120 meters

Injector spacing = 6 grid blocks = 120 meters

Simulation results are shown in Fig. 6.25: after over 8 years of polymer flooding, the 3 to 1 case produces the least amount of oil (5.24 MM bbls), while the 3 to 3 case produces almost the same amount of oil (6.63 MM bbls) as that with the 3 to 2 case (6.56 MM bbls). The difference in oil recoveries between these two cases is large at the beginning (0.87 MM bbls) but decreases as time proceeds. Considering the cost of drilling, especially in an offshore environment, it would appear economical to use fewer injection wells than production wells.

6.2.1.5 Injector orientation

One more simulation was run to investigate the sensitivity of oil recovery to injector orientation. The run (Case # 3p3ivt) is for the 3 to 3 case. Injection wells were placed perpendicular to production wells as shown in Fig. 6.26. As shown in Fig. 6.27, after 8 years of polymer flooding, Case 3p3ivt produces less oil (5.58 MM bbls) compared to Case 3p3i (6.63 MM bbls). However, after extending the simulation time from 8.43 yrs (3080 days) to 35 years, the cumulative oil recovery of Case 3p3ivt surpasses that of Case 3p3i. This is because more reservoir volume is swept in Case 3p3ivt.

6.2.2 Summary and Conclusions

- For the box model with the semi-analytical infinite aquifer, the optimum injection depth is just above the WOC. Polymer flood incremental recovery over water flood is about 48%, which is substantial. When two pressure-constraint injectors are used, the optimum injection well location is 10 ft above the WOC.
- The delay in polymer flooding only slightly decreases the final oil recovery which is useful as it allows time to develop and implement polymer facilities and enables monitoring of well performance prior to commencement of waterflood. However, further simulations are needed to study the viscoelastic effect of high concentration of large molecular weight polymers.
- Oil recovery increases linearly with the number of producers for primary production (no injection). This could help in deciding when to add an injector or producer.
- Three producer to two injector well arrangement produces almost the same amount of oil (6.56 MM bbls) as the 3 producer to 3 injector case (6.63 MM bbls) in 8 years. Different orientations of injection wells may improve cumulative oil recovery by enlarging the swept volume. More simulations are required to optimize the well orientation.
- An important issue in heavy oil recovery is the viscous fingering effect, which however is not captured in our simulations. Adverse viscosity ratios during the waterflooding in viscous oil reservoirs lead to viscous fingers and render the displacing process less effective. High water cut may be reached at very early times with large amounts of oil left in the reservoir. Polymer flooding in heavy oil reservoirs can reduce fingering and stabilize the displacement process. For

heavy oil recovery, due to the improve mobility ratio, concentrated polymer flood can improve both volumetric and displacement sweep efficiencies by lowering the oil saturation below waterflood residual oil saturations. Very fine grid models can be used to investigate the importance of fingers in coreflood simulations. In field scale simulations, results from coreflood studies need to be upscaled in sophisticated ways to capture the fingering effect (Doorwar and Mohanty, 2011).

6.3 MODELING POLYMER INJECTIVITY

This section follows the derivations and discussion in Chapter 4. The polymer viscosity model in UTCHEM was used to model polymer injectivity in 1D coreflood. Semi-analytical polymer injectivity model was applied to model polymer injectivity in the field.

6.3.1 Polymer Injectivity in 1D Coreflood

Experimental data (Yerramilli *et al*., 2013) were used to simulate polymer injectivity in 1D coreflood and also validate the Carreau model (shear-thinning part of the UVM model) and its implementation in UTCHEM. Table 6.6 summarizes the experimental results. Injectivity relative to water (I_p/I_w) is defined as the ratio of pressure drop in waterflood to that in polymer flood after 10 pore volumes of fluid injection. Table 6.7 gives the simulation input parameters for 1D coreflood and polymer properties. Shear rate coefficient (C) is set to 2.5 (Stavland *et al*., 2013). As shown in Fig. 6.28, UTCHEM gave a very close match of the experimental results without tuning additional model parameters.

The experimental data and simulation results showed that polymer injectivity drastically decreases as polymer concentration increases. In the experiment, mechanical

degradation of polymer is not observed and loss of polymer injectivity is mainly caused by high polymer viscosity and permeability reduction effect. Polymer coreflood experiments and simulation studies provide input parameters for setting up field-scale models with which well injectivity and economics of polymer flood can be further studied.

6.3.2 Polymer Injectivity in Field Cases

Field case study is important for showing the importance of capturing polymer rheology in the near wellbore region and its effect on polymer injectivity. The first field case we studied is shown in in Fig. 6.29. Table 6.8 gives a basic description of the field and fluid properties. This field case has a fine-grid simulation model and an upscaled counterpart. For the fine-grid simulation, we use 43×47×45 gridblocks; for the coarse-grid simulation, we use 11×12×19 gridblocks. Considering the grid block size, the maximum timestep estimated from the pore volume of the grid block from the coarse grid model would be about (43×47×45)/(11×12×19) ≈ 36 times larger than that from the fine grid model. So if a coarse grid model can be successfully upscaled from the fine grid model for this polymer flood case, the computational efficiency will be improved significantly. The simulation process starts with a waterflood for 5 PVs followed by a high concentration polymer flood (0.2 wt%, 0.3 PV), then a low concentration polymer flood (0.115 wt%, 1 PV) and finally a post waterflood (1 PV). One of the 10 injectors (the one pointed in Fig. 6.29) is chosen for presenting the analysis. In Fig. 6.30, we compare the results of a fine-grid simulation with its up-scaled coarse model. The effective radius method (Eq. [2.64]) was used to match the wellbore pressure of the coarse-grid simulation with that of the fine one, which is shown as the curve "R_{weff} = 10 ft". Note R_{weff} matched here is much larger than the well radius. It is shown that before

polymer flood starts, the wellbore pressure is the same for fine-grid and coarse-grid simulation cases because no injectivity correction is needed for waterflood. However, after polymer flood starts, the wellbore pressure of the one using R_{weff} = 10 ft deviates widely from that of the coarse one without injectivity modification. Once we activate the analytical model option with the coarse grid, the analytical model greatly improves the calculated polymer injectivity. The area equivalent radius method (Eq. [4.18]) still overestimates the shear rate as shown in the verification cases in Chapter 4 but gives a fairly good estimation of the polymer injectivity in this case.

A normal 5-spot pilot study was used to show the impact of the analytical model on prediction of polymer flood performance. Table 6.9 gives basic properties of the reservoir and the polymer rheology. For this case, we use 21×18×75 gridblocks. All wells are operated on pressure-constraint. Waterflood is conducted for 240 days and the polymer flood continues until 390 days. Fig. 6.31 shows the reservoir pressure at 300 days. Figure 6.32 shows aqueous-phase viscosity change with time near injector No. 1 and Fig. 6.33 gives the viscosity near the producer. Modified viscosities are compared with original values. Obviously, modification with the analytical model gives a much lower aqueous-phase viscosity near wellbore because of more accurately calculated higher shear rates. As shown in Fig. 6.34, the correction in viscosity causes very different injection rates during polymer flood. Polymer injectivity increases where more water is injected causing a quick pressure build up (Fig. 6.35) when the viscosity correction is considered. More oil is recovered since more fluid is injected with an increase in sweep efficiency (Fig. 6.36).

6.3.3 Summary and Conclusions

- 1D polymer coreflood simulations were conducted to match experimental data. The close match between simulation results and experimental data validated the Carreau model and its implementation in UTCHEM. Coreflood experiments and simulation studies are necessary because they provide input parameters for field-scale polymer flood simulations.
- The semi-analytical injectivity model was successfully validated using a fine-grid field simulation and its up-scaled counterpart.
- The impact of the correction using the proposed analytical model in field-scale simulations is demonstrated by closely examining polymer solution viscosity of the wellblock, well injection rates, and average reservoir pressure.
- Based on this study, it is believed that grid effect needs to be considered for reservoir simulation of polymer flood. Our analytical model helps to eliminate the grid effect and thus gives a more accurate polymer injectivity.

6.4 Impact of Fracture Propagation on Polymer Flood Performance

In this section, we used UTCHEM coupled with a fracture model to simulate fracture propagation during polymer flooding. This coupled model was firstly compared with UTWID (Sharma *et al.*, 2009). Then we simulated fracture propagation process in an inverted 5-spot during injection of a viscoelastic polymer solution.

6.4.1 UTCHEM and UTWID Comparison

The University of Texas Well Injectivity Decline simulator (UTWID) is a semi-analytical single-injection-well numerical simulator. The simulator is designed to predict fracturing and well injectivity due to the effects of particle plugging, thermal stresses,

pore pressure changes, polymer injection, etc. (Gadde et al.,2001; Suri and Sharma, 2009) Assumptions include:

- Fracture geometry is given by the PKN model.
- A fracture propagation criterion by Perkins *et al.* (1985) is used to determine fracture length.
- Fluid leak-off from the fracture is assumed to be uniform and overall leak-off rate equal to total injection rate.
- Displacement is assumed piston-like.
- Polymer rheology follows the power law model.
- Flow resistance due to polymer injection is calculated analytically using a radial flow assumption. The radius is approximated using one half of the sum of the major axis and the minor axis of an elliptical flow front.

  Details of UTWID can be found in the User Guide (Sharma *et al.,* 2009).

To compare UTCHEM coupled with fracture model against UTWID results, an inverted 5-spot was set up. A brief description of the homogeneous and isotropic reservoir model is shown in Table 6.10. The relative permeability curves are fitting using the Corey-Type relative permeability model as shown in Table 6.11. Additional rock/geomechanical properties are required for fracture model as shown in Table 6.12. Four producers located at the corners produce at constant pressure of 3000 psi. One injector located at the center injects 1500 ppm polymer solutions at 356 bbl/day (2000 ft3/day). The polymer rheology is shown in Fig. 6.37, with matched parameters given in Table 6.13. For UTCHEM, Meter's equation was used to match to experimental data and for UTWID, the power law model was used. As shown in Fig. 6.38, it takes about 25 days for fracture to initiate in the UTCHEM simulation while in the UTWID model, fracture initiates from the beginning. In the UTCHEM, it is shown that fracture grows

fast at the beginning from zero to tens of feet. Possible reason for this sudden change could be the pseudo-static approach we use to model fracture initiation process when the radial flow pattern of no fracture at the injection well changes to an elliptical flow pattern. Similar observations were shown in the modeling results by Seright et al. (2008) and also results by UTWID that will be discussed later. Fracture half-length predicted from UTCHEM is longer than UTWID in the late stage after fracture initiates. In the inverted 5-spot UTCHEM model, four production wells are used to deplete the reservoir pressure. However, in the UTWID model, only one single injection well is model and pressure builds up when fluids are injected into the reservoir. If the pressure depletion at the boundary is approximated using large drainage radii, better match of the results are observed. Considering the differences between the UTCHEM fracturing modeling (KGD fracture model, coupled reservoir and fracture, numerical reservoir simulation) and the UTWID model (PKN fracture model, single injection well model, semi-analytical solution), it is no surprise to see the misfit between UTCHEM and UTWID. As shown in Fig. 6.39, when polymer of higher concentration (3000 ppm) is used, an earlier fracture initiation is observed. Fig. 6.40 shows that a lower polymer viscosity in the UTWID model also predicts a delay of fracture initiation and a sudden fracture growth, although the fracture length is much short. This can be explained by a significant difference between PKN model and KGD model: the PKN model is not based on the Barenblatt theory and the flow resistance in the fracture determined by the PKN model is thus smaller than the KGD model (Geertsma and de Klerk, 1969). Therefore, it requires lower pressure for the PKN model to initiate a fracture or propagate a fracture in the early stage compared to the KGD model. The KGD model is more accurate than the PKN model for predicting fracture initiation or fracture propagation in the early stage.

6.4.2 Fracture Propagation during Injection of Viscoelastic Polymer

Rheological data of HPAM from Chauveteau (1981) are matched using the UVM model as shown in Fig. 6.41. The values of fitting parameters are given in Table 6.14. Considering that polymer rheology is different in porous media than in fracture, the shear-thinning regimes of the HPAM rheological data from Chauveteau (1981) are matched with the modified power law model (Eq. [B-13], [B-14] in Appendix B) as shown in Fig. 6.42. The fitting parameters are given in columns 2 and 3 of Table 6.14. The dependence of the power law parameters on polymer concentration were modeled with Eq. [5.1] and [5.2], and the fitting parameters are given in Table 6.15. Power law parameters correlated using the fitting parameters are given in columns 4 and 5 in Table 6.14.

An inverted 5-spot is studied as an example to show the capability of UTCHEM implicitly coupled with the fracture model. This same reservoir geometry and reservoir/fluid properties as shown in Section 6.4.1 were adopted for study here and the parameters are given in Tables 6.10~6.12. Four producers located at the corners produce at constant pressure of 3000 psi. One injector located at the center injects 1500 ppm polymer solutions at 356 bbl/day (2000 ft^3/day) for half pore volume and then switches to 500 ppm polymer solutions at 250 bbl/day (1403 ft^3/day) for another 0.5 PV.

Fig. 6.43 shows the polymer concentration distribution after injecting 90 days of 1500 ppm polymer solutions. The length of the fracture is marked in black crossing the injector in the center. If the fracture didn't exist, the front of the injected polymer solutions would have a circular front. However, fracture growth from the injector diverts injected polymer distribution so that the front of the polymer solutions becomes elliptical.

Figs. 6.44~6.46 show fracture half-length vs. injection time compared against some other important variables such as oil cut, injectivity, and wellbore pressure of the

injector. It is clear that there is no oscillation during the simulation process, which owes to our implicit scheme. After injecting for 180 days (0.5 PV), the injection rate decreases from 356 bbl/day to 200 bbl/day, and polymer concentration also decreases from 1500 ppm to 500 ppm, which causes wellbore pressure to decrease below minimum horizontal stress and the fracture closes. Fig. 6.44 shows that immediately after water breaks through the producers, the fracture half-length increases suddenly for several feet and the rate of fracture growth gradually increases afterwards. This is because after the water breaks through, the total mobility of the fluid at the producer decreases until it reaches a minimum. This effect causes an increase in pressure at the injector in order to maintain its injection rate. Fig. 6.45 shows that after fractures initiates, the injectivity maintains approximately constant until fracture closes. After switching to lower concentration and lower injection rate, wellbore injectivity gradually recovers. Fig. 6.46 shows the wellbore pressure.

Fig. 6.47 and Fig. 6.48 show the results assuming polymer is shear-thinning only using Carreu model compared with those from the UVM model. Carreau model uses most of the UVM model parameters except for $AP_{11}=0$ and $AP_{22}=0$ (no shear-thickening effect). The results in Fig. 6.47 show that when there is no shear-thickening effect, fracture initiates later after more than one month. The length of the fracture is also shorter. Fig. 6.48 shows that only after injecting for some time, injection of shear-thinning polymer will increases the wellbore pressure to the fracture initiation pressure and after fracture initiates, wellbore injectivity remains approximately constant and is almost equal to the result from the shear-thickening case. This implies that after fracture initiation, shear rate decreases and polymer solution viscosity is not much affected by the shear-thickening effect. Polymer rheology is only shear-thickening near the wellbore. Similar results were observed in Ma's simulation studies using a modified version of

CFRAC (Ma, 2015). Ma's simulation results showed that "fracture initiation occurred much earlier" for cases with shear-thickening polymers and after fracture initiation, polymer injectivities were almost the same for shear-thinning and shear-thickening polymers. After injecting after 0.5 PV, polymer concentration decreases from 1500 ppm to 500 ppm. When polymer concentration is small, shear-thickening effect is not obvious. That's why even after fracture is closed, wellbore pressure seems not affected by polymer rheology.

6.4.3 Summary and Conclusions

- UTCHEM was implicitly coupled with a fracturing model to study the impact of fracture growth during chemical flood processes.
- The coupled model was compared with the semi-analytical, single-injection-well simulator, UTWID. The results from UTCHEM and UTWID show qualitative agreement despite their different fracture models, assumptions and approaches.
- The coupled simulator can be used to optimize polymer flood concerning polymer injectivity, impact of fracture growth on sweep efficiency, flow out of zone, etc.
- The preliminary simulation results show how fracture growth is affected by total mobility of multiphase fluid flow. It also shows the impact of polymer rheology on fracture initiation and fracture growth.
- Once fracture is initiated, pressure is reduced in the wellbore which significantly enhances polymer injectivity.
- The semi-analytical polymer injectivity model helps to capture polymer rheology in the near-wellbore area without the need to use fine-size grids.

- Shear-thickening causes earlier fracture initiation.
- After fracture is initiated, wellbore pressures or polymer injectivities are almost the same for shear-thinning and shear-thickening polymers. This implies that shear-thickening effect is only important for near wellbore, and after fracture initiation shear rate decreases and polymer solution viscosity is not much affected by the shear-thickening.

Length, L, ft	7.8
Width, W, ft	0.04
Upper and lower layer thickness, ft	0.19029
Upper and lower layer porosity	0.3
Initial water saturation for upper and lower layers	0.3
Upper layer permeability, k_1, md	500
Lower layer permeability, k_2, md	50
Endpoint water/oil relative permeability	0.4, 0.8
Corey exponents for water and oil phases	2, 2
Residual water and oil saturations	0.3, 0.33
Displaced fluid viscosity (Brine), cp	1
Displacing fluid viscosity (Polymer), cp	8
Polymer concentration, wt%	0.1
AP1, AP2, AP3	46.9, 47, 2001.4
GAMMAC, GAMHF, POWN, GAMHF2	Variable, 300, 1.52, 0
Total Injection Rate, ft^3/d	0.16951

Table 6.1: Reservoir and fluid properties for a 2D cross-sectional model.

Length, L, ft	0.744
Cross area, A, ft^2	0.0121
Porosity, ϕ	0.219
Permeability, k, md	720
Initial water saturation, S_{wi}	0.59
Endpoint water/oil relative permeability	0.3, 0.6
Corey exponents for water and oil phases	2, 2
Residual water/oil saturations	0.3, 0.33
Oil viscosity, cp	7
Brine viscosity, cp	0.678
Polymer concentration, wt%	0.15
AP1, AP2, AP3	12.54, 41, 715
GAMMAC, GAMHF, POWN, GAMHF2	Variable, 450, 1.8, 0
BRK, CRK, RKCUT	100, 0.13, 10
AD41, AD42, B4D	0.97, 0.5, 100
EPHI4	1
Total Injection Rate, ft^3/d	0.0123

Table 6.2: Core and fluid properties for 1D polymer flooding model.

Geometry	Box model with 58 x 47 x 29 gridblocks
Grid cell size in the x-, y-, z- direction, ft	65.6, 65.6, 5
Reservoir top, ft	3600
Oil column, ft	130
Water column, ft	400
OWC, ft	3730
Oil zone permeability, darcy	47
Aquifer permeability, darcy	25
Kv/Kh ratio	0.6
Permeability of infinite aquifer, darcy	1.2
Oil viscosity, cp	1518
Water viscosity, cp	0.74
Endpoint water/oil relative permeability	1, 0.3
Corey exponents for water and oil phases	2.0, 3.0
Residual water and oil saturations	0.35, 0.09
Formation volume factors: Bw, Bo	1.002, 1.06128
Production rate, bbl/d	2500 for first 160 d and 5000 afterwards

Table 6.3: Bentley reservoir model description and fluid properties.

AP1, AP2, AP3	19, 60, 1800
GAMMAC, GAMHF, POWN, GAMHF2	4, 9670, 1.4, -25.23
BRK, CRK, RKCUT	100, 0, 10
AD41, AD42, B4D	1.4, 0.5, 100
EPHI4	1
Polymer Concentration, wt%	0.3

Table 6.4: Polymer properties for ChemPam 8177.

Case #	Injector Location above WOC (ft)	Inj./Prod. Rate before 160 Day (bbl/d)	Inj./Prod. Rate after 160 Day (bbl/d)
Primary (PP)	0 (At WOC)	0, 2500	0, 5000
1p1i00(PF at WOC)	0 (At WOC)	0, 2500	5000, 5000
1p1i05(PF at 5ft)	5	0, 2500	5000, 5000
1p1i10(PF at 10ft)	10	0, 2500	5000, 5000
1p1i15(PF at 15ft)	15	0, 2500	5000, 5000
1p1i20(PF at 20ft)	20	0, 2500	5000, 5000
1p1i25(PF at 25ft)	25	0, 2500	5000, 5000
1p1i30(PF at 30ft)	30	0, 2500	5000, 5000
1p1i35(PF at 35ft)	35	0, 2500	5000, 5000

Table 6.5: Summary of simulation cases for injector depth optimization.

Exp.	C_p (ppm)	C_{NaCl} (g/cm^3)	k (md)	ϕ	μ_P at 1 s^{-1} (cp)	R_k	Ads. (μg/g)	λ_1	n_1	I_p/I_w
1	125	0.02	2450	0.23	-	1.02	38.2	0	1	0.83
2	250	0.02	2314	0.21	-	1.039	57.1	0.045	0.924	0.74
3	500	0.02	2499	0.22	1.86	1.06	88.4	0.094	0.854	0.59
4	1000	0.02	2659	0.22	3.27	1.079	114	0.097	0.843	0.33
5	2000	0.02	2450	0.21	6.41	1.098	132.9	0.111	0.761	0.22
6	3000	0.02	2272	0.22	11.73	1.112	158.5	0.133	0.695	0.11
7	4000	0.02	-	-	21.22	-	-	0.39	0.64	-
8	5000	0.02	2014	0.21	34.94	1.12	166.4	0.197	0.661	0.05

Table 6.6: Polymer coreflood experimental data from Yerramilli et al. (2013); λ_1 and n_1 are given by non-linear regression analysis of the experimental data.

Length, L, cm	17
Cross diameter, cm	3.8
Porosity, ϕ	As given in Table 6.6
Permeability, k, md	As given in Table 6.6
Initial water saturation, S_{wi}	1
Anion concentration, meq/ml	0.342
Brine viscosity, cp	1.0
Polymer concentration, ppm	As given in Table 6.6
AP1, AP2, AP3	1.266 1.5545, 1.
GAMMAC	10
BRK, CRK, RKCUT	15.147, 0.0461, 10
BETAP, SSLOPE, CSE1	0, -2.329, 0.01
AD41, AD42, B4D	3.363, 0, 19.615
λ_1, n_1	As given in Table 6.6
Total Injection Rate, cc/min	1.0

Table 6.7: Reservoir and polymer properties for coreflood simulations.

Reservoir dimensions in x, y, z directions, ft	2100, 2400, 37
Rock compressibility, psi^{-1}	0.000008
Permeability, md	Variable (10^{-5}~8970.8), anisotropic
Porosity	Variable (0.01~0.33)
Initial pressure at reference depth, psi	550
Reference depth, ft	1965.8
Initial water saturation	0.2
Residual water saturation	Gridblock dependent
Anion concentration, meq/ml	0.0513
Brine viscosity, cp	0.37
Oil viscosity, cp	3.4
Water compressibility, psi^{-1}	0.000003
Oil compressibility, psi^{-1}	0.00001
AP1, AP2, AP3	45, 625, 1000
BETAP, CSE1, SSLOPE	1, 0.01, -0.377
GAMMAC, GAMHF, POWN, GAMHF2	4, 30, 1.8, 0

Table 6.8: Reservoir and polymer properties for field case 1.

Reservoir dimensions in x, y, z directions, ft	210, 150, 180
Rock Compressibility, psi^{-1}	0.000008
Permeability, md	Variable (10^{-5}~5889.5), anisotropic
Porosity	Variable (0.01~0.31)
Initial pressure at reference depth, psi	1304
Reference depth, ft	2457
Anion concentration, meq/ml	0.1323
Brine viscosity, cp	0.48
Oil viscosity, cp	17
Water compressibility, psi^{-1}	0.0000027
Oil compressibility, psi^{-1}	0.00005
AP1, AP2, AP3	150, 150, 850
BETAP, CSE1, SSLOPE	1, 0.01, -0.377
GAMMAC, GAMHF, POWN, GAMHF2	15, 5, 1.7, 0

Table 6.9: Reservoir and polymer properties for field case 2.

Reservoir dimensions in x, y, z directions, ft	300, 300, 40
Number of grid blocks	31 × 31 × 1
Initial reservoir pressure, psi	3000
Initial water saturation	0.3
Porosity	0.2
Permeabilities in x, y, z directions, md	100, 100, 10
Water viscosity, cp	0.798
Oil viscosity, cp	10
Rock compressibility, psi^{-1}	$3.3x10^{-6}$
Water compressibility, psi^{-1}	$3x10^{-6}$
Oil compressibility, psi^{-1}	$1x10^{-5}$
Well radius, ft	0.25

Table 6.10: Reservoir model description for comparison of UTCHEM with UTWID.

Endpoint relative permeability to water, k_{rw}^{o}	0.7
Endpoint relative permeability to oil, k_{ro}^{o}	0.3
Endpoint exponent to water, n_w	2.0
Endpoint exponent to oil, n_o	2.0
Residual water saturation, S_{wr}	0.3
Residual oil saturation, Sor	0.3

Table 6.11: Corey-type oil/water relative permeability parameters for comparison of UTCHEM with UTWID.

Initial maximum horizontal stress, psi	4500
Initial minimum horizontal stress, psi	4000
Tensile stress, psi	0
Biot's constant	0.9
Poisson's ratio	0.3
Young's modulus, psi	3950000
Critical stress-intensity factor, KIC, psi	500
Initial fracture half length, ft	1
Infinite dimensionless fracture conductivity	10

Table 6.12: Fracture model input parameters for comparison of UTCHEM with UTWID.

AP1, AP2, AP3	29.6, 29.6, 1262.511
BETAP, CSE1, SSLOPE	1, 0.01, -0.42929
GAMMAC, GAMHF, POWN, GAMHF2	24, 4381.87, 1.4, -24.2037
ISHEAR	2
a1, a2, a3	27, 0, 0
b1, b2	0.25, 0
Power law exponent, n	0.8

Table 6.13: Polymer rheology input parameters for comparison of UTCHEM with UTWID.

AP1, AP2, AP3	35, 435, 1055
BETAV1, BETAV2, EXPN1	0.0192, 18.522, 0.78
TETAV, TAU0, TAU1	0.01, 0.2992, 0.008905
EXPN2, AP11, AP22	3.5, 2.7406, 17.116
a1, a2, a3	1.1068, 685.6407, 1.8091
b1, b2	1.6686, 0.8489

Table 6.14: UVM model and power law model input parameters for HPAM data (Chauveteau, 1981).

Polymer Conc., wt%	Fitted K ($cp.s^{n-1}$)	Fitted n	Modeled K ($cp.s^{n-1}$)	Modeled n
0.136	19.676	0.768	19.666	0.765
0.068	6.329	0.850	6.403	0.854
0.034	2.754	0.912	2.618	0.914

Table 6.15: Summary of parameters for correlating data (Chauveteau, 1981) with the power law model.

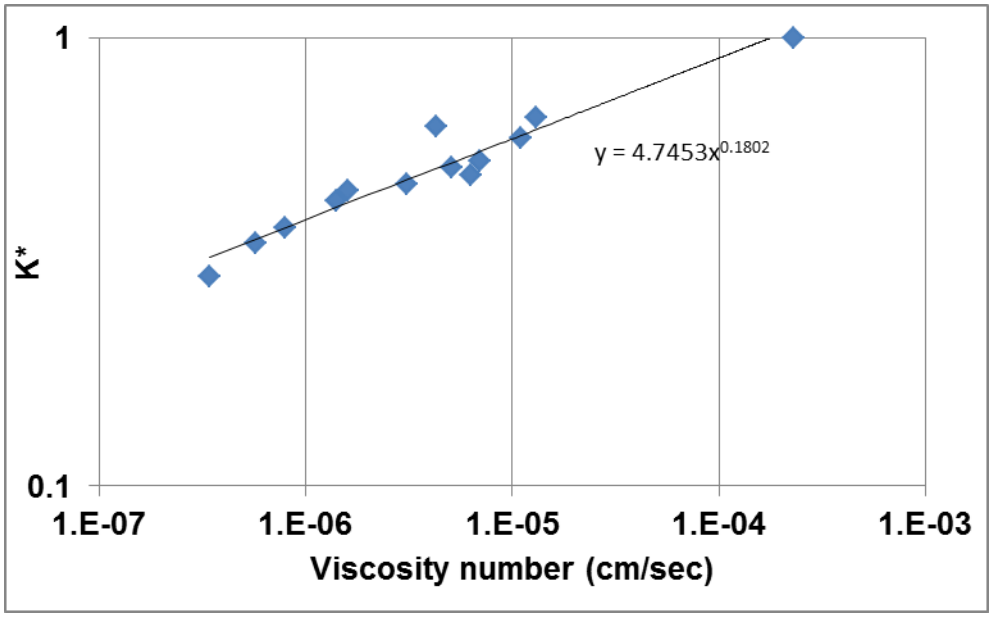

Figure 6.1: Wreath's correlation for polymer flood experiments (n=0.48).

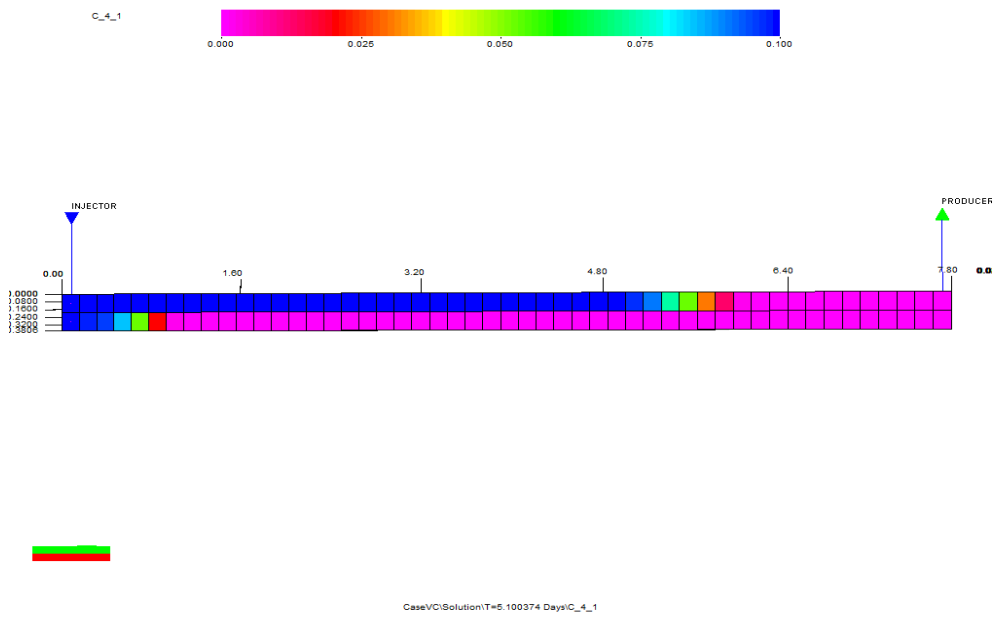

Figure 6.2: Polymer concentration distribution at T=5.1 days in a 2D cross section model.

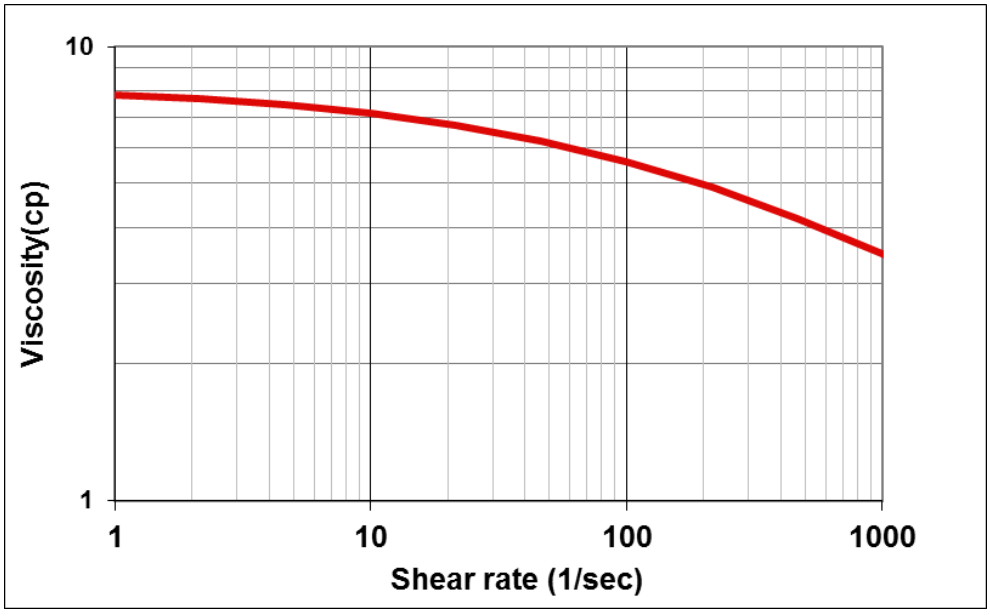

Figure 6.3: Polymer viscosity vs. shear rate.

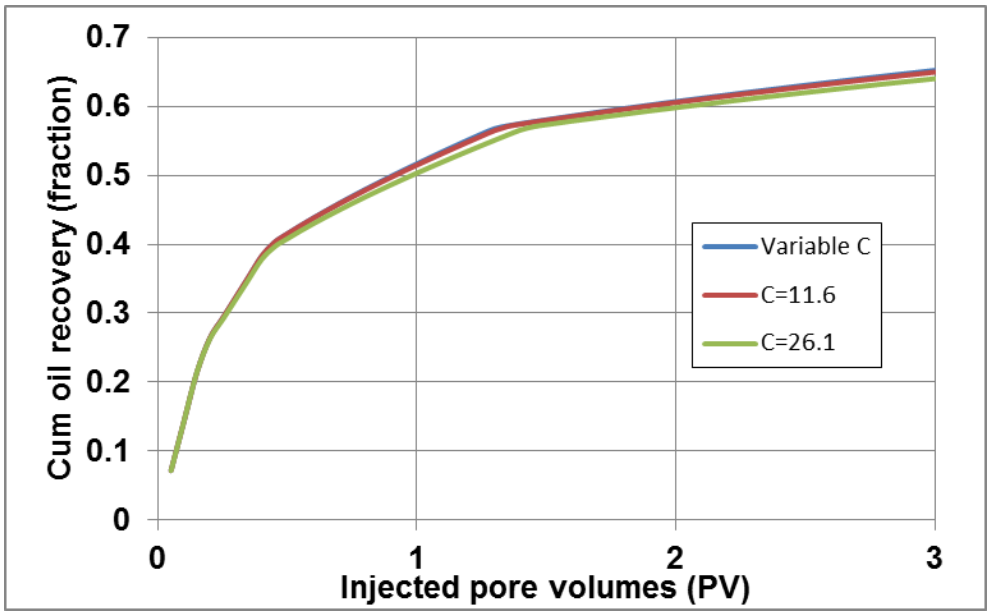

Figure 6.4: Cumulative oil recovery vs. injected pore volumes for variable shear correction factor using Wreath's correlation, constant C=11.6 from high permeability zone, and constant C=26.1 from low permeability zone.

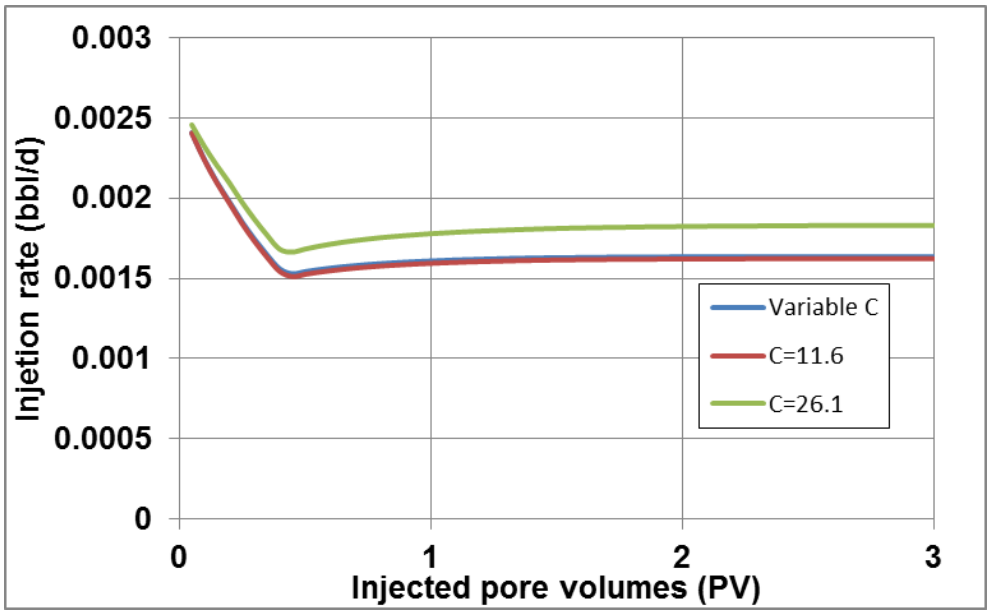

Figure 6.5: Injection rate vs. injected pore volumes for variable shear correction factor using Wreath's correlation, constant C=11.6 from high permeability zone, and constant C=26.1 from low permeability zone.

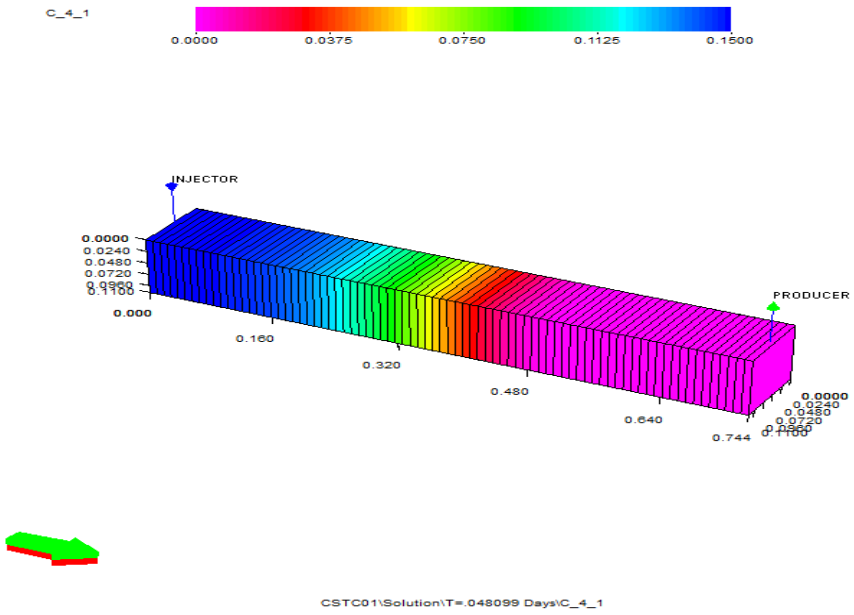

Figure 6.6: polymer concentration distribution along the core at T=0.48 day.

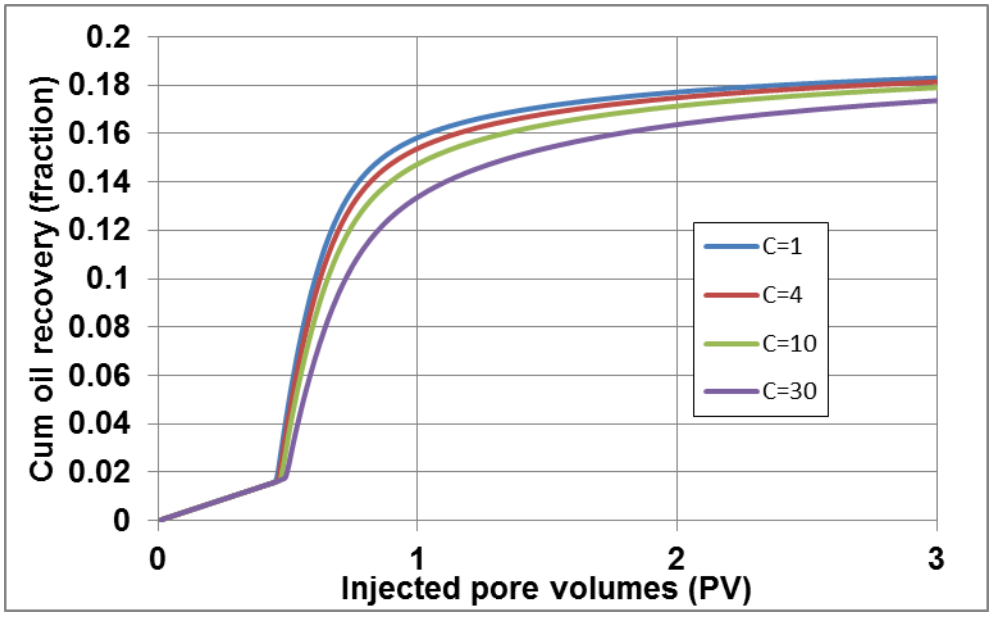

Figure 6.7: Cumulative oil recovery vs. injected pore volumes for different C values.

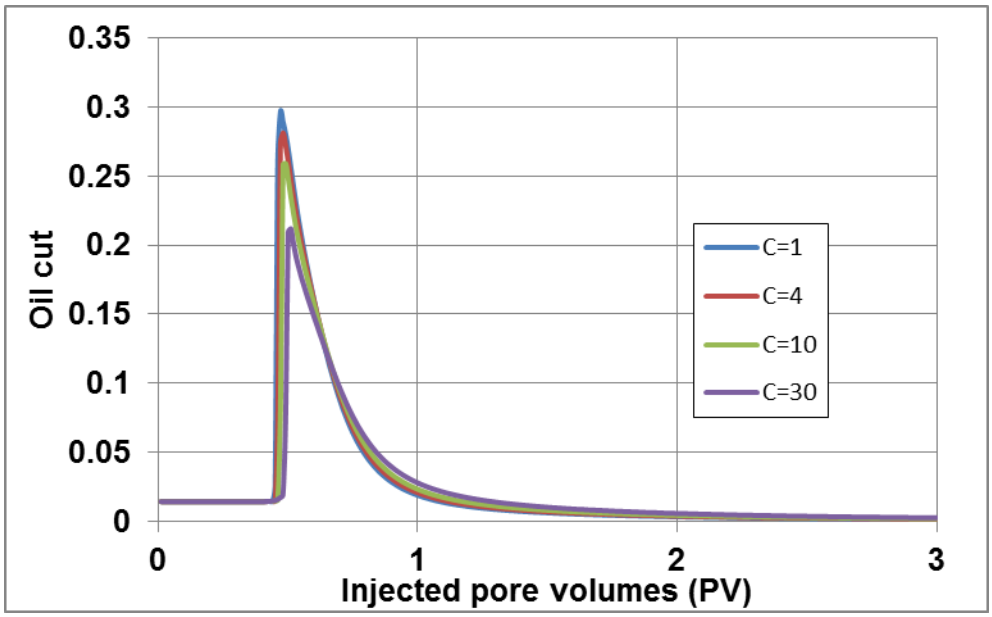

Figure 6.8: Oil cut vs. injected pore volumes for different C values.

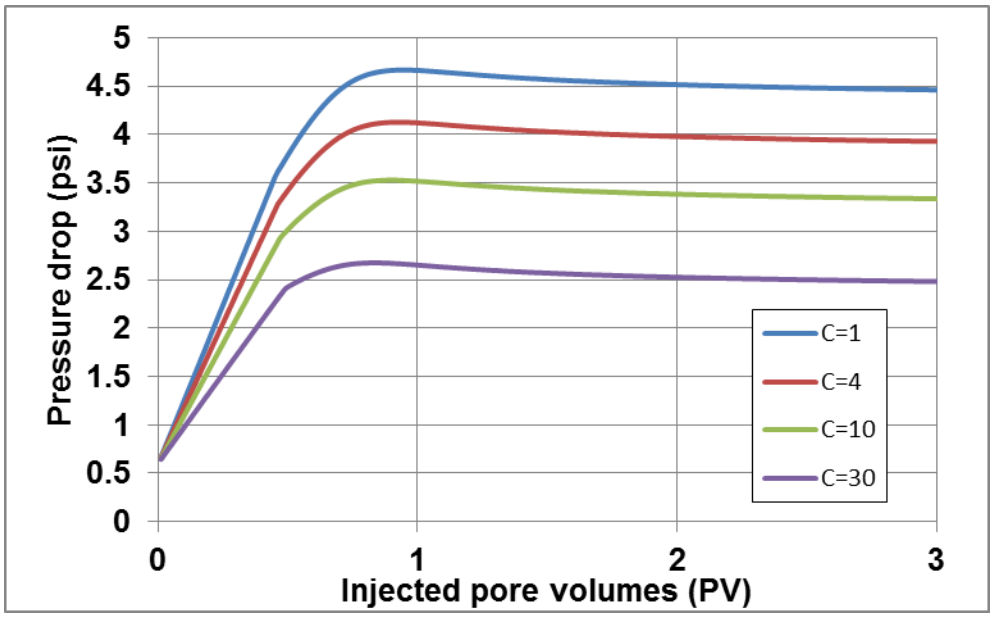

Figure 6.9: Pressure drop vs. injected pore volumes for different C values.

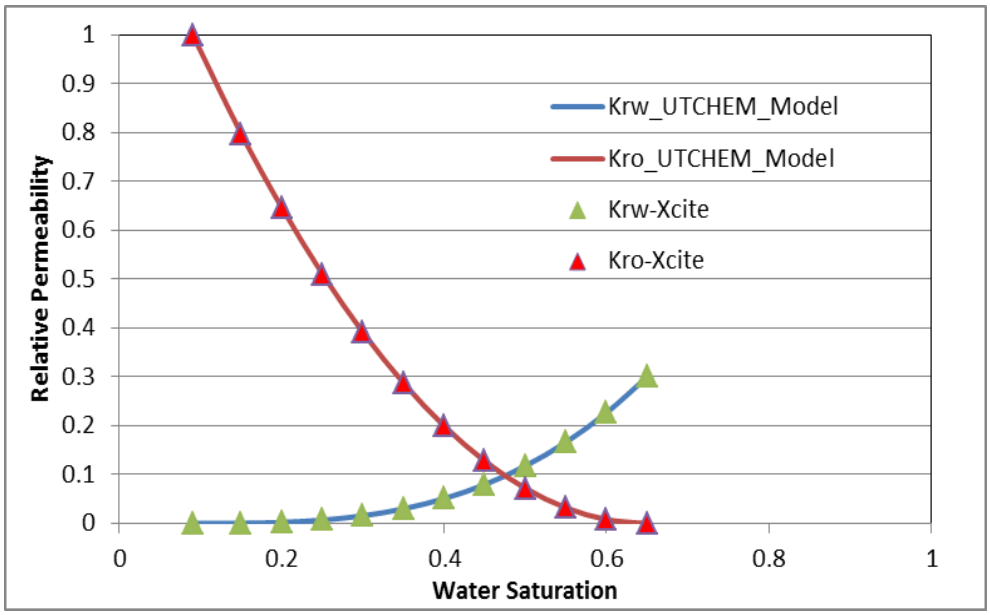

Figure 6.10: Water-oil relative permeability curves (points are from tables provided by Xcite, lines are curve fit to Corey function).

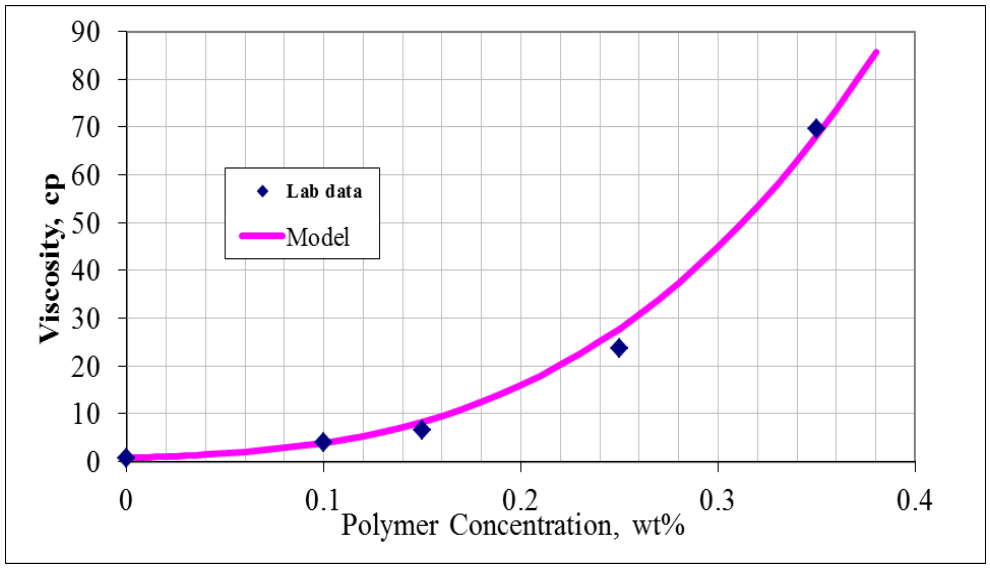

Figure 6.11: Viscosity of ChemPam 8177 measured as a function of polymer concentration at reservoir temperature of 40 °C and low shear rate (points are measured data and lines are the model fit).

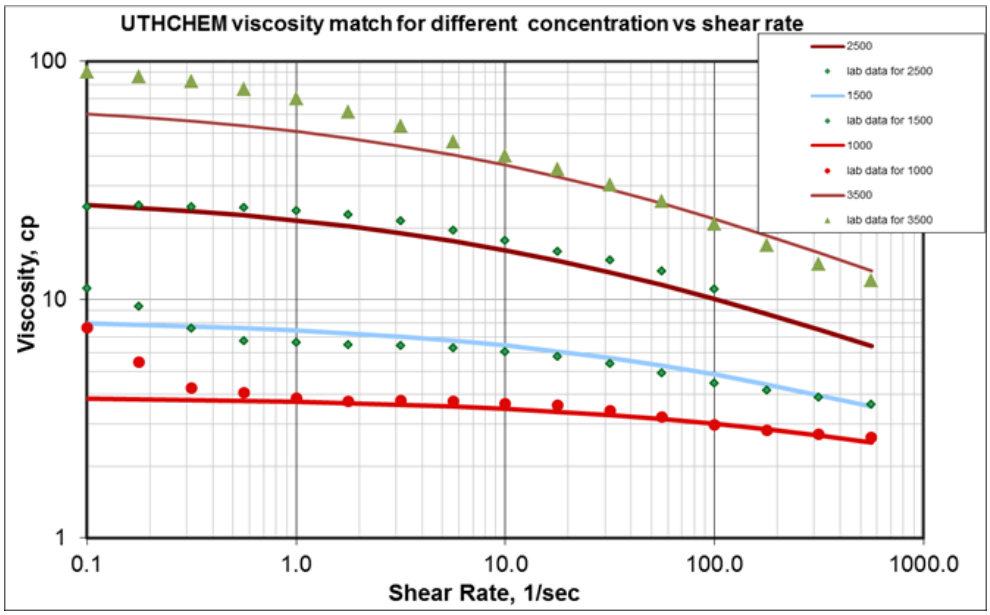

Figure 6.12: Effect of shear rate on viscosity of ChemPam 8177 measured at reservoir temperature of 40 °C (points are measured data and lines are the model fit).

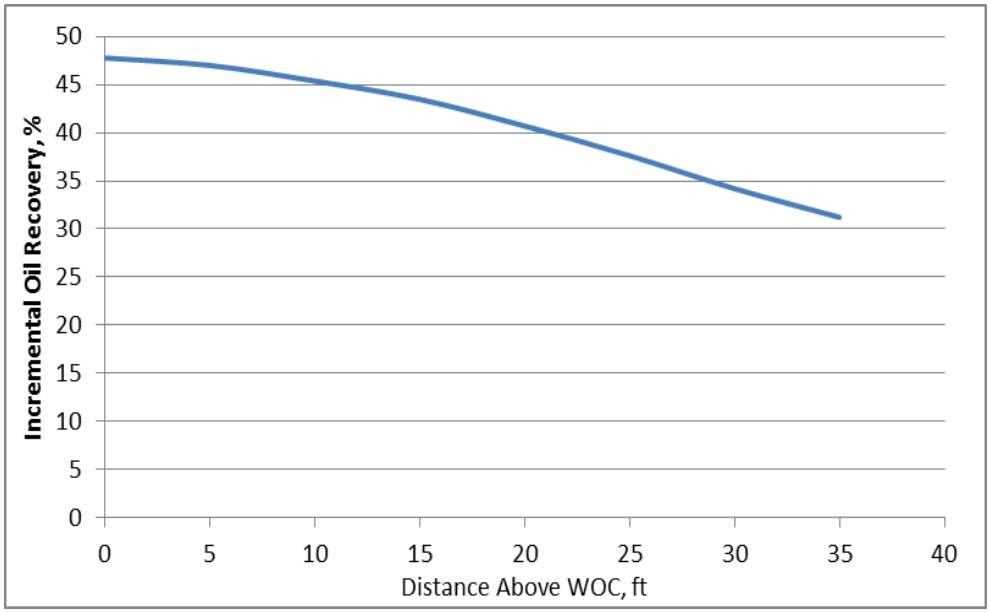

Figure 6.13: Sensitivity of injector location for polymer flooding cases when using infinite aquifer model.

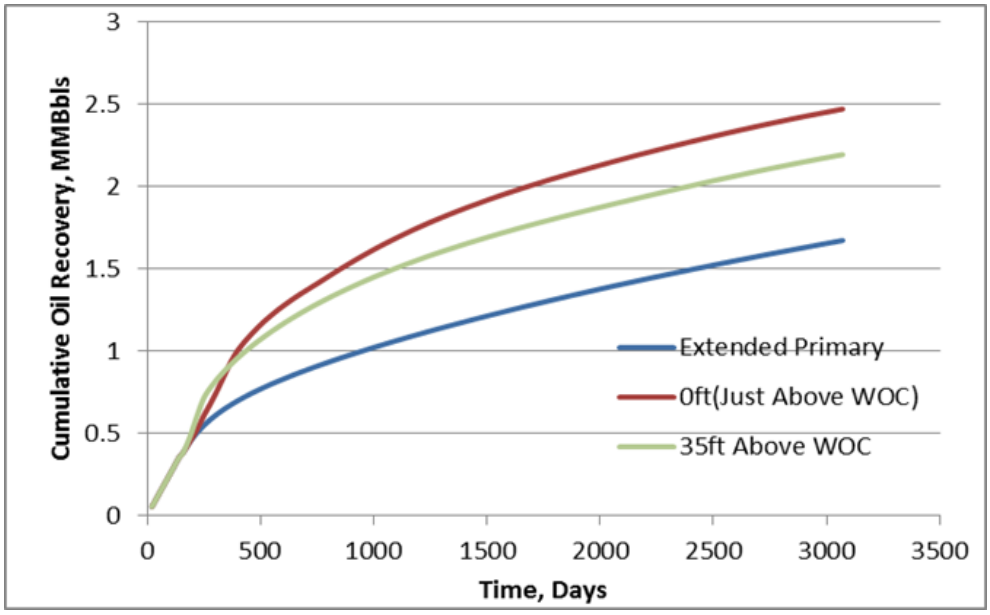

Figure 6.14: Cumulative oil production for primary depletion and polymer flood for well location optimization.

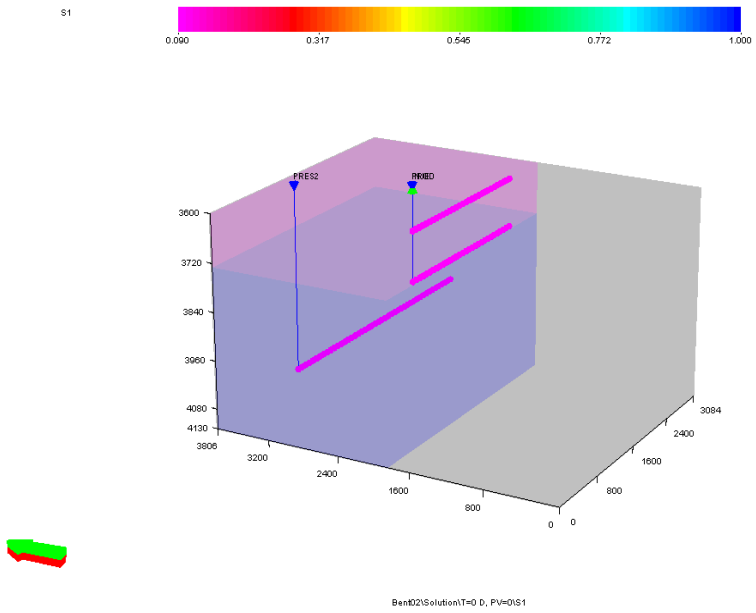

Figure 6.15: Box model with two pressure-constrained injection wells in the aquifer.

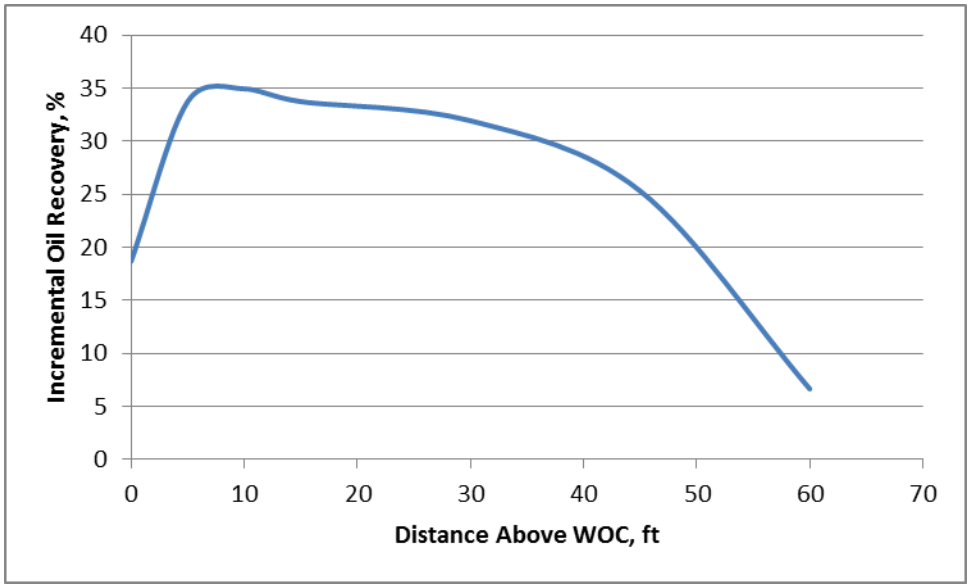

Figure 6.16: Sensitivity of injector location for polymer flooding cases when using pressure-stabilized aquifer.

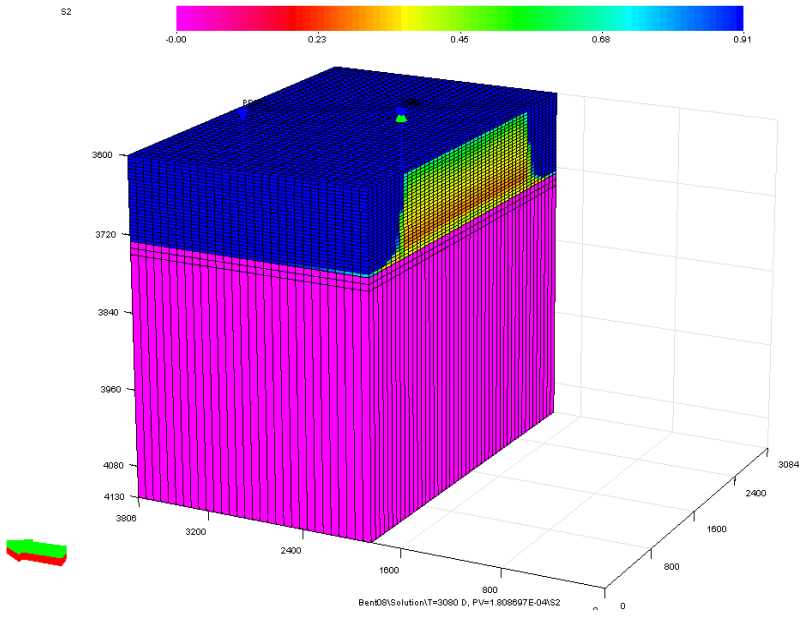

Figure 6.17: Oil saturation at T = 3080 days (Y-Z cross section at NX = 29).

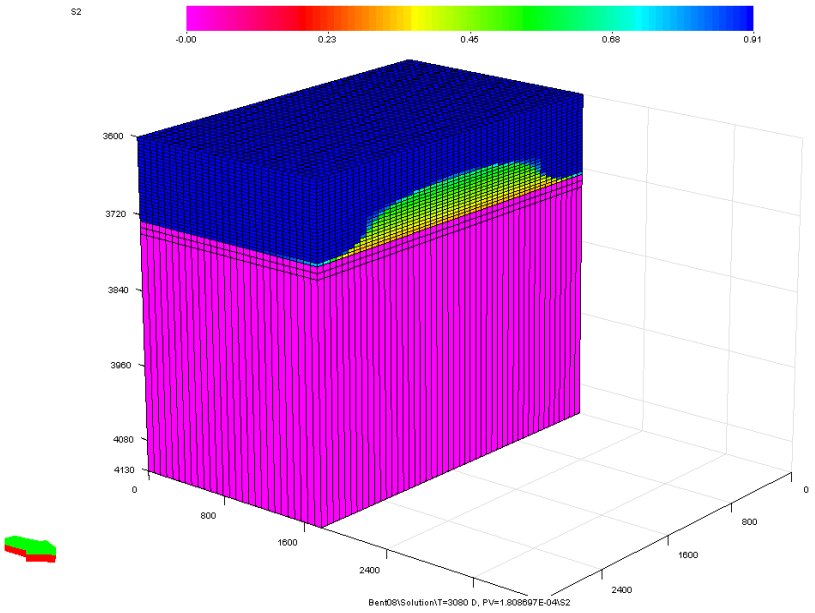

Figure 6.18: Oil saturation at T = 3080 days (Y-Z cross section at NX = 27).

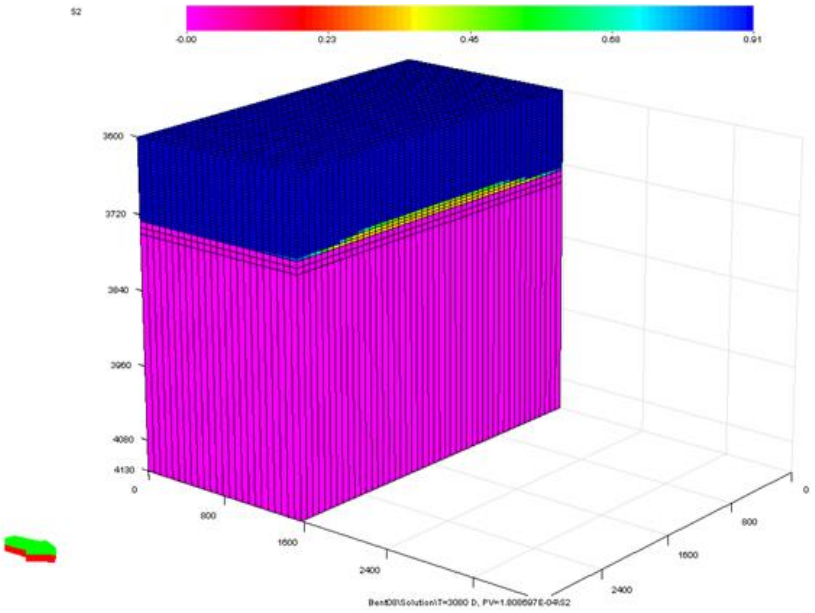

Figure 6.19: Oil saturation at T = 3080 days (Y-Z cross section at NX = 24).

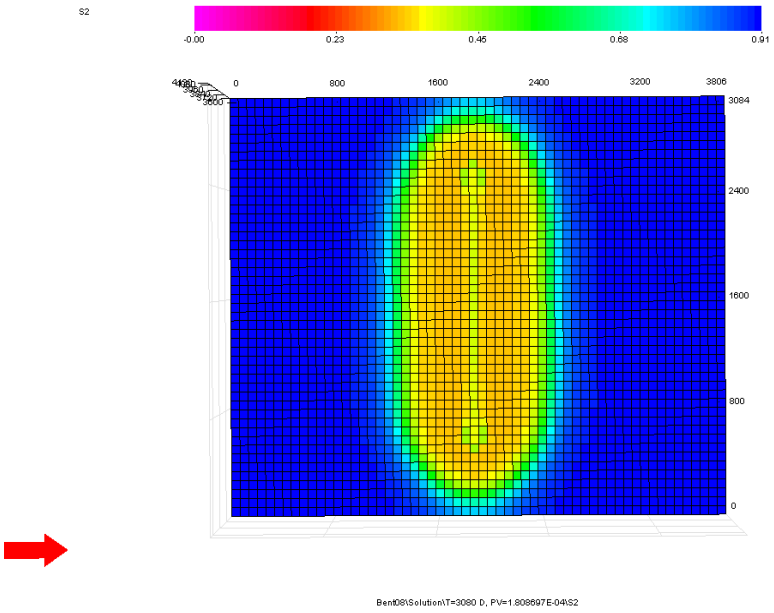

(a)

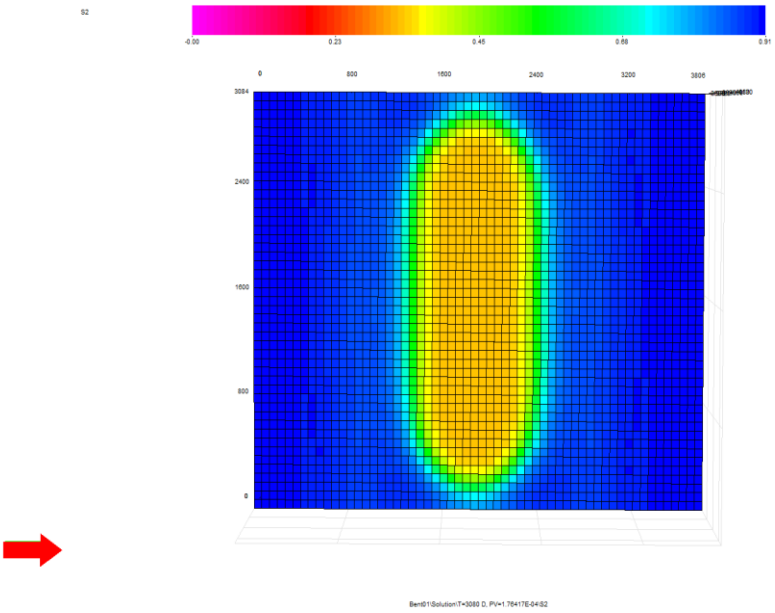

(b)

Figure 6.20: Oil saturation at T = 3080 days (X-Y cross section at NZ = 26, WOC): (a) with polymer, (b) without polymer

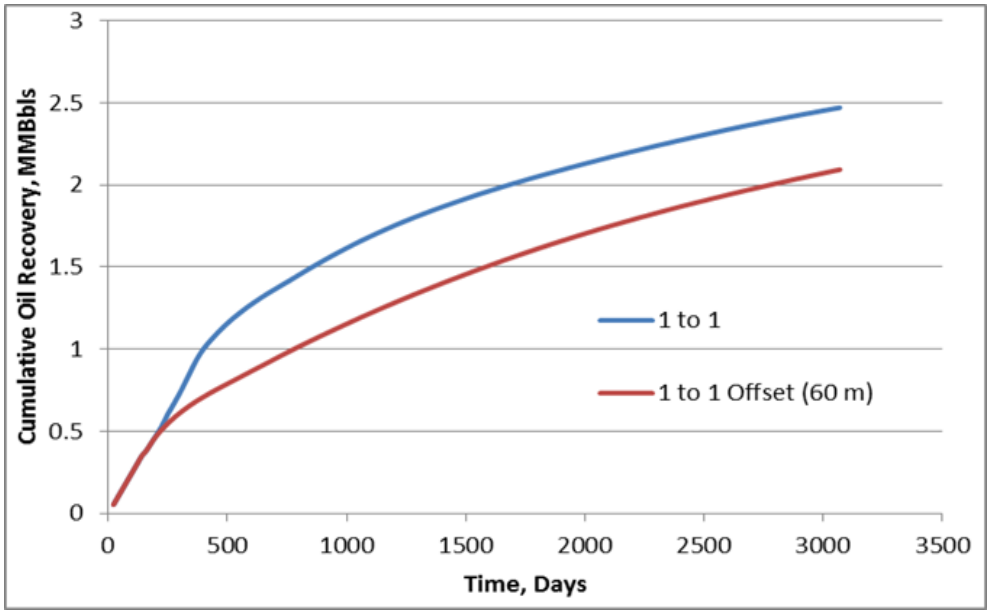

Figure 6.21: Oil recovery for 1 to 1 Case vs. 1 to 1 Offset Case.

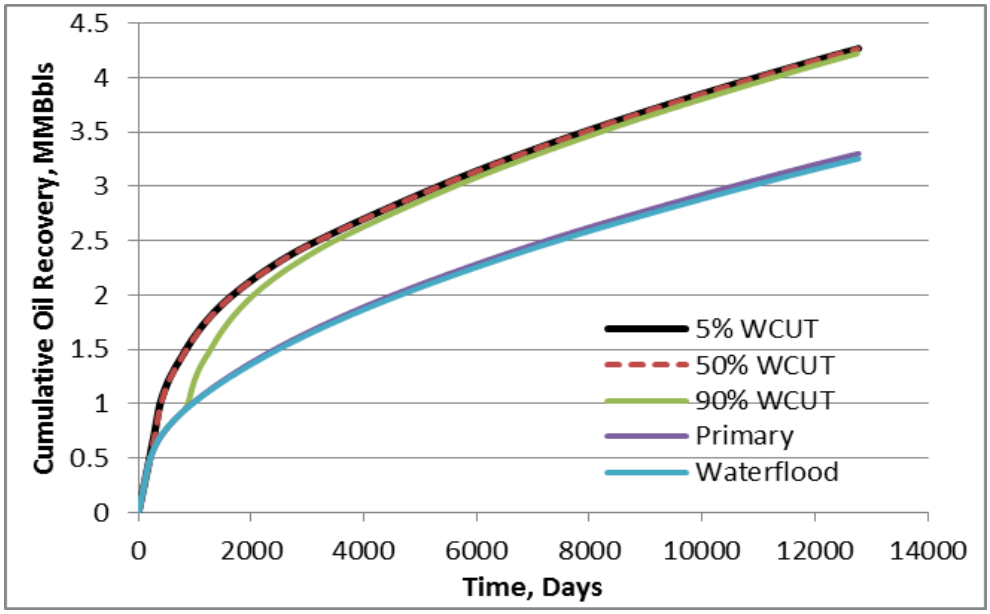

Figure 6.22: Oil recoveries at different water cut vs. extended primary production and waterflood.

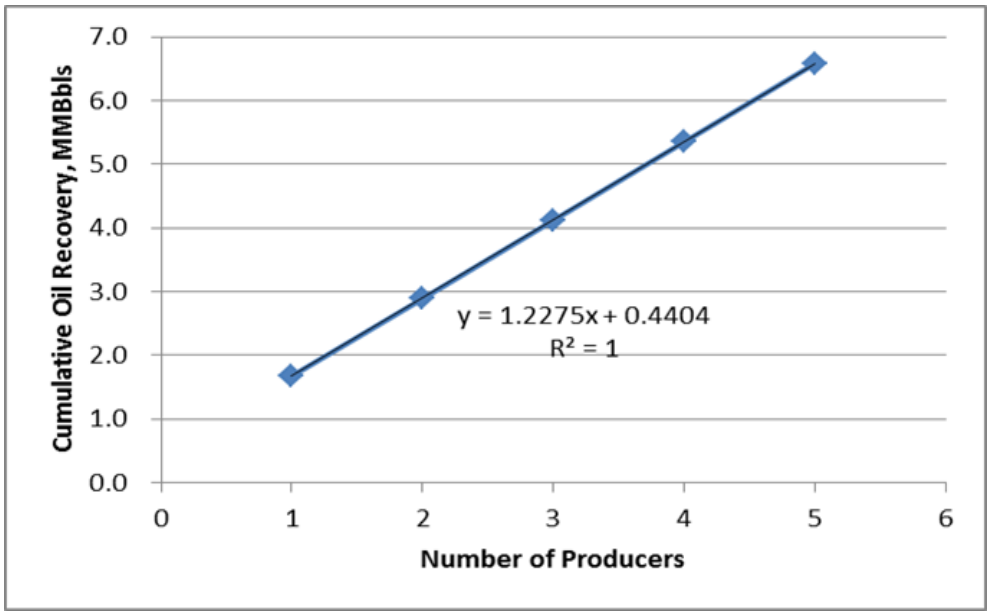

Figure 6.23: Simulation of the sensitivity to number of producers.

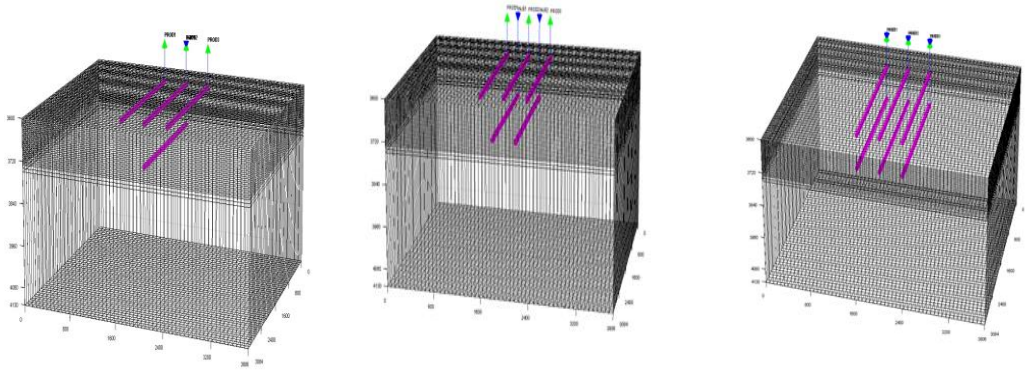

(a) (b) (c)

Figure 6.24: Well locations for (a) 3 Producers to 1 Injector, (b) 3 Producers to 2 Injectors, (c) 3 Producers to 3 Injectors simulation cases.

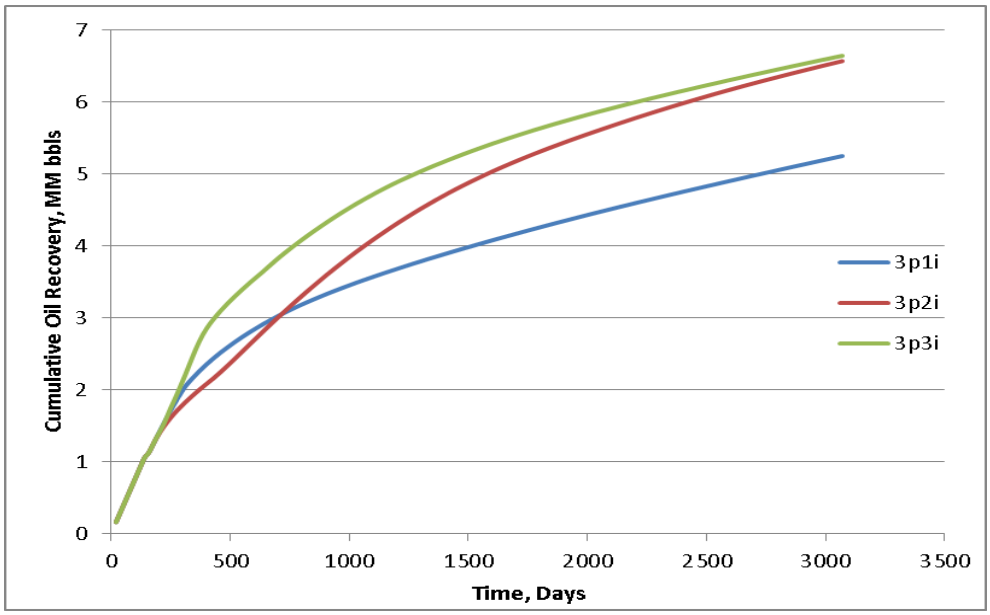

Figure 6.25: Simulation of the sensitivity to number of injectors during polymer flooding.

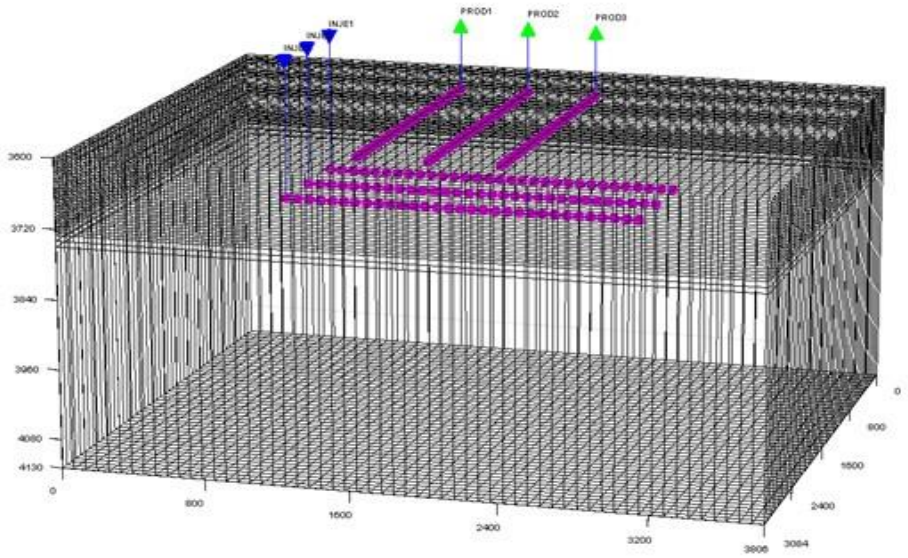

Figure 6.26: Injector orientation in the 3p3ivt Case.

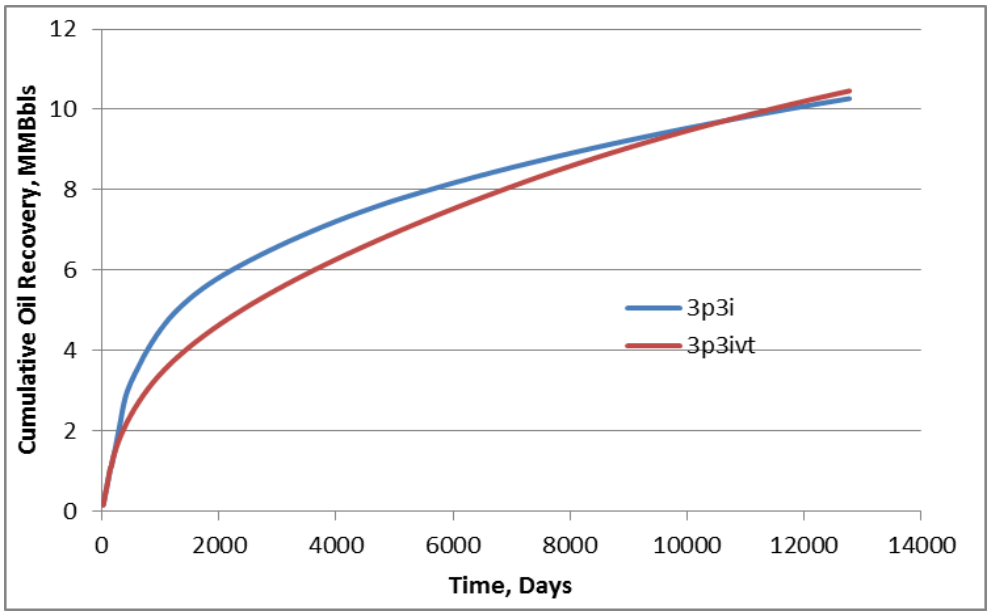

Figure 6.27: Simulation of the sensitivity to injector orientation (3 to 3 Cases) in 35 years.

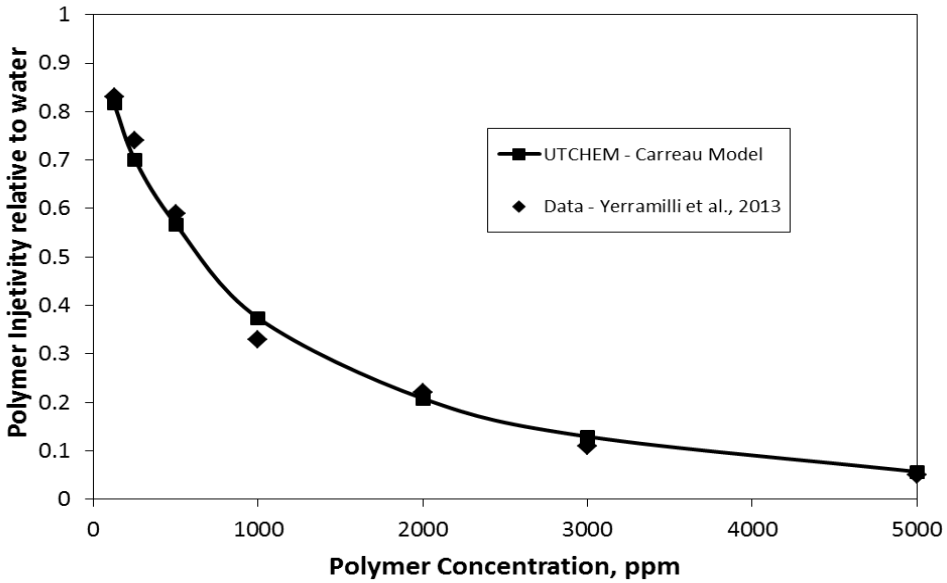

Figure 6.28: Coreflood simulations: polymer injectivity relative water vs. polymer concentration.

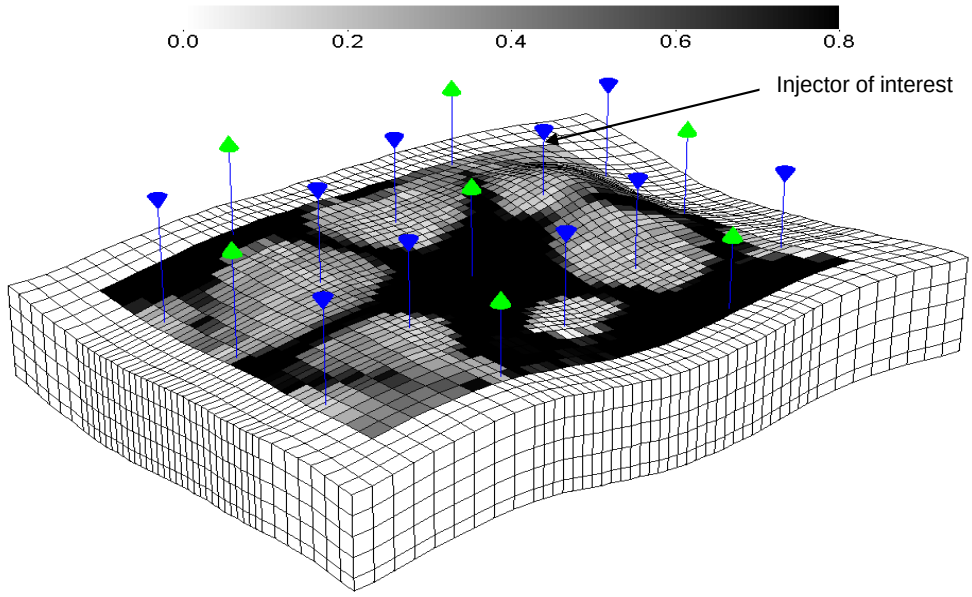

Figure 6.29: Oil saturation distribution for field case 1 at 195 days.

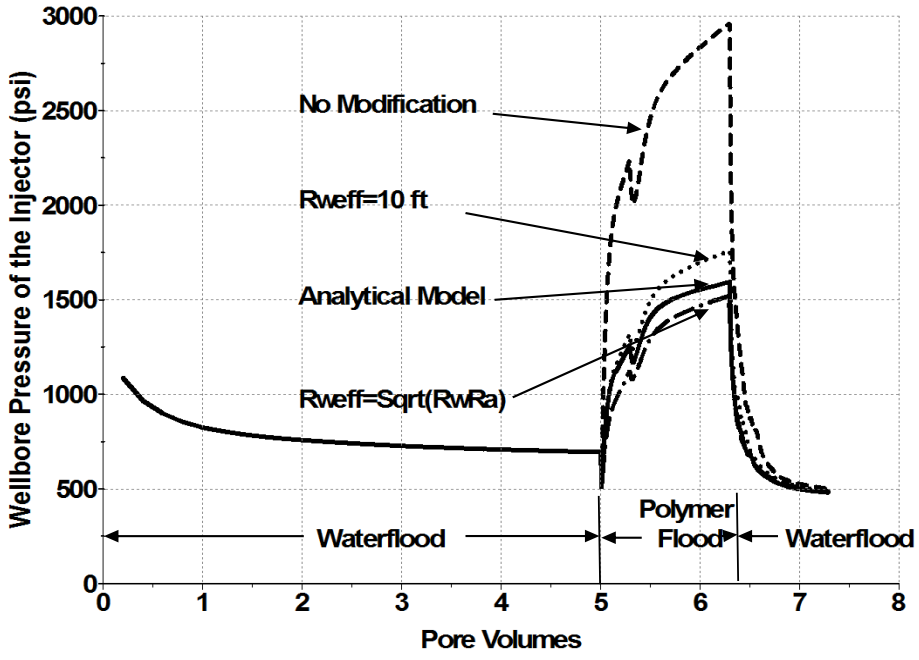

Figure 6.30: Wellbore pressure of the injector of interest vs. injected pore volumes for field case 1.

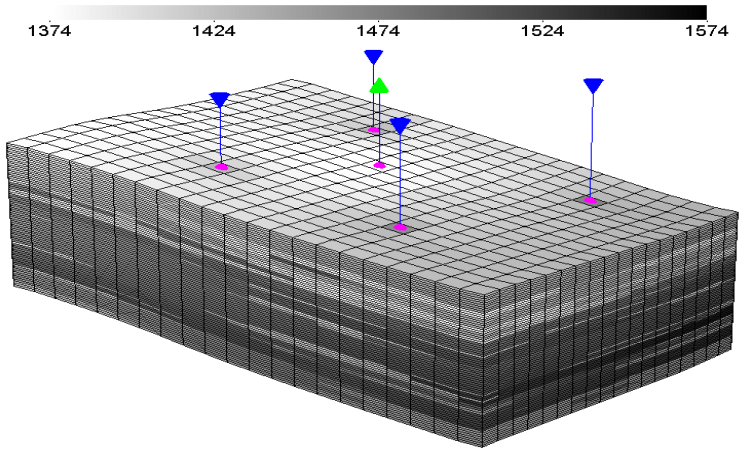

Figure 6.31: Reservoir pressure distribution at 300 days for field case 2.

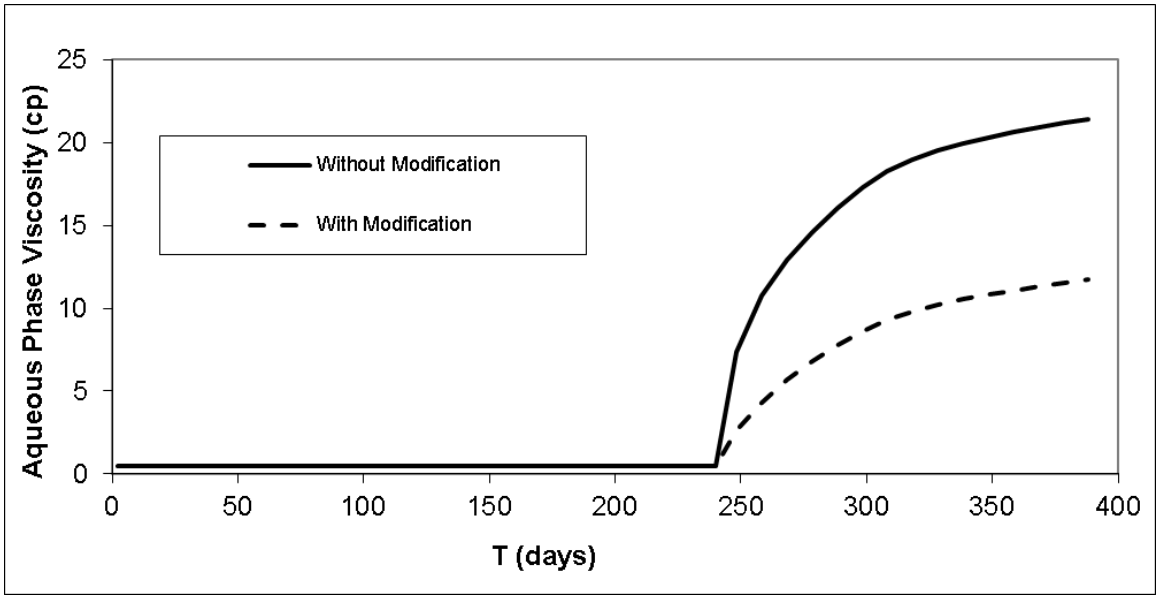

Figure 6.32: Aqueous phase viscosity around injector 1 for field case 2.

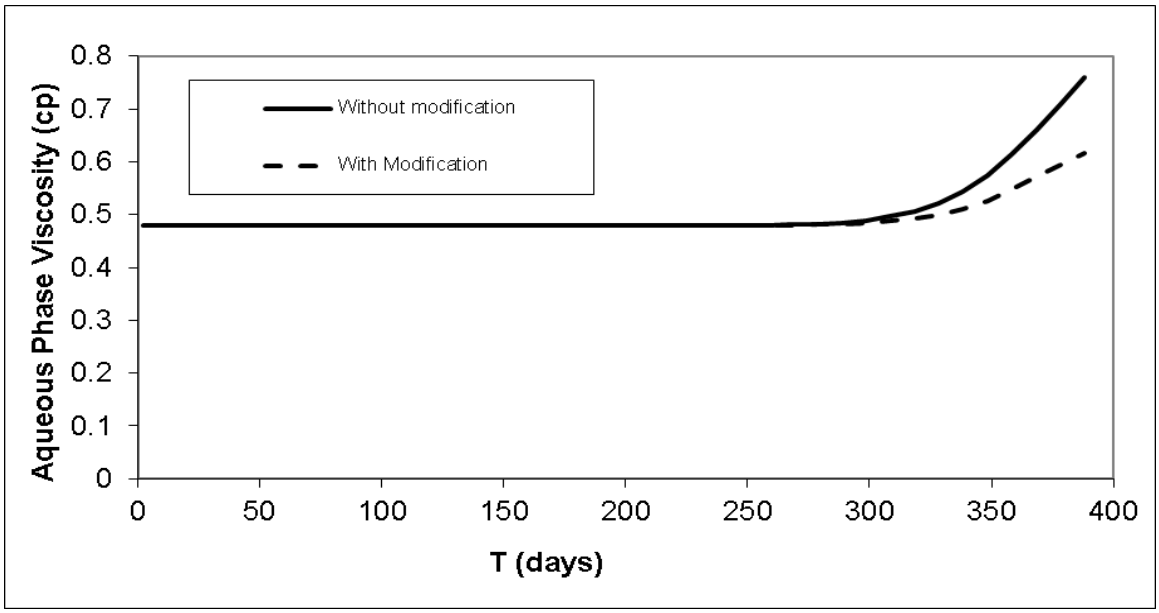

Figure 6.33: Aqueous phase viscosity around producer for field case 2.

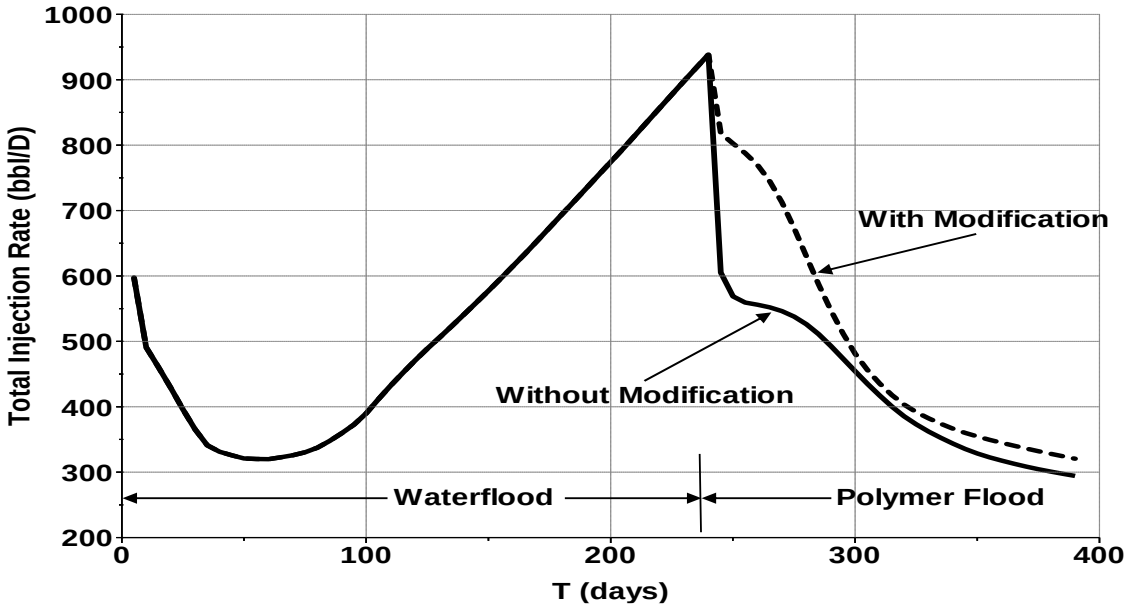

Figure 6.34: Injection rate of injector 1 vs. time in days for field case 2.

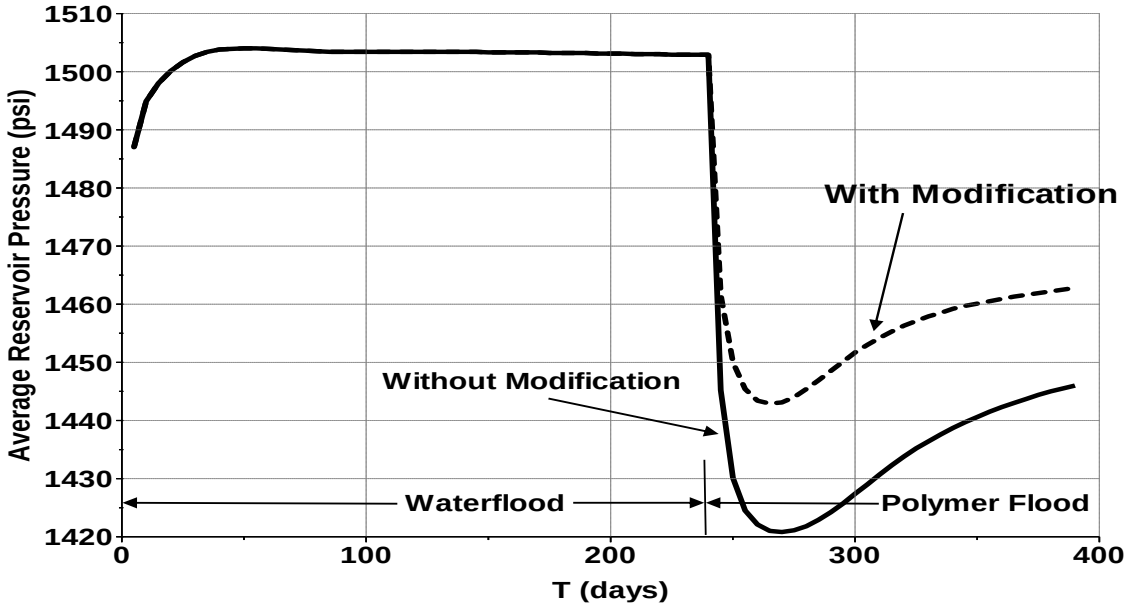

Figure 6.35: Average reservoir pressure vs. time in days for field case 2.

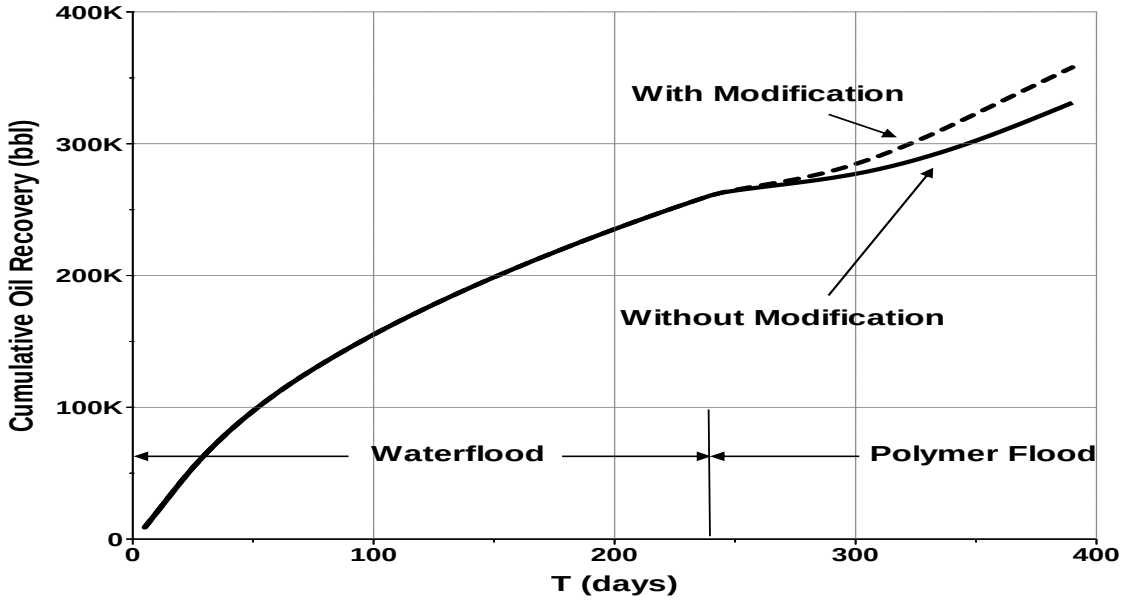

Figure 6.36: Cumulative oil recovery vs. time in days for field case 2.

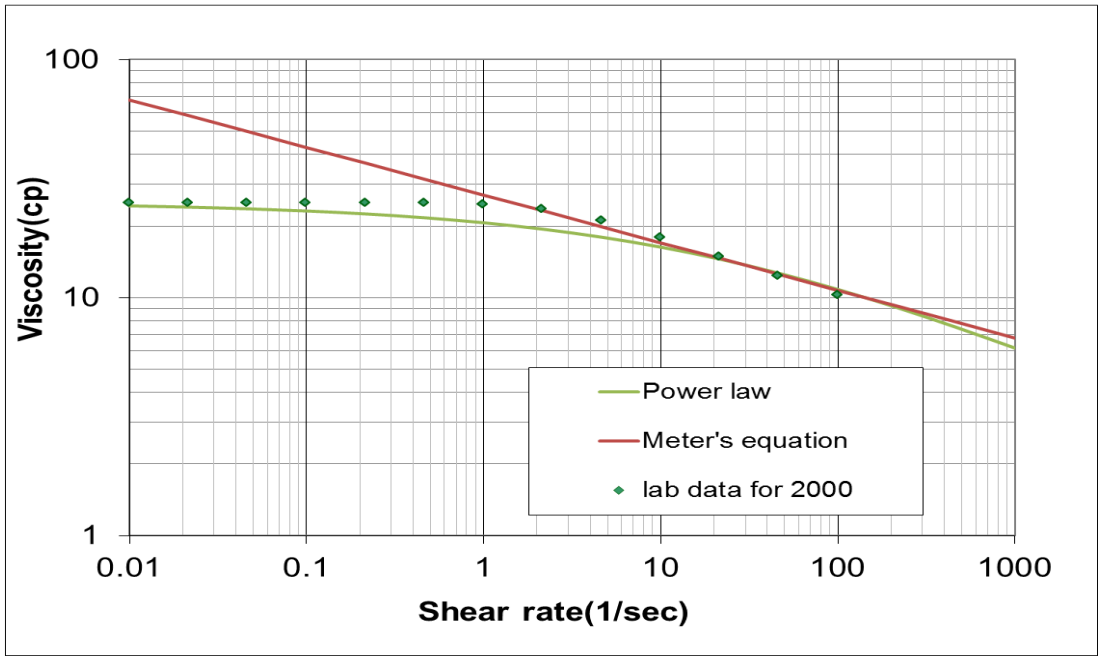

Figure 6.37: Polymer rheology for comparison of UTCHEM with UTWID.

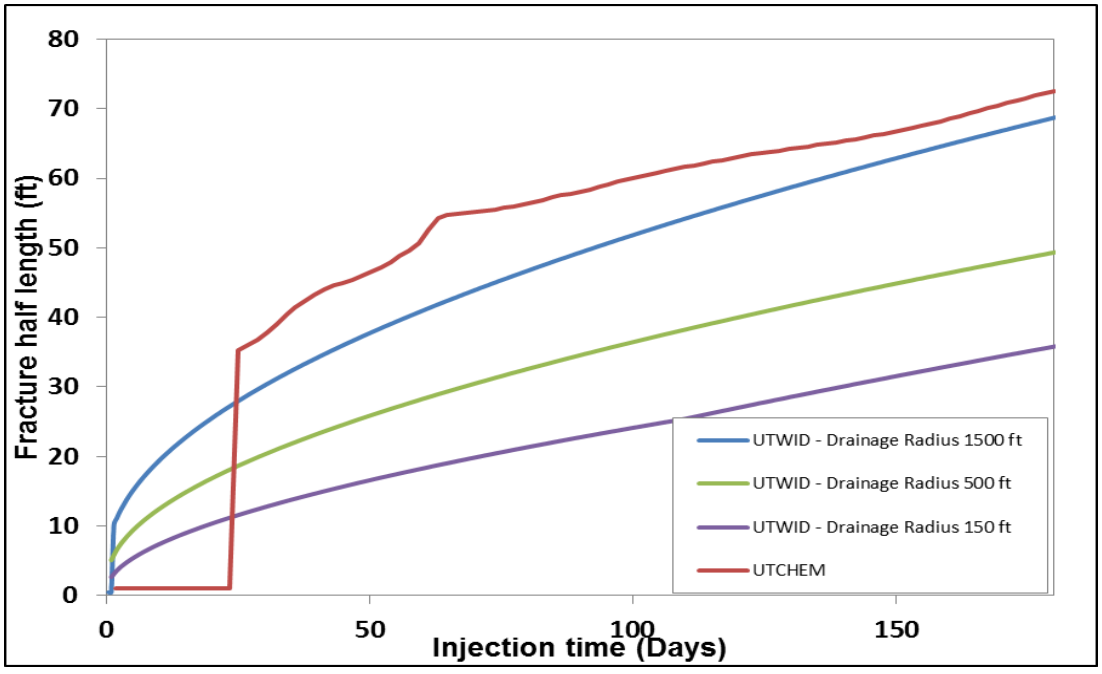

Figure 6.38: Fracture half-length for comparison of UTCHEM with UTWID.

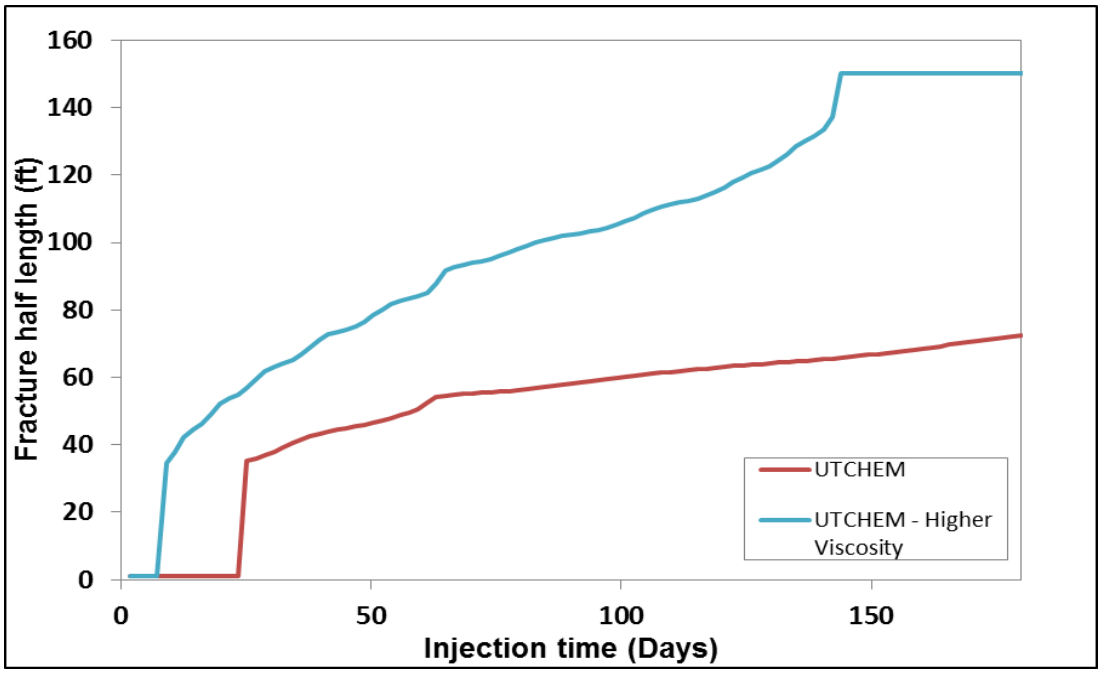

Figure 6.39: Early fracture initiation for higher polymer concentration.

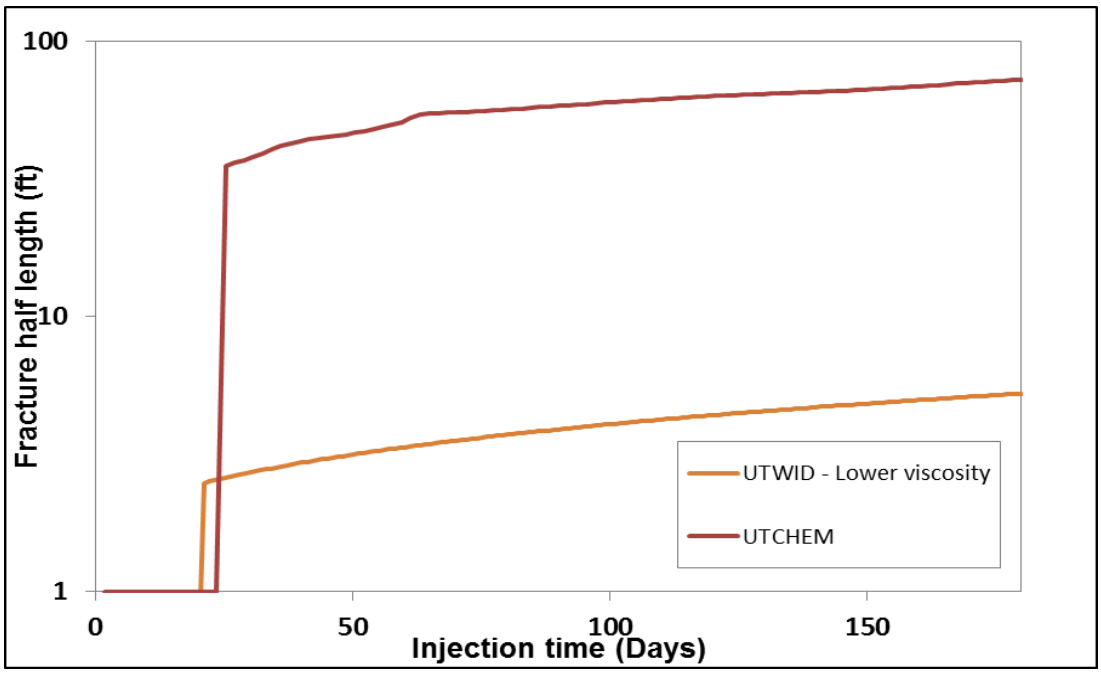

Figure 6.40: Delay of fracture initiation using a lower polymer concentration.

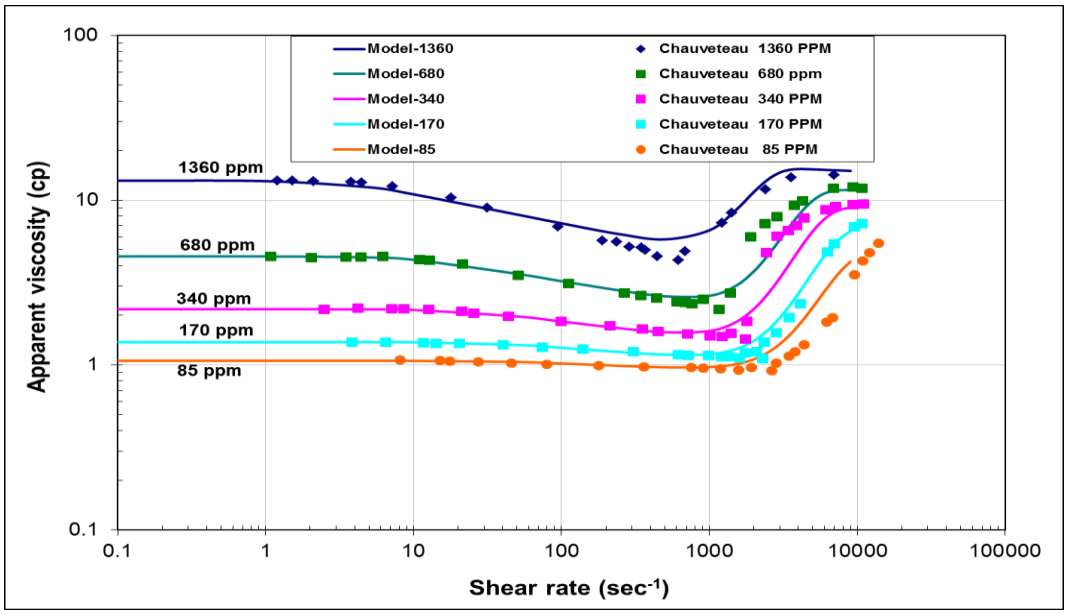

Figure 6.41: HPAM rheological data matched using UVM model.

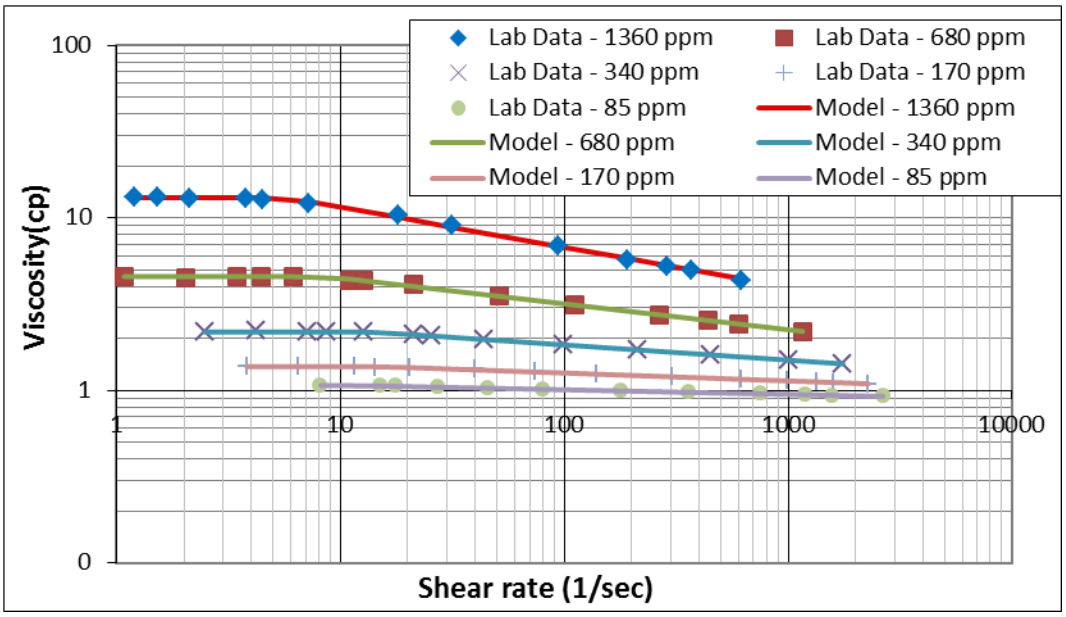

Figure 6.42: Shear-thinning rheological part matched using modified power law model.

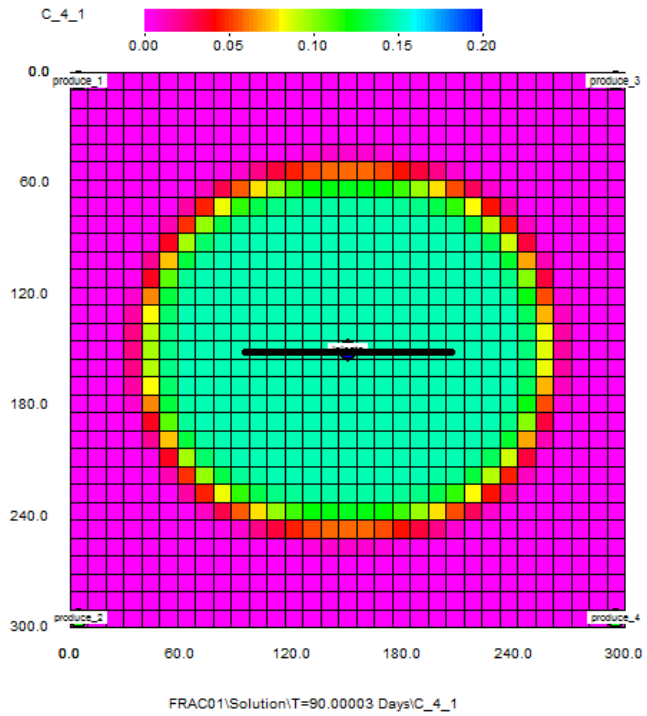

Figure 6.43: Polymer concentration distribution at T=90 days.

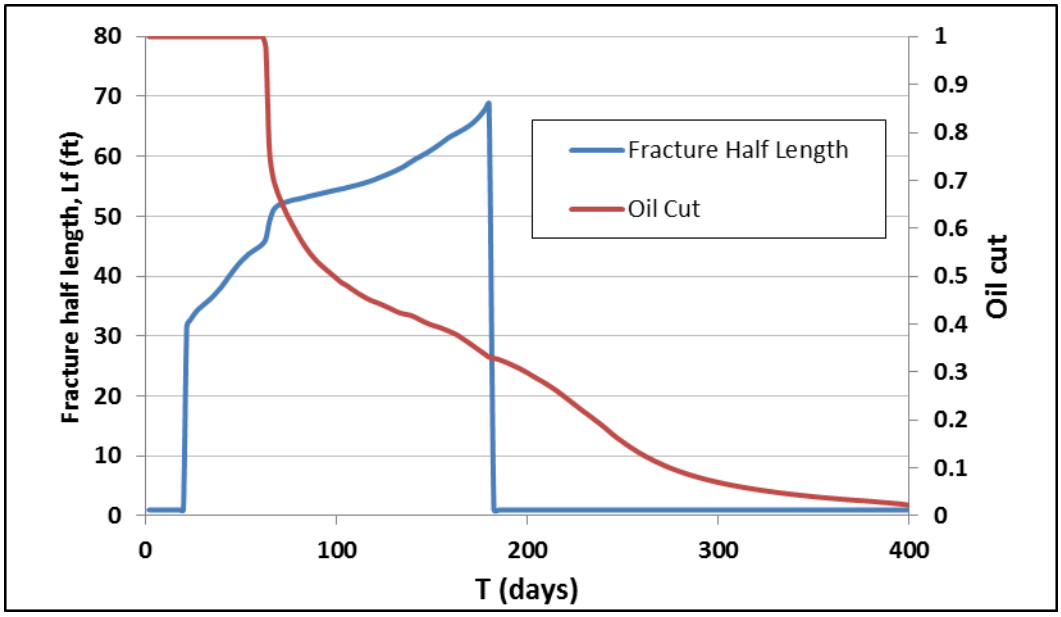

Figure 6.44: Fracture half-length/oil cut vs. injection time in days.

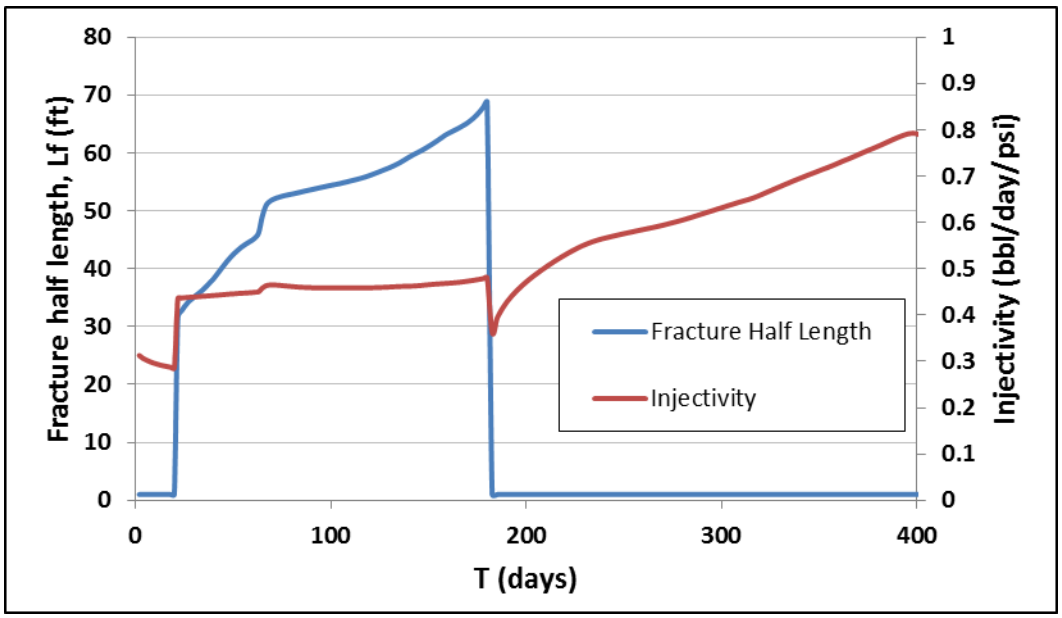

Figure 6.45: Fracture half-length/injectivity vs. injection time in days.

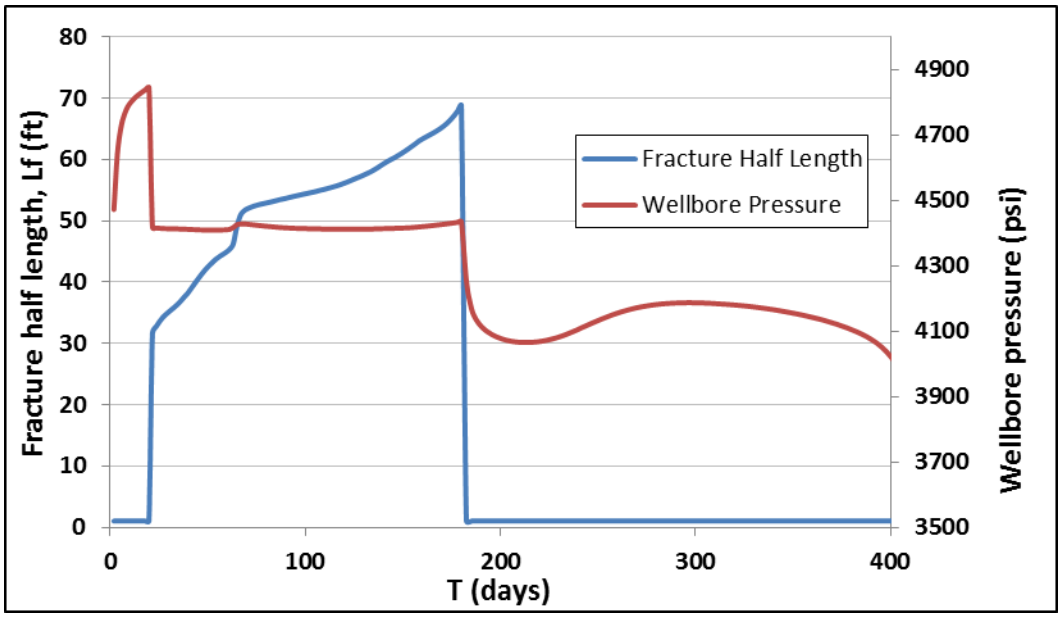

Figure 6.46: Fracture half-length/wellbore pressure vs. injection time in days.

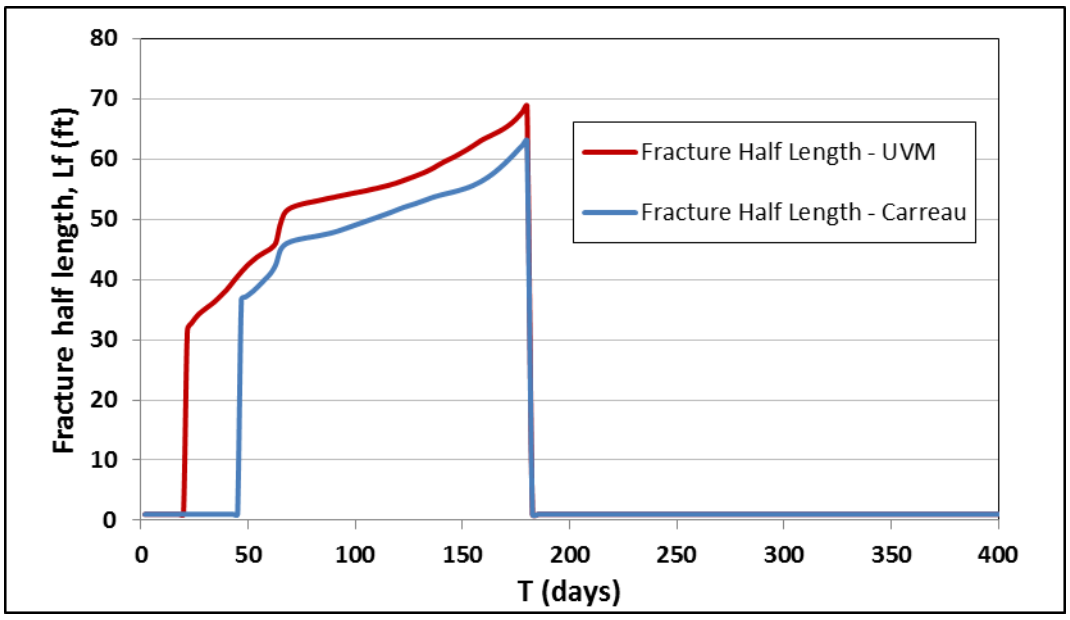

Figure 6.47: Comparison of fracture half-lengths for the UVM model and Carreau model.

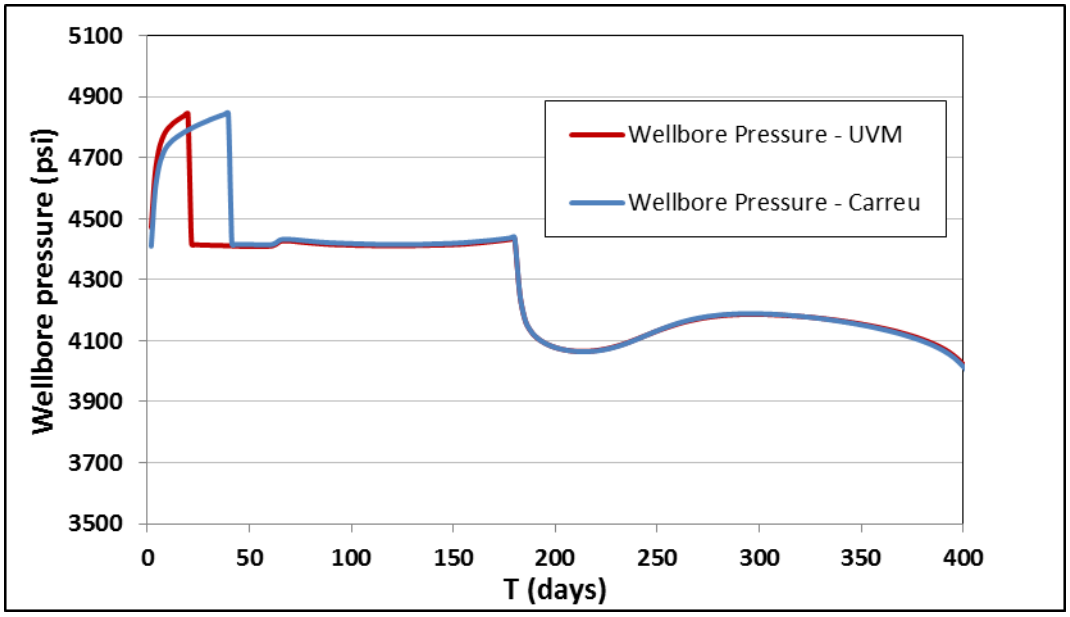

Figure 6.48: Comparison of wellbore pressure for the UVM model and Carreau model.

Chapter 7: Summary, Conclusions, and Recommendations

7.1 Summary and Conclusions

This dissertation is focused on development, validation and application of UTCHEM. We introduced implicit well rate allocation scheme to treat rate-constraint well implicitly for more accurate fluid allocation in different layers when there is a limited cross flow between the layers. An infinite aquifer model was implicitly implemented to accurately and more efficiently model the strength and impact of aquifer influx to the reservoir performance. The timestep control schemes were also improved to enhance the simulation stability and CPU times. Inactive cells were excluded from the pressure and concentration equations to reduce redundant calculations and also improve the numerical stability and accuracy. Both direct and iterative solvers were implemented into the simulator to solve the pressure equation of ill-conditioned/non-symmetric coefficient matrices. This enhanced simulator showed improvements in accuracy, robustness and computational efficiency in handling heterogeneous reservoir models.

To model polymer flooding in complex reservoirs, we also improved polymer rheology models by implementing Wreath's correlation which estimates the shear correction factor for properties such as permeability, porosity, saturation, and polymer type. Wreath's correlation parameters can be obtained by matching multiple sets of polymer coreflood experimental data, which is time-consuming and might be impossible for realistic studies. Simulation studies showed that for a heterogeneous reservoir, it is important to characterize the C value in its high permeable zone which contributes to a larger portion of the flow rate compared with the low permeable zone. It was found that in coreflood simulation studies, pressure drop is sensitive to the C values, while cumulative oil recovery or oil cut curves are insensitive to the C values.

Application of polymer flooding in a heavy oil reservoir with a bottom aquifer was studied to prove the applicability in this research frontier. The heavy oil reservoir was simplified using a box model. Several conclusions were drawn based on our sensitivity studies. For aquifer modeled with the semi-analytical infinite aquifer model, the optimum injection depth is just above the WOC; polymer flood incremental recovery over water flood is about 48%, which is substantial. When two pressure-constraint injectors are used to mimic strong water influxes, the optimum injection well location is 10 ft above the WOC. The delay in polymer flooding only slightly decreases the final oil recovery which is useful as it allows time to develop and implement polymer facilities and enables monitoring of well performance prior to commencement of waterflood. However, further simulations are needed to study the viscoelastic effect of high concentration of large molecular weight polymers. Oil recovery increases linearly with the number of producers for primary production (no injection). This could help in deciding when to add an injector or producer. Three producer to two injector well arrangement produces almost the same amount of oil (6.56 MM bbls) as the 3 producer to 3 injector case (6.63 MM bbls) in 8 years. Different orientations of injection wells may improve cumulative oil recovery by enlarging the swept volume. More simulations are required to optimize the well orientation. An important issue in heavy oil recovery is the viscous fingering effect, which however were not captured in our simulations. Adverse viscosity ratios during the waterflooding in viscous oil reservois lead to viscous fingers and render the displacing process less effective. High water cut may be reached at very early times with large amounts of oil left in the reservoir. Polymer flooding in heavy oil reservoirs can reduce fingering and stabilize the displacement process. For heavy oil recovery, due to the improve mobility ratio, concentrated polymer flood can improve both volumetric and displacement sweep efficiencies by lowering the oil saturation below

waterflood residual oil saturations. Very fine grid models can be used to investigate the importance of fingers in coreflood simulations. In field scale simulations, results from coreflood studies need to be upscaled in sophisticated ways to capture the fingering effect (Doorwar and Mohanty, 2011).

Another study was on modeling polymer injectivity, which is considered as the main contribution of this research work. A semi-analytical polymer injectivity model was developed and implemented in UTCHEM. This model was validated against fine-grid Cartesian-grid simulations and also radial-grid simulation. 1D polymer coreflood simulations were conducted to match experimental data. The close match between simulation results and experimental data validated the Carreau model and its implementation in UTCHEM. Coreflood experiments and simulation studies are necessary because they provide input parameters for field-scale polymer flood simulations. The semi-analytical injectivity model was successfully verified for field-scale simulations using a fine-grid field simulation and its up-scaled counterpart. Application of the semi-analytical polymer injectivity model in simulating polymer flooding in field applications showed the importance of capturing near-wellbore polymer rheology and its effects on polymer injectivity and average reservoir pressure. Based on this study, it is believed that grid effect needs to be considered for reservoir simulation of polymer flood. Our analytical model helps to eliminate the grid effect and thus gives a more accurate polymer injectivity.

Furthermore, a facture propagation model was implicitly coupled with UTCHEM. The fracture was treated using average permeability scheme in the simulation. The scheme was validated using a model with a static fracture attached to the injection well. Fracture propagation during polymer flooding was simulated to show the impact of hydraulically induced fracture on polymer injectivity and flood performance. The

coupled model was compared with the semi-analytical, single-injection-well simulator, UTWID. The results from UTCHEM and UTWID showed qualitative agreement despite different fracture models, assumptions, and approaches used. The coupled simulator can be used to optimize polymer flood concerning polymer injectivity, impact of fracture growth on sweep efficiency, flow out of zone, etc. Preliminary simulation results showed how fracture growth is affected by total mobility of multiphase fluid flow. It also showed the impact of polymer rheology on fracture initiation and fracture growth. Fracture initiation releases pressure buildup in the wellbore and significantly enhances polymer injectivity. The semi-analytical polymer injectivity model helps to capture polymer rheology in the near-wellbore area without the need of using fine-size grids. For synthetic polymer, shear-thickening effect helps to induce earlier fracture initiation. After fracture initiation, wellbore pressures or polymer injectivities are almost the same for shear-thinning and shear-thickening polymers. This implies that shear-thickening effect is only important for near-wellbore areas. Similar results on fracture initiation were observed in the simulation study by Ma (2015).

7.2 Recommendations for Future Work

Considering the limitation of this study, we list plausible future work as follows:

- Improve robustness and computational efficiency of UTCHEM using the IMPSAT formulation (Cao, 2002) which treats pressure and saturation implicitly while other primary variables are treated explicitly. The IMPSAT formulation significantly improves the robustness of IMPEC/IMPES scheme. Besides, it requires much less labor to adapt the current formulation than using a fully implicit formulation;

- Couple a geomechanical simulator (e.g., Ganis *et al.*, 2013) with UTCHEM to include the geomechanical effect. Polymer flooding may involve geomechanical risks such as borehole failure, etc. Besides, geomechanical effects need to be taken into account for accurately modeling fracture growth and reservoir properties such as porosity and permeability;
- Couple the PKN model and 3D/pseudo-3D fracture models with UTCHEM. An important issue that has not been considered in our current fracture model is to model fracture propagation in vertical direction. This can be achieved by implementing a 3D/pseudo-3D fracture model;
- Include Todd-Longstaff technique on treating non-ideal mixing effects on polymer solution viscosity (Todd and Longstaff, 1972);
- Model and simulate unstable floods in heavy oil reservoir (Doorwar and Mohanty, 2011);
- Model and simulate low-salinity polymer flooding (Luo *et al.*, 2015);
- Model physical properties of associative polymer (Wassmuth *et al.*, 2012).

Appendix A: Pressure Distribution due to Power Law Flow in Fracture

In this appendix, the pressure distribution within a fracture due to non-Newtonian fluid flow is analytically calculated. The analytical solution of flow of a power-law fluid through a narrow slit was given by Bird *et al*. (2007) as shown below:

$$q = \frac{AB}{2+\frac{1}{n}}\left(\left|\frac{\Delta P}{\Delta L}\right|\frac{B}{K}\right)^{\frac{1}{n}} \qquad [A.1]$$

where q is the flow rate through the cross section of the slit, B is the half thickness of the narrow slit, A is the area of the cross section, K and n are the power law parameters, and $\frac{\Delta P}{\Delta L}$ is the pressure gradient along the flow direction. Then for the flow rate through one wing of the fracture, the Eq. [A-1] is converted to:

$$q_f = \frac{2h_f\left(\frac{w_f}{2}\right)^2}{2+\frac{1}{n}}\left(\left|\frac{dp_f}{dx_f}\right|\frac{w_f}{2K}\right)^{\frac{1}{n}} \qquad [A.2]$$

and the pressure gradient in this wing of the fracture is

$$\frac{dp_f}{dx_f} = -2K\left(\frac{2q_f}{h_f}\frac{2n+1}{n}\right)^n\left(\frac{1}{w_f}\right)^{2n+1} \qquad [A.3]$$

To account for turbulent effect in the fracture due to high injection rate, we adopted the same treatment by Perkins and Kern (1961) and Suri *et al*. (2009) by introducing a correction factor, C_{Turb} in the expression above:

$$\frac{dp_f}{dx_f} = -2C_{Turb}K\left(\frac{2q_f}{h_f}\frac{2n+1}{n}\right)^n\left(\frac{1}{w_f}\right)^{2n+1} \qquad [A.4]$$

where C_{Turb}=1 when the flow is laminar and C_{Turb}=16/3π when it is turbulent.

At the inlet of the fracture, which is at the wellbore, the fluid flow rate, q_f, is half of the total injection rate, q_{inj}, assuming the problem is symmetric. If there is no-leak along the fracture, q_f is constant. If all of the fluid into the fracture leaks out of the fracture and the leak-off is uniform along the fracture (Suri *et al.*, 2009), then

$$q_f = \frac{1}{2}q_{inj}\left(1-\frac{x_f}{L_f}\right) \qquad [A.5]$$

Substitution of Eq. [A.6] and the fracture geometry equation, Eq. [5.7], into Eq. [A-4] gives:

$$p_f(x_f) - p_{foc} = \left(\frac{\Phi q_{inj}^n L_f}{n+1}\right)^{\frac{1}{2n+2}}\left(1-\frac{x_f}{L_f}\right)^{\frac{1}{2}} \qquad [A.6]$$

where

$$\Phi = 4(n+1)C_{Turb}m\left(\frac{2n+1}{n}\frac{1}{h_f}\right)^n\left(\frac{E}{4(1-\nu^2)L_f(t)}\right)^{2n+1} \quad [A.7]$$

At the wellbore, the pressure difference in Eq. [A.7] is the largest:

$$\Delta p_{f\max} = \left(\frac{\Phi q_{inj}^n L_f}{n+1}\right)^{\frac{1}{2n+2}} \quad [A.8]$$

which is namely Eq. [5.9]. Substitution of Eq. [A.8] and Eq. [A.7] into Eq. [5.7] gives:

$$w_f(x_f) = \left[\frac{4(1-\nu^2)L_f}{E}\Delta p_{f\max}\right]\left(1-\frac{x_f}{L_f}\right)^{\frac{1}{2}} \quad [A.9]$$

Appendix B: Deficiency and Remedies to Analytical Solution of Pressure Drop Based on Power Law Model

Power law model makes reasonable predictions at intermediate shear rates, or the power law regime. However, it over predicts viscosity at very low shear rates and under predicts the viscosity at high shear rates. Ellis model is a rheological model with one additional fitting parameter:

$$\frac{1}{\mu} = \frac{1}{\mu_n}\left[1 + \left(\frac{\tau}{\tau_{\frac{1}{2}}}\right)^{\alpha-1}\right] \qquad [B.1]$$

where τ is the shear stress, and α, $\tau_{\frac{1}{2}}$, and μ_n are fitting parameters. α is equivalent to $\frac{1}{n}$ (where *n* is the power law exponent). μ_n is the viscosity at very low shear stresses. Ellis model can predict the Newtonian plateau of shear-thinning fluids at low shear stresses/rates but still underestimates the viscosity at very high shear stresses/rates. Although the Meter's equation or the Carreau model is more accurate than the Ellis model, Ellis model is chosen for this discussion because the derivations presented below require the rheological model to be based on shear stress instead of shear rate.

To calculate pressure distribution within a fracture due to non-Newtonian fluid flow, we first examine the Ellis-model-based analytical solution of flow of a shear-thinning fluid in a narrow slit given by Matsuhisa and Bird (1965):

$$q = \frac{2AB\tau_B}{3\mu_n}\left[1+\frac{3}{\alpha+2}\left(\frac{\tau_B}{\tau_{\frac{1}{2}}}\right)^{\alpha-1}\right] \qquad [B.2]$$

and

$$\tau_B = \left|\frac{\Delta p}{\Delta L}\right| B \qquad [B.3]$$

where q is the flow rate through the cross section of the slit, B the half thickness of the narrow slit, A is the area of the cross section, and $\frac{\Delta P}{\Delta L}$ is the pressure gradient along the flow direction. For flow through the fracture, q is replaced with q_f, A is replaced with $h_f w_f$, B is replaced with $w_f/2$, etc. Using similar treatments as in the Appendix A gives:

$$w_f^3\left(-\frac{dw_f}{dx_f}\right)+C_2 w_f^{\alpha+2}\left(-\frac{dw_f}{dx_f}\right)^{\alpha} = C_3 \qquad [B.4]$$

where

$$C_2 = \frac{3}{(\alpha+2)\left(2\tau_{\frac{1}{2}}C_1\right)^{\alpha-1}}, \qquad [B.5]$$

and

$$C_3 = \frac{6\mu_n C_1 q_{inj}}{h_f} \qquad [B.6]$$

and

$$C_1 = \frac{4\left(1-\nu^2\right)}{E} L_f C_{Turb} \qquad [B.7]$$

The boundary condition for Eq. [B.4] is

$$w_f\left(x_f = L_f\right) = 0 \qquad [B.8]$$

Eq. [B.4] is a Differential Algebraic Equation (DAE), which is usually solved using the Backward Euler Method (Brenan and Engquist, 1988). For our problem, application of Backward Euler Method gives:

$$f\left(w_{fN}\right) = w_{fN}^3\left(\frac{w_{fN} - w_{fN-1}}{\Delta x_f'}\right) + C_2 w_{fN}^{\alpha+2}\left(\frac{w_{fN} - w_{fN-1}}{\Delta x_f'}\right)^{\alpha} - C_3\frac{x_{fN}'}{L_f} = 0 \qquad [B.9]$$

Assuming $x_f' = L_f - x_f$. Eq. [B.9] is then solved using Newton's method:

$$w_{fN}^{l+1} = w_{fN}^{l} - \frac{f\left(w_{fN}^{l}\right)}{f'\left(w_{fN}^{l}\right)} \qquad [B.10]$$

where

$$w_{f1} = 0 \qquad [B.11]$$

Convergence for Newton's iteration is achieved by setting

$$w_{fN}^{l=1} = w_{fN-1} + \varepsilon \qquad \text{[B.12]}$$

where ε is a small positive value.

The solution to the DAE gives a more accurate solution of pressure drop along fracture compared to the analytical solution based on power law. However, it is computationally expensive to solve the DAE for every timestep. To avoid solving the DAE for calculating pressure distribution in the fracture at the cost of reasonable numerical error, a simple model is proposed as follows. The power law model is modified with the constraint below:

$$\mu = \min\left[\mu, \mu_p^0\right] \qquad \text{[B.13]}$$

and

$$\mu = \max\left[\mu, \mu_\infty\right] \qquad \text{[B.14]}$$

Thus the maximum fluid pressure drop (Eq. [5.8]) is constraint with the limits based on the analytical solutions assuming two Newtonian viscosity μ_p^0 and μ_∞:

$$\Delta p_{f\max} = \min\left[\Delta p_{f\max,} \left\{\frac{3C_{Turb}\mu_p^0}{2h_f}\left(\frac{E}{2(1-\nu^2)}\right)^3 \frac{q_{inj}}{L_f^2}\right\}^{\frac{1}{4}}\right] \qquad \text{[B.15]}$$

and

$$\Delta p_{f\max} = \max\left[\Delta p_{f\max,}\left\{\frac{3C_{Turb}\mu_{\infty}}{2h_f}\left(\frac{E}{2(1-\nu^2)}\right)^3\frac{q_{inj}}{L_f^2}\right\}^{\frac{1}{4}}\right] \quad [B.15]$$

The modified power law model for polymer viscosity in the fracture is verified by matching experimental data as shown in Fig. 5.1 and the analytical pressure drop solutions are verified against the numerical solution for the Ellis model as shown in Fig. 5.2. As shown in Fig. 5.2, for a given polymer solution (1000 ppm Flopaam 3330S), the pressure drop of the power law model matches well with the numerical solution using Ellis model after fracture half-length increases to about 10 ft. The analytical solutions based on the upper and lower Newtonian viscosity guarantee an acceptable solution of pressure drop even when fracture is less than 1 ft or greater than 1000 ft.

Appendix C: The Illinois Algorithm: An Efficient Root-Finding Method

The Illinois algorithm adopted in our solution of fracture half-length was thought to be invented at the University of Illinois in 1950's (Dowell and Jarratt, 1971). This algorithm is a modified version of the well-known false position method, or the Regula-Falsi method. The Regula-Falsi method iteratively searches for the root of an equation based on the idea of "trial and error". This method is explained below:

For the equation,

$$f(x) = 0 \qquad [C.1]$$

a root is supposed to be confined in the interval of x_{i-1} and x_i, which satisfies that

$$f(x_{i-1})\, f(x_i) < 0 \qquad [C.2]$$

We calculate a new value for next iteration:

$$x_{i+1} = \frac{x_{i-1} f(x_i) - x_i f(x_{i-1})}{f(x_i) - f(x_{i-1})} \qquad [C.3]$$

Then if

$$f(x_{i+1})\, f(x_{i-1}) < 0 \qquad [C.4]$$

The root of interest is confined in the interval of x_{i-1} and x_{i+1}. If else, the root is confined in the interval of x_i and x_{i+1}.

The iteration continues until the interval is small enough. However, when the search interval "is reached on which the function (which refers to *f(x)*) is convex or

concave", "one of the end-points of this interval is always retained, and this feature slows down the asymptotic convergence to first order" (Dowell and Jarratt, 1971). To avoid this problem and improve its computational efficiency, the Illinois algorithm was proposed: For the next iteration, if

$$f\left(x_{i+1}\right) f\left(x_i\right) < 0 \qquad \text{[C.5]}$$

in Eq. [C.3], $(x_{i-1}, f(x_{i-1}))$ is replaced with $(x_{i-1}, f(x_{i-1}))$. If

$$f\left(x_{i+1}\right) f\left(x_i\right) > 0 \qquad \text{[C.6]}$$

in Eq. [C.3], $(x_{i-1}, f(x_{i-1}))$ is replaced with $(x_{i-1}, f(x_{i-1})/2)$.

Besides, in the next iteration, $(x_i, f(x_i))$ is replaced with $(x_{i+1}, f(x_{i+1}))$.

References

Abou-Kassem, J.H. and Aziz, K., "Analytical Well Models for Reservoir Simulation", SPE 11719, *SPE Journal*, 25(4): 573-579, 1985.

Abou-Kassem, J.H. and Ertekin T., "An Efficient Algorithm for Removal of Inactive Blocks in Reservoir Simulation", JCPT-92-02-02, *Journal of Canadian Petroleum Technology*, 31(2): 25-31, 1992.

Al-Azri, N., Jamal, E., Murshidi, A., Al-Mahrouqi, A., Al-Busaidi, I., Kazzaz, A., Al-Ajmi, W., Ramalingam, S., De Kruijf, A., Al-Kharusi B. and Brooks, D., "Polymer Injection in Heavy Oil Reservoir under Strong Bottom Water Drive", SPE 129177, presented at the *SPE EOR Conference at Oil & Gas West Asia*, Muscat, Oman, 11-13 April, 2010.

Audibert, A. and Argillier, J-F., "Thermal Stability of Sulfonated Polymers", SPE 28953, presented at the *SPE International Symposium on Oilfield Chemistry*, 14-17 February, Santonio, TX, USA, 1995.

Babu, D.K. and Odeh, A.S., "Productivity of a Horizontal Well", SPE 18298, *SPE Reservoir Engineering*, 4(4): 417-421, 1989.

Bailey, J.E. and Ollis, D.F., *Biochemical Engineering Fundamentals*, 2nd Edition, McGraw Hill, New York, NY, USA, 1986.

Balhoff, M., *Modeling The Flow of Non-Newtonian Fluids in Packed Beds at the Pore Scale*, PhD Dissertation, Louisiana State University, Baton Rouge, LA, USA, 2005.

Brenan, K.E. and Engquist, B.E., "Backward Differentiation Approximations of Nonlinear Differential/Algebraic Systems", *Mathematics of Computation*, 51: 659-576, 1988.

Brennan, B., Lucas-Clements, C., Kew, S., Shumakov, Y., Camilleri, L., Akuanyionwu, O., Tunoglu, A., Hayhurst, S. and Simpson, J., "Methodologies, Solutions, and Lessons Learned from Heavy Oil Well Testing with an ESP, Offshore UK in the Bentley Field, Block 9/3b", CSUG/SPE 148833, presented at the *Canadian Unconventional Resources Conference*, Calgary, Alberta, Canada, 15-17 November, 2011.

Buell, R.S., Kazeml, H. and Poettmann, F.H., "Analyzing Injectivity of Polymer Solutions with the Hall Plot", SPE 16963, *SPE Reservoir Engineering*, 5(1): 41-46, 1990.

Bird, R.B., Stewart, W.E., and Lightfott, E.N., *Transport Phenomena*, Revised 2nd Edition, John Wiley & Sons, 2007.

Bondor, P.L., Hirasaki, G.J. and Tham, M.J., "Mathematical Simulation of Polymer Flooding in Complex Reservoirs", SPE 3524, *SPE Journal*, 12(5): 369-382, 1972.

Brooks, A.D., de Zwart, A.H., Bychkov, A., Al-Azri, N., Hern, C.Y., Al-Ajmi, W. and Mukmin, M., "Evaluation of EOR Techniques for Medium-Heavy Oil Reservoirs with a Strong Bottom Aquifer in South Oman", SPE 129149, presented at the *SPE EOR Conference at Oil & Gas West Asia*, Muscat, Oman, 11-13 April, 2010.

Cannella, W.J., Huh, C., and Seright, R.S., "Prediction of Xanthan Rheology in Porous Media", SPE 18089, presented at the *63rd Annual SPE Technical Conference and Exhibition*, Houston, TX, 2-5 October, 1988.

Cao, H., *Development of Techniques for General Purpose Simulators*, PhD Dissertation, Stanford University, Stanford, CA, USA, 2002.

Carreau, P.J., *Rheological Equations from Molecular Network Theories,* PhD Dissertation, University of Wisconsin, Maddison, WI, USA, 1968.

Carter, R.D. and Tracy, G.W., "An Improved Method for Calculating Water Influx", *Trans., AIME*, 219: 415-417, 1960.

Chang, H.L., "Polymer Flooding Technology — Yesterday, Today, and Tomorrow", SPE 7043, *Journal of Petroleum Technology*, 30 (8): 1113-1128, 1978.

Clemens T., Abdev, J., Thiele, M., "Improved Polymer-Flood Management Using Streamlines", SPE 132774, 14(2): 171-181, *SPE Reservoir Evaluation & Engineering*, 2011.

Clemens, T., Tsikouris, K., Buchgraber, M., Castanier, L., Kovscek, A., "Pore-Scale Evaluation of Polymers Displacing Viscous Oil – Computational Fluid Dynamics Simulation of Micromodel Experiments", SPE 154169, presented at the *18th SPE Improved Oil Recovery Symposium*, Tulsa, Oklahoma, 14-18 April, 2012.

Clemens, T., Deckers, M., Kornberger, M., Gumpenberger, T. and Zechner, M., "Polymer Solution Injection — Near Wellbore Dynamics and Displacement Efficiency, Pilot Test Results, Matzen Field, Austria", SPE 164904, presented at the *EAGE Annual Conference & Exhibition incorporating SPE Europec*, London, United Kingdom, 10-13 June, 2013.

Clifton, R.J., "Three-Dimensional Fracture-Propagation Models", selected topics in *Recent Advances in Hydraulic Fracturing*, SPE Monograph Series, 1989.

Computer Modeling Group Ltd, *CMG-STARS*, Calgary, Alberta, Canada, 2013.

Delamaide, E., Zaitoun, A., Renard, G. and Tabary, R., "Pelican Lake Field: First Successful Application of Polymer Flooding in a Heavy Oil Reservoir", SPE 165234, presented at the *SPE Enhanced Oil Recovery Conference*, Kuala Lumpur, Malaysia, 2-4 July, 2013.

Delshad, M., Pope, G.A. and Sepehrnoori, K., *UTCHEM Technical Documentation Version 9.0*, Center for Petroleum and Geosystems Engineering, The University of Texas at Austin, Austin, TX, July, 2000.

Delshad, M., Kim, D.H., Magbagbeola, O., Huh, C., Pope., G.A., and Tarahhom, F., "Mechanistic Interpretation and Utilization of Viscoelastic Behavior of Polymer Solutions for Improved Polymer-Flood Efficiency", SPE 113620, presented at the *16th SPE Improved Oil Recovery Symposium*, Tulsa, OK, USA, 10-12 April, 2008.

Ding, Y., "A Generalized 3D Well Model for Reservoir Simulation", SPE 30724, *SPE Journal*, 1(04): 437-450, 1996.

Dogru, A.H., "Equivalent Wellblock Radius for Partially Perforated Vertical Wells – Part I: Anisotropic Reservoirs with Uniform Grids", SPE 137051, SPE Journal, 15(04): 1028-1037, 2010.

Dogru, A.H., "Equivalent Wellblock Radius for Partially Perforated Vertical Wells – Part II: Anisotropic Reservoirs with Nonuniform Grids", SPE 137052, SPE Journal, 15(04): 1038-1046, 2010.

Doorwar, S. and Mohanty, K.K., "Viscous Fingering during Non-Thermal Heavy Oil Recovery", SPE 146841, presented at the *SPE Annual Technical Conference and Exhibition*, Denver, Colorado, 30 October – 2 November, 2011.

Doorwar, S. and Mohanty, K.K., "Viscous Fingering during Non-Thermal Heavy Oil Recovery", SPE 146841, presented at the *SPE Annual Technical Conference and Exhibition*, Denver, Colorado, 30 October – 2 November, 2011.

Dowell, M. and Jarratt, P., "A Modified Regula Falsi Method for Computing the Root of an Equation"*, BIT Numerical Mathematics*, 11(2): 168-174, 1971.

Economides, M.J. and Nolte, K.G., *Reservoir Stimulation,* 3rd Edition*,* John Wiley & Sons, June 9, 2000.

Fetkovitch, M.J., "A Simplified Approach to Water Influx Calculations – Finite Aquifer Systems", *Journal of Petroleum Technology*, 814-828, 1971.

Fabbri, C., Romero, C., Aubertin, F., Nguyen, M., Hourcq, S. and Hamon, G., "Secondary Polymer Flooding in Extra-Heavy Oil: Gaining Information on Polymer-Oil Relative Permeabilities", SPE 165237, presented at the *SPE Enhanced Oil Recovery Conference*, Kuala Lumpur, Malaysia, 2-4 July, 2013.

Flory, P.J., *Principles of Polymer Chemistry*, Ithaca, New York, Cornell University Press, 1953.

Gadde, P.B. and Sharma, M.M., "Growing injection well fractures and their impact on waterflood performance", SPE 71614, presented at the *SPE Annual Technical Conference and Exhibition*, New Orleans, LA, USA, 30 September - 3 October 2001.

Ganis, B., Liu, R., Wang, B., Wheeler, M. F. and Yotov, I., "Multiscale Modeling of Flow and Geomechanics", *Simulation of Flow in Porous Media: Applications in Energy and Environment*, 12: 165-197, 2013.

Geertsma, J. and de Klerk, F.A., "A Rapid method of predicting width and extent of hydraulically induced fractures", *Journal of Petroleum Technology*, 21(12): 1571-1581, 1969.

Gidley, J.L., Holditch, S.A., and Veatch Jr., R.W., *Recent Advances in Hydraulic Fracturing*, Richardson, TX, Society of Petroleum Engineers, 1989.

Gogarty, W.B., "Rheological Properties of Pseudoplastic Fluids in Porous Media", SPE 1566, *SPE Journal*, 7(2): 149-160, 1967.

Goudarzi, A., Delshad, M., and Sepehrnoori, K., "A Critical Assessment of Several Reservoir Simulators for Modeling Chemical Enhanced Oil Recovery Processes", SPE 163578, presented at the *SPE Reservoir Simulation Symposium*, Woodlands, TX, USA, 18-20 February, 2013.

Grabowski, J.W., Vinsome, P.K. Lin, R., Behie, G.A. and Rubin, B., "A Fully Implicit General Purpose Finite-Difference Thermal Model for In-Situ Combustion and Steam", SPE 8396, presented at the *SPE Annual Technical Conference and Exhibition*, Las Vegas, NV, USA, 23 September, 1979.

Green, D.W. and Willhite, G.P., *Enhanced Oil Recovery,* SPE Textbook Series, Volume 6, Revised Edition*,* Henry L. Doherty Memorial Fund of AIME, Society of Petroleum Engineers, Richardson, TX, USA, 1998.

Haas, R. and Durst, F., "Viscoelastic Flow of Dilute Polymer Solutions in Regularly Packed Beds", *Rheologica Acta*, 21, 566-571, 1981.

Hagoort, J., "Hydraulic Fracturing Pressures in Permeable Subsurface Layers", SPE 7110, *SPE General*, 1978.

Han, X.-Q., Wang, W.-Y. and Xu, Y., "The Viscoelastic Behavior of HPAM Solutions in Porous Media and Its Effects on Displacement Efficiency", SPE 30013, presented at the *Internal Meeting on Petroleum Engineering*, Beijing, China, 14-17 November, 1995.

Heemskerk, J., Janssen-van Rosmalen, R., Holtslag, R.J. and Teeuw, D., "Quantification of Viscoelastic Effects of Polyacrylamide Solutions", SPE/DOE 12652, presented at the *SPE/DOE 4th Enhanced Oil Recovery Symposium*, Tulsa, OK, 15-18 April, 1984.

Hejri, S., Willhite, G.P., and Green, D.W., "Development of Correlations to Predict Biopolymer Mobility in Porous Media", SPE 17396, *SPE Reservoir Engineering*, 6(01): 91-98, 1991.

Hirasaki, G.J., and Pope, G.A., "Analysis of Factors Influencing Mobility and Adsorption in the Flow of Polymer Solution through Porous Media", SPE 4026, *SPE Journal*, 337-346, 1974.

Ji, L., Settari, A., Orr, D. and Sulllian, R.B., "Methods for Modeling Static Fractures in Reservoir Simulation", presented at the *Petroleum Society's 5th Canadian International Petroleum Conference*, Calgary, Alberta, Canada, 8-10 June, 2004a.

Ji, L., Settari, A., Sulllian, R.B. and Orr, D., "Methods for Modeling Dynamic Fractures in Coupled Reservoir and Geomechanics Simulation", SPE 90874, presented at the *SPE Annual Technical Conference and Exhibition*, Houston, TX, U.S.A, 26-29 September, 2004b.

Ji, L., Settari, A. and Sullivan, R.B., "A Novel Hydraulic Fracturing Model Fully Coupled with Geomechanics and Reservoir Simulation", SPE 110845, *SPE Journal*, 14(3): 423-430, 2009.

Ju, L. and Burkardt, J., "MGMRES: Restarted GMRES Solver for Sparse Linear Systems", from http://people.sc.fsu.edu/~jburkardt/f_src/mgmres/mgmres.html, 2012.

Kamaraj, K., Zhang, G., Liu, Y. and Seright, R.S., "Effect of Residual Oil Saturation on Recovery Efficiency during Polymer Flooding of Viscous Oils", OTC 22040, presented at the *Artic Technology Conference*, Houston, TX, USA, 7-9 February, 2011.

Karpinski, L., Maliska, C.R., Marcondes, F., Delshad, M. and Sepehrnoori, K., "An Element Based Conservative Approach Using Unstructured Grids in Conjunction with a Chemical Flooding Compositional Reservoir Simulator", *Proceedings of COBEM*, 2009.

Khodaverdian M., Sorop, T., Postif, S. and Van den Hoek, P., "Polymer Flooding in Unconsolidated-Sand Formations: Fracturing and Geomechanical Considerations", SPE 121840, *SPE Production & Operations*, 25(02): 211-222, May, 2010.

Khristianovich, S.A. and Zheltov, Y.P., "Formation of Vertical Fractures by Means of Highly Viscous Fluids", *Proc., Fourth World Pet. Gong.*, II 579, Rome, 1955.

Koh, H., *Experimental Investigation of the Effect of Polymers on Residual Oil Saturation*, PhD Dissertation, The University of Texas at Austin, Austin, TX, USA, 2015.

Kong, X., Delshad, M., and Wheeler, M.F., "A Numerical Study of Benefits of Adding Polymer to WAG Processes for a Pilot Case", SPE 173230, presented at the *SPE Reservoir Simulation Symposium*, Houston, TX, USA, 23-25 February, 2014.

Kulawardana, E.U., Koh, H., Kim, D.H., Liyanage, P.J., Upamali, K., Huh, C., Weerasooriya, U., and Pope, G.A., "Rheology and Transport of Improved EOR

Polymers under Harsh Reservoir Conditions", SPE 154294, presented at the *SPE Improved Oil Recovery Symposium*, Tulsa, OK, USA, 14-18 April, 2012.

Lake, L.W., *Enhanced Oil Recovery*, Prentice Hall Inc., NJ, USA, 1989.

Lashgari, H.R., Lotfollahi, M., Delshad, M., Sepehrnoori, K., and de Rouffignac, "Steam-Surfactant-Foam Modeling in Heavy Oil Reservoirs", SPE 170178, presented at the *SPE Heavy Oil Conference-Canada*, Alberta, Canada, 10-12 June, 2014.

Lee, K., Huh, C., and Sharma, M.M., "Impact of Fracture Growth on Well Injectivity and Reservoir Sweep during Waterflood and Chemical EOR Processes", SPE 146778, presented at the *SPE Annual Technical Conference and Exhibition*, Denver, Colorado, USA, 30 October – 2 November, 2011.

Lee, K., *Impact of Fracture Creation and Growth on Well Injectivity and Reservoir Sweep during Waterflood and Chemical EOR Processes*, PhD Dissertation, The University of Texas at Austin, Austin, TX, USA, 2012.

Lee, V.B., *The Development and Evaluation of Polymers for Enhanced Oil Recovery*, Master's Thesis, The University of Texas at Austin, Austin, TX, USA, 2015.

Levitt, D., Jouenne, S., Bondino, I., Gingras. J.P. and Bourrel, M., "The Interpretation of Polymer Coreflood Results for Heavy Oil", SPE 150566, presented at the *SPE Heavy Oil Conference and Exhibition*, Kuwait City, Kuwait, 12-14 December, 2011.

Li, Z., Delshad, M., Lotfollahi, M., Koh, H., Luo, H., Chang, H., Zhang, J., Dempsey, P., Lucas-Clements, C., and Brennan, B., "Polymer Flooding of a Heavy Oil Reservoir with an Active Aquifer", SPE 169149, presented at the *SPE Improved Oil Recovery Symposium*, Tulsa, Oklahoma, USA, 12-16 April, 2014.

Li, Z., and Delshad, M., "Development of an Analytical Injectivity Model for Non-Newtonian Polymer Solutions", SPE 163672, *SPE Journal*, 19(03): 24-585, 2014.

Liu, J., Delshad, M., Pope, G.A., and Sepehrnoori, K., "Application of Higher-Order Flux-Limited Methods in Compositional Simulation", *Transport in Porous Media*, 16(1): 1-30, 1994.

Luo, H., Al-Shalabi, E.W., Delshad, M., Panthi, K., and Sepehrnoori, K., "A Robust Geochemical Simulator to Model Improved Oil Recovery Methods", SPE 173211, presented at the *SPE Reservoir Simulation Symposium*, Houston, TX, USA, 23-25 February, 2015.

Ma, Y., *Diagnosis of Induced Hydraulic Fractures during Polymer Injection*, Master's Thesis, The University of Texas at Austin, Austin, TX, USA, 2015.

Manichand, R.N., Moe Soe Let, K.P., and Suriname, S., Gil, L., Quillien, B., and Seright, R.S., "Effective Propagation of HPAM Solutions through the Tambaredjo Reservoir during a Polymer Flood", SPE 164121, presented at the *SPE*

International Symposium on Oilfield Chemistry, The Woodlands, TX, USA, 8-10 April, 2013.

Masuda, Y., Tang, K., Miyazawa, M., and Tanaka, S., "1D Simulation of Polymer Flooding Including the Viscoelastic Effect of Polymer Solution", SPE 19499, *SPE Reservoir Engineering*, 247-252, 1992.

Matsuhisa, S. and Bird, R.B., "Analytical and Numerical Solutions for Laminar Flow of the Non-Newtonian Ellis Fluid", *AIChE Journal*, 11(4): 588-595, July 1965.

Mehra, R., Hadjitofi, M. and Donnelly, J.K., "An Automatic Time-Step Selector for Reservoir Models", SPE 10496, *SPE Reservoir Simulation Symposium*, New Orleans, LA, 31 January – 3 February, 1982.

Meter, D.M. and Bird, R.B., "Tube Flow of Non-Newtonian Polymer Solutions: Part I – Laminar Flow and Rheological Models", *AIChE Journal*, 10(6): 878-881, 1964.

Mollaei, A., Delshad, M., and Li, Z., "A Novel Forecasting Model for Chemical Flooding Enhanced Oil Recovery", SPE 166157, presented at the *SPE Annual Technical Conference and Exhibition*, New Orleans, LA, USA, 30 September – 2 October, 2013.

Nghiem, L.X., Forsyth Jr., P.A., and Behie, A., "A Fully Implicit Hydraulic Fracture Model", SPE 10506, *Journal of Petroleum Technology*, 36(07): 1191-1198, 1984.

Nolen, J.S., and Berry, D.W., "Tests of the Stability and Time-Step Sensitivity of Semi-Implicit Reservoir Simulation Techniques", SPE 2981, *SPE Journal*, 12(3): 253-266, 1972.

Nordgren, R.P., "Propagation of a vertical hydraulic fracture", SPE 3009, *SPE Journal*, 12(4): 306-314, 1972.

Peaceman, D.W., "Interpretation of Well-block Pressures in Numerical Reservoir Simulation", SPE 6893, *SPE Journal*, 18(3): 183-194, 1978.

Peaceman, D.W., "Interpretation of Well-block Pressures in Numerical Reservoir Simulation with Nonsquare Grid Blocks and Anisotropic Permeabilities", SPE 10528, *SPE Journal*, 23(3): 531-543, 1983.

Peaceman, D.W., "Representation of a Horizontal Well in Numerical Reservoir Simulation", SPE 21217, *SPE Advanced Technology Series*, 1(1): 7-16, 1993.

Perkins, T.K., and Kern, L.R., "Widths of Hydraulic Fractures", *Journal of Petroleum Technology*, 13(09): 937-949, September 1961.

Perkins, T.K., and Gonzalez, J.A., "The Effect of Thermoelastic Stresses on Injection Well Fracturing", SPE 11332, *SPE Journal*, 25(1): 78-88, 1985.

Pope, G.A., "The Application of Fractional Flow Theory to Enhanced Oil Recovery", SPE 7660, *SPE Journal*, 20(3): 191-205, 1980.

Qi, P., Ehrenfried, D.H., and Balhoff, M.T., "Reduction of Residual Oil Saturation in Sandstone Cores using Viscoelastic Polymers", to be presented at *20th SPE Improved Oil Recovery Conference*, April 9-13, 2016.

Ranjbar, M., Rupp, J., Pusch, G. and Meyn, R., "Quantification and Optimization of Viscoelastic Effects of Polymer Solutions for Enhanced Oil Recovery", SPE/DOE 25154, presented at *SPE/DOE 8th Enhanced Oil Recovery Symposium*, Tulsa, OK, 22-24 April, 1992.

Saad, N., *Field Scale Simulation of Chemical Flooding*, PhD Thesis, The University of Texas at Austin, TX, USA, 1989.

Saad, Y., *Iterative Methods for Sparse Linear Systems*, 2nd Edition, SIAM, 2003.

Schlumberger, *ECLIPSE® Reservoir Simulation Software Version 2010.2 Technical Description*, Schlumberger Limited, 785-787, 2010.

Seright, R.S., Seheult, M., and Talashek, T., "Injectivity Characteristics of EOR Polymers", SPE 115142, *SPE Journal*, 12(5): 783-792, 2009.

Settari, A., "Simulation of Hydraulic Fracturing Processes", SPE 7693, *SPE Journal*, 20(06): 487-500, 1980.

Sharma, A., *Assessment of Polymer Injectivity during Chemical Enhanced Oil Recovery Processes*, Master's Thesis, The University of Texas at Austin, Austin, TX, 2010.

Sharma, A., Delshad, M., Huh, C. and Pope, G.A., "A Practical Method to Calculate Polymer Viscosity Accurately in Numerical Reservoir Simulators", SPE 147239, presented at the *SPE Annual Technical Conference and Exhibition*, Denver, CO, 31 October – 2 Nov, 2011.

Sharma, M., Suri, A. and Gadde, P., *University of Texas Well Injectivity Decline Simulator (UTWID) 7.0: A Simulator for Injection Well Design and Management, Version 2009 User Guide*, Austin, TX, USA, 2009.

Singh, G., *Coupled Flow and Geomechanics Modeling for Fractured Poroelastic Reservoirs*, PhD Dissertation, The University of Texas at Austin, TX, USA, 2014.

Sheng, J., *Modern Chemical Enhanced Oil Recovery: Theory and Practice*, Gulf Professional Publishing, 2010.

Schenk, O., Gärtner, K., Fichtner, W., & Stricker, A., *PARDISO: A High-Performance Serial and Parallel Sparse Linear Solver in Semiconductor Device Simulation*, Future Generation Computer Systems, 18(1): 69-78, 2001.

Schenk, O., Gärtner, K., Karypis, G., Luce, R., and Carbonetto, P., "PARDISO 5.0.0 Solver Project", from http://www.pardiso-project.org/, 2014.

Skauge, A., Ormehaug, P.A., Gurholt, T., Vik, B., Bondino, I. and Hamon, G., "2-D Visualization of Unstable Waterflood and Polymer Flood for Displacement of

Heavy Oil", SPE-154292-MS, presented at the *18th SPE Improved Oil Recovery Symposium*, Tulsa, OK, USA, 14-18 April, 2012.

Intel™, *Intel Math Kernel Library Reference Manual*, 2014.

Skauge, A., and Shiran, B.S., "Low Salinity Polymer Flooding", presented at the *IOR 2013 – 17th European Symposium on Improved Oil Recovery*, 16 April, 2013.

Slater, G.E. and Farouq-Ali, S.M., "Simulation of Oil Recovery by Polymer Flooding", PETSOC-70-04-05, *Journal of Canadian Petroleum Technology*, 9(04); 251-260, 1970.

Sorbie, K.S., Roberts, L.J. and Foulser, R.W.S., "Polymer Flooding for Highly Stratified Brent Sands in the North Sea", *Proc. 2nd Eur. Symp. on EOR*, Paris, France, 8-10 November, 1982.

Sorbie, K.S., *Polymer-Improved Oil Recovery*, Blackie and Son Ltd, Glasgow, 1991.

Stahl, G. A. and Schulz, D. N. (Eds), *Water-Soluble Polymers for Petroleum Recovery*, Springer, 1988.

Stavland, A., Jonsbraten, H.C., Lohne, A., Moen, A. and Giske, N.H., "Polymer Flooding – Flow Properties in Porous Media versus Rheological Parameters", SPE 131103, presented at the *SPE EUROPEC/EAGE Annual Conference and Exhibition*, Barcelona, Spain, 14-17 June, 2010.

Suri, A., and Sharma, M.M., "Fracture Growth in Horizontal Injectors", SPE 119379, presented at the *2009 SPE Hydraulic Fracturing Technology Conference*, The Woodlands, TX, USA, 19-21 January, 2009.

Suri, A., Sharma, M.M., and Peters, E.J., "Estimates of Fracture Lengths in an Injection Well by History Matching Bottomhole Pressures and Injection Profile", SPE 132524, *SPE Reservoir Evaluation & Engineering*, August, 2011.

Taber, J.J., Martin, F.D. and Seright, R.S., "EOR Screening Criteria Revisited — Part 1: Introduction to Screening Criteria and Enhanced Recovery Field Projects", SPE 35385, *SPE Reservoir Engineering*, 12(3): 189-198, 1997.

Teeuw, D. and Hesselink, F.T., "Power-Law Flow and Hydrodynamic Behavior of Biopolymer Solutions in Porous Media", SPE 8982, presented at the *SPE Oilfield and Geothermal Chemistry Symposium*, Stanford, CA, USA, 28-30 May, 1980.

Teklu, T.W., Alameri, W., Graves, R.M., Tutuncu, A.N., Kazemi, H. and AlSumaiti, A.M., "Geomechanics Considerations in Enhanced Oil Recovery", SPE 162701, presented at the *SPE Canadian Unconventional Resources*, Calgary, Alberta, Canada, 30 October – 1 November, 2012.

Todd, M.R., and Longstaff, W.J., "The Development, Testing and Application of a Numerical Simulator for Predicting Miscible Flood Performance", SPE 3484, *Journal of Petroleum Technology*, 24(07): 874-882, 1972.

van den Hoek, P.J., Mahani, H., Sorop, T.G., Brooks, A.D., Zwaan, M., Sen S., Shuaili K. and Saadi, F., "Application of Injection Fall-Off Analysis in Polymer Flooding", SPE 154376, presented at the *74th EAGE Conference & Exhibition incorporating SPE EUROPEC 2012*, Copenhagen, Denmark, June 4-7, 2012.

Van Poollen, H.K., Breitenbach, E.A. and Thurnau, D.H., "Treatment of Individual Wells and Grids in Reservoir Modeling", SPE 2022, *SPE Journal*, 8(04): 341-346, 2007.

Verma, S., Adibhatla, B., Kaminsky, R., Wattenbarger, C. and Davidson, J., "Modeling Polymer Flood in an Unstructured Grid Simulator", SPE 118985, presented at the *SPE Reservoir Simulation Symposium*, The Woodlands, TX, USA, 2-4 February, 2009.

Vinsome, P. and Westerveld, J., "A Simple Method for Predicting Cap and Base Rock Heat Losses in Thermal Reservoir Simulators", *Journal Canadian Petroleum Technology*, 19(3): 87-90, 1980.

Wang, D., Cheng, J., Yang, Q., Gong, W., Li, Q., and Chen, F., "Viscous-Elastic Polymer Can Increase Microscale Displacement Efficiency in Cores", SPE 63227, presented at the *SPE Annual Technical Conference and Exhibition*, Dallas, TX, USA, 1-4 October, 2000.

Wassmuth, F.R., Green, K. and Hodgins, L., "Polymer Flood Technology for Heavy Oil Recovery", Paper 2007-182, presented at the *Canadian International Petroleum Conference*, Calgary, Alberta, 12-14 June, 2007.

Wassmuth, F.R., Arnold, W., Green, K. and Cameron, N., "Polymer Flood Application to Improve Heavy Oil Recovery at East Bodo", PETSOC-09-02-55, *Journal of Canadian Petroleum Technology*, 48(02): 55-61, 2009.

Wheeler, M.F., *Advanced Techniques and Algorithms for Reservoir Simulation, II: The Multiblock Approach in the Integrated Parallel Accurate Reservoir Simulator (IPARS)*, Resource Recovery, Confinement, and Remediation of Environmental Hazards, 131: 9-19, 2002.

Wick, T., Singh, G., and Wheeler, M.F., "Fluid-Filled Fracture Propagation with a Phase-Field Approach and Coupling to a Reservoir Simulator", SPE 168597, SPE Journal, Preprint, October, 2015.

Wreath, D., Pope, G.A. and Sepehrnoori, K., "Dependence of Polymer Apparent Viscosity on the Permeable Media and Flow Conditions", *In Situ*, 14(3), 263-284, 1990.

Yerramilli, S.S., Zitha, P.L.J. and Yerramilli, R.C., "Novel Insight into Polymer Injectivity for Polymer Flooding", SPE 165195, presented at the *SPE European Formation Damage Conference and Exhibition*, Noordwijk, The Netherlands, 5-7 June, 2013.

Yuan, C., Delshad, M. and Wheeler, M.F., "Parallel Simulations of Commercial-Scale Polymer Floods", SPE 132441, presented at the *SPE Western Regional Meeting, Anaheim*, CA, USA, 27-29 May, 2010.

Yuan, C., *Commercial Scale Simulations of Surfactant/Polymer Flooding*, PhD Dissertation, The University of Texas at Austin, Austin, TX, USA, 2012.

Zechner, M., Buchgraber, M., Clemens, M., Gumpenberger, T., Castanier, L.M., and Kovscek, A.R., "Flow of Polyacrylamide Polymers in the Near-Wellbore-Region, Rheological Behavior within Induced Fractures and Near-Wellbore Area", SPE 166085, presented at the *SPE Annual Technical Conference and Exhibition*, New Orleans, LA, USA, 30 September - 2 October, 2013.

Zechner, M., Clemens, T., Suri, A., and Sharma, M.M., "Simulation of Polymer Injection under Fracturing Conditions – A Field Pilot in the Matzen Field, Austria", SPE 169043, presented at the *SPE Improved Oil Recovery Symposium*, Tulsa, OK, USA, 12-16 April, 2014.

Zeito, G.A., "Three Dimensional Numerical Simulation of Polymer Flooding in Homogeneous and Heterogeneous Systems", SPE 2186, *Fall Meeting of the Society of Petroleum Engineers of AIME, 29*, Houston, TX, September 29 – October 2, 1968.

Vita

Zhitao Li graduated from The First High School of Changsha, Hunan, in 2005. In 2009 he received the Bachelor of Science degree in Mechanical Engineering from the University of Science and Technology of China. He entered the graduate school of Johns Hopkins University in Sept. 2009. In Jun. 2010, he transferred to the Department of Petroleum and Geosystems Engineering at The University of Texas at Austin to pursue a Ph.D. degree in Petroleum Engineering.

Permanent email: zli@utexas.edu

This dissertation was typed by the author.